Finite temperature dynamics of a degenerate Fermi gas with unitarity limited interactions

dissertation

by

Edmundo Ricardo Sánchez Guajardo

submitted to the Faculty of Mathematics, Computer Science and Physics of the University of Innsbruck

in partial fulfillment of the requirements for the degree of doctor of science

advisor:
Univ.Prof. Dr. Rudolf Grimm,
Institute of Experimental Physics, University of Innsbruck,
Institute for Quantum Optics and Quantum Information
of the Austrian Academy of Sciences

Innsbruck, October 2011

a Inés Helena

Summary

In this thesis we present our experimental study of the dynamics of an ultracold Fermi gas at finite temperature in the presence of unitarity limited interactions. We trap fermionic ^{6}Li in a single focused laser beam and tune the interactions using a Feshbach resonance. At finite temperature the cloud is made up of a superfluid component coexisting with a noncondensed part. In the presence of unitarity limited interactions both obey the Euler equations describing hydrodynamic behavior. However, whereas the superfluid is hydrodynamic due to its long range order, the noncondensed state is hydrodynamic due to the very short collision times in comparison to the trap frequency. Thus, the former is quantum hydrodynamic and the latter collisional hydrodynamic. Moreover, on resonance the crossover from collisional hydrodynamic to near-collisionless is at a temperature much higher than the condensation critical temperature. Distinguishing experimentally between the two regimes is difficult. It is the purpose of this thesis to study the finite temperature dynamics of the cloud and the effect of the coexisting hydrodynamic fluids primarily in the unitarity limit.

In a first set of experiments we used collective modes to study the finite temperature dynamics of the cloud. Using the scissors mode excitation we are able to map the temperature versus interaction strength phase diagram and identify the crossover from hydrodynamic to near-collisionless dynamics. We find a large temperature region above the critical temperature where the noncondensed state shows collisional hydrodynamic behavior. To further study the temperature dependence of the collisional hydrodynamic state above the critical temperature on resonance we compare different collective modes. The experimental data showing the transition from hydrodynamic to near-collisionless behavior as a function of temperature is compared to a theoretical model that can include both pairing correlations and Pauli blocking. We find that both elements are necessary to properly describe the observed change of dynamics.

In subsequent experiments we study rotational properties of the cloud. By means of a rotating ellipse we introduce angular momentum into the noncondensed component. The measurement of the precession angle of the quadrupole mode excitation allows us to determine the precession frequency of the cloud, which relates to its angular momentum. The dissipation of the angular momentum can be fitted to a model, which gives the collision time that one uses to quantify how hydrodynamic the cloud is. We find that on resonance the noncondensed state is most hydrodynamic and shows very long lifetimes of the angular momentum. Next we measure the total angular momentum of the cloud to obtain the moment of inertia (MOI). The presence of the superfluid quenches the MOI of the noncondensed component. Hence, by measuring the temperature dependence of the MOI on resonance we are able to estimate a critical temperature

In the context of interference experiments of two molecular BECs also the deep hydrodynamic state of the cloud is observed. In these set of experiments we observe that close to the unitarity limit the two colliding clouds do not penetrate each other, but rather collide hydrodynamically.

As a first step to study the effect of the two hydrodynamic fluids in the context of second sound, we develop the experimental and analytical tools to excite and analyze adiabatic higher order collective modes. It has been theoretically suggested that they may offer a route to measuring entropy waves, that is to say, second sound. Introducing a repulsive laser beam perpendicular to the axial direction of the cigar shape cloud and a camera to image the axial density profile, we observe collective modes up to third order in the zero temperature limit. We recover the wave form and oscillation frequency of each mode.

Thanks!

First of all I would like to thank my advisor Rudi Grimm for giving me the opportunity of joining the group and working in the experiment. I would like to thank him for very valuable suggestions and advice. I also want to thank Florian Schreck and Johannes Hecker Denschlag for their suggestions.

I had the opportunity to work with two different postdocs, from whom I learned quite a bit. When I first joined the lab in January of 2007 Matthew Wright was postodc. During those first months of my PhD he advised me on my first projects and introduced me to the most basic concepts of strongly interacting Fermi gases. Even though we overlapped in the lab for only half a year, it was for me very fruitful. In addition to Matt, I would also like to thank Meng Khoon Tey, who joined the lab in summer of 2010. It was nice working with him in the lab and I learned quite a few technical things from him. We also shared seeing the higher order collective modes for the first time.

I would also like to thank the PhD students with whom I worked at some point: Alexander Altmeyer, Stefan Riedl, Christoph Kohstall, and Leonid Sidorenkov. In particular, Stefan was always available for discussions and taught me the basic things around the lab. I had a very good time working with him. Leonid gave me a hand building electronic devices - not to mention dealing with the water leaks!

I also have to thank PhD students that were not in the lab but with whom I worked. In particular I want to thank Andreas Trenkwalder: I had some very useful physics discussions with him and he gave me valuable comments on the thesis. He was also always ready to discuss some technical problem. I also want to mention Manfred Mark for developing so many electronic devices for the group - eventually finding them in the electronics workshop was great help in implementing large changes.

Not directly in the lab but also very important for its success are the staff in the mechanical workshop, electronics workshop, and the secretaries. I would like to thank the guys in the mechanical workshop for being always so forthcoming in building things for us. In the electronics workshop I want to thank Arthur Wander for discussing the circuit diagrams with me and introducing me to some electronic components. Gerhard Hendl always had time to discuss electronics specific to our lab and was always available to help us check something in more detail. The secretaries Christine Götsch-Obmascher, Nicole Jorda, Karin Köhle and Sabine Hofer Brigo, always try to help and minimize the administrative work one has to do.

I want to end thanking my family. Orlaith and Inés Helena shared my time in Innsbruck and often supported me or inspired me when I most needed it. My parents and sisters have always given me their unconditional support, and backed me in (most of) my endeavors - thanks.

Contents

1. Introduction

1.1. Overview

In this thesis we report on experimental research done with a degenerate cloud of fermionic ^{6}Li in the presence of a Feshbach resonance. The experimental studies address questions regarding the dynamic properties of the gas. Hence, we first give an overview of the field of ultracold Fermi gases. This includes a brief historical review, the basic ideas behind strongly interacting ultracold atom clouds and tunable interactions, and finally a review of the current status of the field. Then the dynamic properties of the gas are considered. In addition to reviewing experimental work on the topic, we give a concise framework of collective modes before introducing the content of this thesis.

1.1.1. History

The field of atomic physics underwent a revolution when in 1995 a gas of bosonic particles was condensed into a Bose-Einstein condensate (BEC) [And95, Dav95]. As the temperature of a gas is lowered the interparticle spacing decreases up to the point where it is comparable to the thermal de Broglie wavelength, $\lambda_{\mathrm{dB}} = \sqrt{2\pi\hbar/mk_BT}$, where m is the mass of the particle and T the temperature of the gas. At this temperature ($T = T_{BEC}$) the particles become indistinguishable and, in the case of bosons, a phase transition takes place to the state where all the atoms are in the ground state. This is the BEC.

The BEC is a quantum fluid. Below the aforementioned degeneracy temperature the statistics do not correspond anymore to a Maxwell-Boltzmann distribution of a normal thermal gas, but are governed by the Bose distribution function

$$f_{\mathrm{Bose}}(\epsilon) = \frac{1}{\exp\left(\frac{\epsilon-\mu}{k_BT}\right) - 1}, \tag{1.1}$$

where ϵ is the energy per particle and μ is the chemical potential. In the presence of weak repulsive interactions a superfluid is formed. The superfluid state has zero entropy and zero viscosity. It is conveniently described in the framework of a mean-field approximation by the Gross-Pitaevskii equation,

$$i\hbar\partial_t\psi(\mathbf{x},t) = \left(-\frac{\hbar^2}{2m}\nabla^2 + U(\mathbf{x}) + g|\psi(\mathbf{x},t)|^2\right)\psi(\mathbf{x},t), \tag{1.2}$$

where U is the external trapping potential, g is the coupling constant and the nonlinear term describes the contact interactions. The single macroscopic wave function, $\psi(\mathbf{x},t)$, describes the macroscopic quantum state. Because the condensate velocity field is proportional to the gradient of the phase of this wave function, $v_c(\mathbf{r},t) \propto \nabla\theta(\mathbf{r},t)$, the superfluid flow is irrotational, $\nabla \times v_c = 0$ [Gri09]. Angular momentum can only be introduced in the form of quantized vortices.

Unlike the bosonic particles identical fermions cannot occupy the same quantum state as the temperature is lowered into quantum degeneracy. For temperatures below the Fermi temperature,

$T_F = E_F/k_B$, fermions follow Fermi-Dirac statistics,

$$f_{\mathrm{FD}}(\epsilon) = \frac{1}{\exp\left(\frac{\epsilon-\mu}{k_B T}\right)+1}. \tag{1.3}$$

In this case one fills the energy levels up to the Fermi surface forming a Fermi sea. Hence, identical fermions cannot form a BEC.

However, excitations at the surface of a filled Fermi sea may lead to pairing of atoms. This pairing mechanism was first described by L. Cooper [Coo56]. In his seminal work he realized that fermions lying on the Fermi surface and with opposite momentum could be excited to form a pair in the presence of weakly attractive interactions. In real space the size of the paired atoms, known as Cooper pair, is much larger than the interparticle spacing. Thus, Cooper pairs overlap in space resulting in a many-body state. Later Bardeen, Cooper, and Schrieffer (BCS) developed a theory with the Cooper pair as a stable ground state [Bar57]. Their theory properly describes the superconductor in which the Cooper pairs are in a superfluid state.

The BCS superfluid state is connected to the BEC of tightly bound pairs. In other words, the many-body Cooper pair can evolve into a pair with size smaller than the interparticle spacing that follows Bose statistics [Eag69]. It was then shown that the tightly bound molecules and Cooper pairs connect smoothly through a crossover [Leg80]. Finally, Nozières and Schmitt-Rink found that also the critical temperature can be joined smoothly[Noz85].

Fermions were first cooled down to a degenerate state in [DeM99b] using two spin states of ^{40}K in a magnetic trap and cooled evaporatively. It was followed by other groups also using magnetic traps [Tru01, Sch01, Had02, Roa02] but with a Bose-Fermi mixture to sympathetically cool the Fermi component to degeneracy. All-optical production schemes were later used [Gra02, Joc03a] to cool the gas using forced evaporative cooling, *ie*, without the need of a boson to do sympathetic cooling.

1.1.2. Feshbach resonances

The Feshbach (FB) resonance allows the tuning of the interaction strength with an external magnetic field [Fes58, Fan61, Fes62, Chi10]. Effectively what happens is that the energy difference between two molecular potentials is being changed. One potential is called the entrance channel (or open channel): it holds two free atoms at large interatomic distance and a scattering state when the atomic separation is small. The second potential is referred to as the closed channel since it is normally energetically inaccessible to the atoms in the entrance channel. However, it can support a bound state if its energy is near the threshold of the entrance channel. Hence, by means of an external magnetic field the energy difference can be adjusted such that two scattering atoms in the entrance channel couple to the bound state in the closed channel. In [Moe95] a function was introduced to describe the change of the scattering length with the magnetic field, namely,

$$a(B) = a_{bg}\left(1 - \frac{\Delta B}{B - B_0}\right), \tag{1.4}$$

where a_{bg} is the background scattering length, B_0 is the center of the resonance, and ΔB the width of the resonance (for ^{6}Li in the lowest two hyperfine states $a_{bg} = -1405a_0$, $B_0 = 834.15$ G, and $\Delta B = 300$ G). Near B_0 we find the *universal regime* in which the binding energy of the pairs is

given by $E_b = \hbar^2/2\mu a^2$, where μ is the reduced mass, and the molecular state is a halo dimer, that is to say, its size is in the order of a.

In the universal regime the energy scale of the system is set by the Fermi energy of the trapped noninteracting gas, $E_{\mathrm{F}} = \hbar\bar{\omega}(3N)^{1/3}$, where $\bar{\omega} = (\omega_x\omega_y\omega_z)^{1/3}$ is the geometric mean trap frequency, and N is the total number of atoms in both spin states. The relevant length scale is defined by the Fermi wave number, k_{F}, and relates to the Fermi energy as $\hbar k_{\mathrm{F}} = \sqrt{2mE_{\mathrm{F}}}$. Also the temperature scale is given by the Fermi temperature, $T_{\mathrm{F}} = E_{\mathrm{F}}/k_B$, below which the gas is degenerate.

Within the universal regime the experimental interest is primarily to sit on resonance, where the interactions are the strongest. On resonance the scattering cross section has its largest allowed value by quantum mechanics. This is known as the *unitarity limit*. It offers a laboratory to study effects beyond mean-field in a strongly correlated many-body system. In this limit one can use a universal parameter, β, to write the mean-field potential as $U_{\mathrm{MF}} = \beta E_{\mathrm{F}}$ [Ho04].

In the case of fermions, the tunability of the scattering length allows the experimental realization of the crossover from the BEC to the BCS. This is characterized by the dimensionless parameter $1/k_{\mathrm{F}}a$. As a function of this parameter the BEC limit corresponds to those values $1/k_{\mathrm{F}}a \gg 1$, and the BCS limit to $1/k_{\mathrm{F}}a \ll -1$.

In the case of a Bose gas the first studies on FB resonances were done in [Ino98, Cou98]. For fermions it followed the experimental realization of the degenerate Fermi gas. The first observation of hydrodynamic expansion, namely, the effect of strong interactions, was reported in [O'H02a] for an unpaired ultracold cloud. The initial studies reported in [Die02, Joc02, OH02b, O'H02a] for ^{6}Li and for ^{40}K focused on characterizing the tunability of the scattering length and characterization of the resonant region. However, whereas some studies focused on the atom loss associated to inelastic decay [Die02], others studied the atom decay in relation to the elastic scattering associated to the resonance [Joc02]. Unexpectedly, for fermions, as opposed to bosons, losses are heavily suppressed. This was later understood to be the result of Pauli blocking. Other experiments mapped the elastic cross section for ^{40}K [DeM99a, Lof02] by extracting the thermalization constant of the gas from the time evolution of the aspect ratio of the widths. Finally, the measurement of the interaction energy in the crossover region was reported in [Bou03].

The Feshbach resonance was used to form diatomic molecules, both in a Bose gas [Her03, Xu03, Dür04] as in a Fermi gas [Reg03, Cub03, Str03, Joc03b, Reg04a]. The first realization of diatomic molecules in Fermi gases was in [Reg03], where the ^{40}K$_2$ molecules were detected using radio-frequency spectroscopy at different magnetic field values. The long-lifetime of the molecules gave rise to expectation that cooling towards a BEC could be possible. Experiments with ^{6}Li focused on the atom-dimer collisional properties and its prospects for evaporative cooling [Joc03b].

The Feshbach molecules were Bose condensed (mBEC) [Joc03a, Gre03, Zwi03]. The experiments in [Joc03a, Gre03] relied on forced evaporative cooling of two spin states to reach the necessary low temperature. In the former case, a mBEC of ^{6}Li$_2$ was directly produced during the evaporation. It was then indirectly observed through two measurements: firstly, the large number of atoms in the trap for the low trap frequency in which no unpaired atoms could exist. The temperature of this very shallow trap was well below the critical temperature for condensation. Secondly, by exciting the axial quadrupole mode they were able to confirm that the oscillation frequency corresponds to that of a mBEC. In the latter case, the mBEC was created after cooling below degeneracy by adiabatically sweeping the magnetic field across the FB resonance from attractive to repulsive interactions. The bimodal distribution of a mBEC of ^{40}K$_2$ was directly observed using state selective high field absorption imaging after dissociating the dimers with an RF pulse. In the experiment of

[Zwi03] the ^{6}Li was in the stretched low-field seeking state and was sympathetically cooled using Na to a temperature just above the critical temperature. The ^{6}Li atoms were then transferred to the lowest spin state. After setting the desired magnetic field in the vicinity of the FB resonance a RF pulse was applied to get the desired two spin states mixture. Finally the atoms were further cooled down with forced evaporative cooling. The onset of the BEC was further studied by the observation of the bimodal distribution for different laser power. What is fascinating is that the almost simultaneous publications successfully produced the mBEC in rather different ways, maybe heralding the rich and vast experiments that were to come.

1.1.3. Exploring the BEC-BCS crossover

Next the BEC-BCS crossover was explored with a broad range of experiments. It was showed that one could adiabatically change the interaction strength across the FB resonance [Bar04b] resulting in a smooth crossover as seen on the study of the axial cloud size throughout the crossover. Fast magnetic field ramps were introduced to project the fermionic many-body state on the BCS side of the resonance into a molecular BEC state [Reg04b]. It was used to study the condensation in the crossover and found the striking result that also on the BCS side there is a BEC, which implies pair correlations. This same technique was later used by [Zwi04] for ^{6}Li instead of ^{40}K. They found a much larger condensate fraction on the BCS side, and suggested that it may be an indication of short-range correlations rather than long-range ones. The nature of the atom pairs through the resonance has been one of the most enigmatic properties of the resonant superfluid.

The measurement of the two-body, K_2, and three-body, K_3, inelastic coefficients that describe the atom number decay as modeled by [Rob00]

$$\frac{dN}{dt} = -\Gamma N - \int K_2 n^2 d\mathbf{x} - \int K_3 n^3 d\mathbf{x}, \tag{1.5}$$

was done much later in [Du09b]. Here Γ is the background collision rate, which does not depend on the density, and n is the total atomic density. The density corresponds to that of the 2D trap geometry used in the experiment. What was found is that for higher temperatures the K_3 alone describes the decay in the number of atoms; it decreases by two orders of magnitude when changing the interaction parameter from the mBEC side of the resonance to the collisionless regime. For lower temperatures it is a combination of K_2 and K_3 which accurately describes the decay. However, K_2 disappears on the BCS side of the resonance. Relating K_2 to the presence of pairs, this behavior of K_2 is taken as an indication that no pairing takes place on this side of the resonance.

1.1.4. Experiments in ultracold Fermi gases

Tan universal relations

Novel experiments related to the universality of the resonant superfluid measure what is known as the Tan relations [Ste10]. These relations were presented in a series of articles [Tan08c, Tan08b, Tan08a] and depend only on a quantity introduced therein called the *contact*. It is defined as the amplitude of the high-momentum tail of the momentum distribution and contains all the many-body physics of the system. Hence, the aforementioned experiment measured the contact for an ultracold gas of ^{40}K. It verified that, even though the contact depends on parameters like temperature, interaction strength, and density, the universal relations remain independent of them. More

specifically they measure the radial momentum distribution for the fermions during ballistic expansion, from which they reconstruct with an inverse Abel transformation the spherically symmetric momentum distribution for the fermion, $n(k)$. This in turn is used to calculate the contact,

$$C = \lim_{k\to\infty} k^4 n(k), \tag{1.6}$$

where k is the wave number in units of k_F, and $n(k)$ satisfies the normalization $\int_0^\infty d\mathbf{k} n(k)/(2\pi)^3 = 0.5$. Interestingly, they were *also* able to measure C using RF spectroscopy. In this case, the high-frequency tail of the transferred atoms distribution has an amplitude of $C/2^{3/2}\pi^2$ [Pie09]. It is also predicted that the transferred number of atoms scales with the frequency ν like $\nu^{-3/2}$ for large frequencies. Experimentally one has to minimize the final-state effects for the measurement to work. The outcome of their work is the behavior of C throughout the crossover: it goes to zero as $(k_\mathrm{F}a)^{-1}$ goes far into the BCS side and increases as one approaches the resonance, in accordance with the theory. Moreover, they verify the universal Tan relations with it.

Spectroscopic methods

Radio-frequency (RF) spectroscopy, in which atoms are transfered to an unoccupied state changing the projection of the nuclear spin, is another tool for studying the unitarity limited Fermi gas [Chi04b]. It was used to observe fermionic pairing at different temperatures and interactions strengths; it allowed the measurement of the pairing gap. Also optical molecular spectroscopy was used to explore the wave function of the pair correlations in the crossover [Par05]. It was theoretically suggested that, for atoms such as ^{6}Li, the wave function of the pairs, ψ_p, is the superposition of the atoms in the incoming channel, ϕ_a, and the molecules in the closed channel, ψ_m [Dui04]. Namely,

$$|\psi_p\rangle = Z^{1/2}\,|\psi_m\rangle + (1-Z)^{1/2}\,|\phi_a\rangle\,, \tag{1.7}$$

where Z is the fraction of pairs in the closed channel. By measuring the loss in the closed channel in the presence of the molecular probe beam they were able to measure Z. The changing nature of the pair correlations is seen as it decreases from about 1 for the mBEC-limit to close to 0 towards the BCS limit. Later another set of RF spectroscopy experiments were done in which the size of the fermion pair is determined after minimizing final state effects [Sch08c]. To achieve this different initial spin states were chosen: instead of creating a superfluid with the commonly used two lowest hyperfine states of ^{6}Li, $|1\rangle$ and $|2\rangle$, the states $|1\rangle$ and $|3\rangle$ where employed. The pair size, ξ, can be determined from the spectral linewidth of the dissociation spectrum, E_w, given by $\xi^2 \approx \hbar^2/mE_w$. Experimentally E_w is taken as the width of the peak. On resonance the resulting pair size is smaller than the interparticle spacing and the smallest found so far for a fermionic superfluid. In general, the size in the BEC-BCS crossover is found to increase from the two-particle correlation length, ξ_pair, in the mBEC-limit to about $2,5\xi_\mathrm{pair}$ on the BCS side of the resonance.

A particular case of RF spectroscopy was used to investigate the single-particle excitation spectrum of the many-body system [Ste08]. Momentum-resolved RF spectroscopy, also known as photoemission spectroscopy, likewise couples one of the two spin states to an unoccupied third state. Yet, it must fulfill two additional conditions: the interaction energy has to be small enough such that the ideal Fermi gas dispersion, $\epsilon_k = \hbar^2k^2/2m$, holds and final-state effects are negligible; and the collision rate has to be low as not to wash away the momentum information. The results show the energy dispersion of the system. It was clearly shown that the molecular branch appearing and

separating from the free atom dispersion as the interactions are increased from a weakly interacting Fermi gas to a mBEC.

Some recent studies have focused on the pseudogap region of the unitarity limited gas [Gae10, Per11]. The pseudogap corresponds to a temperature region above T_c in which pair-correlation are present, but the cloud is not superfluids. In this region the gas still has a BCS-like dispersion, $E_s = \mu \pm \sqrt{(\epsilon_k - \mu)^2 + \Delta^2}$, where $\epsilon_k = \hbar^2 k^2/2m$ is the kinetic term, k is the fermion wave vector, and Δ is the pair-correlations order parameter. In the weakly interacting gas, where Cooper pair formation and their condensation is simultaneous, Δ becomes the superfluid order parameter. Hence, the fact that $\Delta \neq 0$ in the absence of superfluidity in the pseudogap regime is what differentiates it from the normal BCS state. It leads to a change of behavior in the dispersion for temperatures above T_c: whereas the conventional BCS case would lead to a free particle dispersion, for the strongly interacting gas the lower branch of E_s changes slope from positive to negative at k_F. By use of momentum-resolved RF spectroscopy the dispersion was measured for different temperatures [Gae10]. The signature of $\Delta \neq 0$ for temperatures both below and above T_c was measured and, for $T > T_c$, taken to pertain to the incoherent pairing correlations of the pseudogap. In following work it was established that the backbending of the dispersion actually happens at a Luttinger wave vector $k_L \neq k_F$, elucidating the existence of a remnant Fermi surface for the strongly interacting gas [Per11]. The study for different temperatures and interaction strengths evidence the deviations from the normal Fermi liquid theory, and showed the evolution of the pseudogap. Also, new RF spectroscopy data is analyzed including final-state and trap effects in [Pie11]. The evolution of the spectra as a function of temperature is explained with this new model. It emphasizes that both final-states and trap effects are needed to properly describe the results. Moreover, it makes it possible to explain the evolution of the gas from a phase where the pairing-gap and pseudo-gap are present at $T < T_c$ to a phase where the pseudo-gap and no-gap exist at $T > T_c$.

Bragg spectroscopy is a widely used tool [Vee08, Ina08b, Kuh10, Zou10, Kuh11b, Kuh11a]. Bragg spectroscopy, as opposed to RF spectroscopy, does not change the internal state of the atom, so there are no final-state effects to be considered. The property of Bragg spectroscopy, rather, is to transfer momentum into the system, even larger than $\hbar k_\mathrm{F}$. Interestingly, the first time that atoms were out coupled from a cloud using a Bragg pulse was used to look at the critical temperature and condensate fraction for different magnetic fields deep into the mBEC side and in the crossover region [Ina08b]. The first report of using a Bragg pulse with spectroscopic purposes in the BEC-BCS crossover was done in [Vee08]. The measured center of mass displacement was related to the momentum transferred to the cloud by the Bragg pulse, which in turn is related to the dynamic structure factor. The transition from atomic to molecular excitations was observed in the spectra. Moreover, the two-body correlation between states $|1\rangle$ and $|2\rangle$, $g^{(2)}_{\uparrow\downarrow}(r)$, was studied by looking at its Fourier transform through the static structure factor,

$$S_{\uparrow\downarrow}(q) = n \int dr [g^{(2)}_{\uparrow\downarrow}(r) - 1] e^{iqr}, \tag{1.8}$$

where q is the wave vector of the Bragg pulse. It was seen that the value of the static structure factor dropped by half when going from the BEC to the BCS limit of the crossover as a result of a drop of $g^{(2)}_{\uparrow\downarrow}$. A continuation of this work by [Kuh10, Kuh11b] used the measurement of the $g^{(2)}_{\uparrow\downarrow}$ to test universal relations in the crossover region. It has been shown that the two-body correlation

function depends on C contained in the Tan relations,

$$g^{(2)}_{\uparrow\downarrow}(r) = \frac{C}{16\pi^2 N k_{\mathrm{F}}}\left(\frac{1}{r^2} - \frac{2}{ar}\right). \tag{1.9}$$

By measuring the static structure factor throughout the resonance region they were able to show that it follows a universal law that is a direct result of Tan's relations. Indeed, as predicted by Tan, the contact decreases and eventually disappears as we go from the BEC limit to the BCS side. Later theoretical work using a random phase approximation (RPA) calculation came up with a model for the dynamic and static structure factors that properly describes the experimental results [Zou10]. Finally, an extension of this research used the temperature dependence of the static structure factor to measure the change of C as a function of T/T_{F} [Kuh11a]. What is found is that $C \to 0$ for $T/T_{\mathrm{F}} > 1$.

Thermodynamic studies

First thermodynamic studies exploring the crossover region were done in [Bou04, Kin05b]. The experiment of [Bou04] was the first to introduce a cross-dipole trap in the study of the mBEC-BCS crossover. The purpose was to reduce the anisotropy of the cloud, *ie*, the elongated cigar-like shape of the gas, due to a single focused laser beam. The tight confinement and strong interactions led to a large condensate mean-field. This leads to a modification of the thermodynamics resulting in a large shift of T_{BEC}. Also, the partially condensed cloud's expansion is modified due to interactions, which affect the thermal cloud. Further, by measuring the anisotropy of the cloud, $\eta = \sigma_y/\sigma_x$, where σ_i is the rms width of the cloud along the i direction, they were able to study the expansion of the cloud across the resonance region. They found deviations from the expected hydrodynamic behavior, in particular on resonance, where the gas expanded nonhydrodynamically. In the experiment [Kin05b] the heat capacity was measured and thermometry in the crossover region was done.

However, a new generation of experimental studies revealing new thermodynamic properties of the unitarity limited Fermi gas have taken place [Luo09, Hor10, Nas10b], including the study of the equation of state [Nas10b, Nas10a, Nav10]. The entropy and the energy were presented in [Luo09], the internal energy in [Hor10], the equation of state for a uniform gas on resonance for different spin-imbalance mixtures in [Nas10b], and finally across the resonance in [Nav10]. The equation of state for a uniform gas in the unitarity limit is given by [Ho04],

$$P(\mu_1, \mu_2, T) = P_1(\mu_1, T) h\left(\eta = \frac{\mu_2}{\mu_1}, \zeta = \exp\left(\frac{-\mu_1}{k_{\mathrm{B}}T}\right)\right), \tag{1.10}$$

where $P_1(\mu_1, T) = -k_{\mathrm{B}}T\lambda_{\mathrm{dB}}^{-3}(T) f_{5/2}(-\zeta^{-1})$ is the pressure of a noninteracting Fermi gas for one of the spin components, and $f_{5/2}(z) = \sum_{n=1}^{\infty} z^n/n^{5/2}$. The function $h(\eta, \zeta)$ is universal and contains all the thermodynamic information. To circumvent the density profile inhomogeneity introduced by the trapping potential one measures the pressure locally [Ho10],

$$P(\mu_{1z}, \mu_{2z}, T) = \frac{m\omega_{\mathrm{r}}^2}{2\pi}(\tilde{n}_1(z) + \tilde{n}_2(z)), \tag{1.11}$$

where the doubly-integrated density profiles $\tilde{n}_i(z) = \int dxdy n_i(x, y, z)$ are for each spin state i. This results in the following two advantages: one measures the equation of state directly, and each pixel along the axial direction z gives a measurement for the now discretized $h(\eta(z_i), \zeta(z_i))$. The

experiment finally showed that the unitary gas is a strongly correlated system that obeys Fermi liquid theory. Interestingly, the equation of state at which they arrive is similar to the one calculated from the internal energy measurement done by [Hor10].

Spin degree of freedom

In addition to $1/(k_{\mathrm{F}}a)$ and T, also the spin degree of freedom of the gas has been experimentally controlled and studied [Par06a, Zwi06, Shi06, Par06b, Li07, Par07, Shi08, Sch08a, Nas09]. In general one defines the local spin polarization, $\sigma = (n_\uparrow - n_\downarrow)/(n_\uparrow + n_\downarrow)$, to describe the local spin imbalance. The first observation was reported in [Par06a]. What was found is that after reaching a critical polarization the minority spin population is paired at the center of the trap, while the excess majority atoms are segregated around the paired core; the segregation as function of polarization was studied. Later vortices were studied as a function of degree of population imbalance [Zwi06]. It showed the decrease in the number of vortices in the paired cored as the polarization is increased, and confirmed the phase segregation between the two spin states, for different interaction strengths. The superfluid proved to be rather robust against population imbalance. The phase separation was further studied in [Shi06], where the effect of the phase separation on the density profiles was reported. The measurement was performed with a new imaging technique, that consisted in taking phase-contrast images and then doing a 3D image reconstruction of the density distributions. The results showed that the phase separation occurs for smaller spin imbalances as the interaction strength increases. In addition, the central paired core shows a "flattop" distribution of the total density. Sharp phase boundaries between the segregated phases were observed and discussed in the context of a first-order phase transition in [Par06b, Li07]. The temperature dependence of the deformation exposed that for higher temperatures, but still $T < T_c$, the sharp boundary becomes a partially polarized domain wall joining a uniformly paired core and a fully polarized outer region. The spin imbalanced mixture was studied in the crossover in [Par07]. The pair correlations were found to be continuous throughout. Moreover, the data seemed to have the same magnetic field dependence as the order parameter, suggesting that a single-channel model properly describes the system. The superfluid gap order parameter was measured in [Sch08a]. By combining tomographic RF spectroscopy [Shi07] and *in situ* phase contrast imaging with 3D reconstruction of the density profiles they were able to study the pair correlations in the domain wall uniting the superfluid to the polarized normal state. The comparison of the spectra for the majority and minority components exposed a smooth crossover in which the majority component shows a double-peak spectrum from which the superfluid gap can be determined. This study was followed by the mapping of the phase diagram (σ, T). The measured spatial density profile of the minority component showed a discontinuity; this striking result is a signature of a first-order superfluid-to-normal phase transition. A second-order phase transition, at which the density profile and condensate fraction vary smoothly, has also been characterized. In addition, the tricritical point, at which the first- and second-order phase transition lines meet, was determined. Finally, the dynamics of the polarized Fermi gas has been studied using collective modes [Nas09]. The excitation of the compression mode for different spin imbalances established a region of low polarization for which the gas behaves hydrodynamically. For intermediate polarizations, where a superfluid is still present, both spin components oscillate in phase. For large polarization the two spins oscillate independently, giving rise to a polaron breathing mode and allowing the study of a Fermi polaron. A polaron is an impurity surrounded by a Fermi sea, *ie*, an atom of one species surrounded by a cloud made up of atoms of another species in the ideal case. However, in practice on finds a minority component surrounded by the

phase segregated majority atoms. The effective mass of the polaron was inferred.

Interestingly, likewise for spin balanced mixtures spin segregation has been observed [Du08], and subsequently spin currents [Du09a]. For a spin balanced mixture near the zero crossing of the scattering length the spatial densities segregate markedly if the two states are prepared in a coherent superposition [Du08]. The segregation was found to be temperature independent. Its time evolution was observed, finding that the buildup takes a couple hundred ms and the decay several seconds. The study concluded that the experimental data could not be explained by the current available theories, namely, spin-wave theory. However, a later experiment focused on spin currents in this system [Du09a]. By introducing the notion that the spin vector of each atom is correlated to its energy, resulting in a nearly undamped spin wave, the observed spin segregation is explained. Further, the spin current associated with this segregation can also be understood in these terms. The cause of the observed spin dynamics lies in the fact that the magnetic moment of the two spin species is not identical. Hence, the finite curvature of the bias magnetic field introduces slightly different axial trapping frequencies for both of them. This small difference correlates the precession of an atomic spin in the horizontal axial plane with the energy of the atom, giving rise to a spin wave. Moreover, the spin current can be reversed by changing the sign of the interactions and applying a π pulse to the spin vector perpendicular to the horizontal axial plane. In this case the spatial density distributions go back to their initial unsegregated profiles.

Lower dimensions

The trapping potential has been modified to study low dimensions [Lia10], and recently complicated potentials have been engineered together with high-resolution imaging [Zim11]. A spin polarized Fermi gas in a 1D tube has been studied in [Lia10]. The interest in these systems lies in the theoretical prediction by Fulde and Ferrel [Ful64] and Larkin and Ovchinnikov [Lar65] of an exotic state in which pairs with finite momentum lead to magnetism (FFLO state). For the 1D case it is anticipated that the phase diagram is dominated by this FFLO state. Experimentally, the desired spin imbalance is first created and then loaded into a 2D optical lattice. The bias magnetic field is tuned to the BCS side of the FB resonance, where the 1D interactions are strongly attractive. The results reveal that, whereas for the 3D case the center of the trap remains fully paired as polarization is increased, for the 1D tube a partially polarized region at the *center* of the trap is formed for low polarization. This region extends outwards as the polarization increases until it covers the whole cloud. If the polarization is further increased then the *edge* of the cloud becomes fully polarized after which point it starts growing inwards. This first study may pave the way for further research on FFLO physics.

Other aspects of low dimensions in Fermi gases have also been studied. Investigating a weakly interacting Fermi gas the transition from 3D to 2D at low temperatures has been studied in [Dyk11]. Taking advantage of the fact that $E_{\mathrm{F,2D}} = \sqrt{2N}\hbar\omega_r$ the number of atoms was carefully controlled to ensure that all the atoms are in the lowest transversal vibrational state in the low temperature limit. In this case $E_{\mathrm{F}} \ll \hbar\omega_z$ and the gas is 2D. An experimentally accessible value of the critical atom number below which the gas becomes 2D is given by

$$N_{\mathrm{2D}} = \frac{\lambda}{2}(\lambda + 1), \tag{1.12}$$

where $\lambda = \omega_z/\omega_r$ is the aspect ratio of the trap frequencies. To prove the crossover from 3D to 2D the aspect ratio between the axial and radial radii was recorded for different atom number. At low

enough atom number shell structures are observed, caused by the filling of individual transverse oscillator states in the quasi-2D regime.

Beyond two states

Beyond two-spin mixtures also systems of three components have been researched [Ott08, Wen09, Huc09, Lom10b]. As opposed to the two spin mixture in which Pauli blocking greatly suppresses three-body processes, the three component mixture was expected to show Efimov physics and, perhaps more interesting, relate to the color superconductivity of quantum chromodynamics (QCD). The first report on a balanced mixture of the three lowest hyperfine states of ^{6}Li in a degenerate Fermi gas was done in [Ott08]. The collisional stability of the mixture was studied as a function of magnetic field by looking at loss features from 0 up to 750 G. However, above 600 G a two-body Feshbach resonance between states $|1\rangle$ and $|3\rangle$ increases the inelastic processes. Hence, the loss features seen are explained in terms of two- and three-body inelastic processes, by looking at the decay rate and extracting the K_3 coefficient up to 600 G. Most interesting was a broad resonance caused by all three spin states. Soon after the stability of the system was studied up to 950 G, namely, including the three broad two-body Feshbach resonances [Huc09]. It corroborated the previous measurement of K_3 and confirmed the remarkable stability of the system against two-body loss processes. It was soon after proposed that some of the loss features could be explained in terms of Efimov trimers [Nai09], followed by a reinterpretation of the data in [Wen09], albeit using the theory by [Bra06] modified for three distinguishable fermions.

Efimov's theory, [Efi70, Efi71, Efi79], found a universal regime in which an infinite number of trimers are formed when the two-body interactions become resonant. The binding energy of these three-body bound states scale with the factor $e^{-2\pi/s_0}$, where $s_0 = 1.00624$ for nonidentical fermions with same mass. By dropping the assumption that the lifetime of the trimer is independent of the magnetic field, the three-body recombination with a magnetic field dependent lifetime of the trimer was used in [Wen09] to explain their results. Assuming that a trimer will decay into a deeply bound dimer and a free atom they used the three-body coefficient

$$K_{3,\mathrm{deep}}(a) = \frac{c\sinh(2\eta_*)}{\sin^2[s_0\ln(a/a_*)] + \sinh^2\eta_*}\frac{\hbar a^4}{m}. \tag{1.13}$$

Here c is a universal constant, and a_* and η_* are parameters that completely characterize the three-body recombination. More precisely, η_* describes the width of the resonance and hence the lifetime of the Efimov state. The parameter $a_* = a(e^{\pi/s_0})^{-n}$, where $n \in \mathbb{Z}_{\geq 0}$, fixes the position of the loss resonance by relating the short-range interaction potential to the three-body bound state. In the case of three distinguishable fermions one replaces a by an effective interaction parameter

$$a_m^4 = \frac{1}{3}\left(a_{12}^2 a_{13}^2 + a_{12}^2 a_{23}^2 + a_{13}^2 a_{23}^2\right). \tag{1.14}$$

The data is fitted to Eq.(1.13) using c, a_*, and η_* as free parameters. The model properly reproduces the behavior of the data, in particular for the lower magnetic field resonance, confirming the existence of an Efimov trimer.

Other aspects of the Efimov trimers were later studied. For instance, by using an RF pulse an excited trimer state was created [Wil09]. By looking at the recombination rate K_3 at magnetic fields around 900 G a loss feature was observed. At this magnetic field the trimer crosses the

three-atom scattering threshold associated with the first excited state of the Efimov spectrum. In another experiment an RF pulse was also implemented for the creation of trimers [Lom10a]. In it, the RF pulse was used with spectroscopic purposes: the binding energy was measured using the RF pulse to *form* the trimers, instead of using it to dissociate the molecules as in the usual RF spectroscopy method. The reason for this approach is that the trimers are expected to have very short lifetimes, which makes the preparation of macroscopic samples unfeasible. The measurement of the binding energy was in agreement with theories including up to nonuniversal corrections.

Also nonuniversal trimers have been reported [Nak10]. Two loss features were observed: one at the position where the energy of a ground state Efimov trimer equals that of an atom-dimer threshold; and the other at the position where the energy of the first excited state of an Efimov timer crosses the same atom-dimer threshold. The position of these loss features deviates from the universal predictions. This deviation was further studied in the context of the experimental study of the trimer binding energy [Nak11]. Precision RF spectroscopy of the binding energy showed its temperature dependence at different magnetic fields. For the low-temperature limit, where the shift of the spectra is minimized, the results deviated from the previous measurements and theoretical predictions.

Moving on beyond trimers new experimental research has focused on few-body physics [Ser11]. States with 1 to 10 particles are prepared and their interactions tuned by means of a FB resonance. To generate the required small-volume optical dipole trap with large level spacing a laser beam is tightly focused to a waist a couple of microns large. The desired number of atoms is then regulated by controlled spilling using a magnetic field gradient. The precise control of atom number opens up the possibility to study properties and applications of few-body physics.

p-wave pairing

Other experiments have focus on the creation of p-wave molecules [Gae07, Fuc08, Ina08a]. The lifetime and binding energy of p-wave molecules in ^{40}K was reported in [Gae07]. The lifetime was found to be 1 to 2 milliseconds, which makes it hard to pursue the production of condensates. In the case of ^{6}Li, the three possible p-wave molecules of the lowest two hyperfine states were studied in [Fuc08]. Only the ones involving state $|2\rangle$ were seen; their binding energy and lifetime reported. The lifetime found was in the order of tens of milliseconds, apparently due to vibrational quenching collisions with unpaired atoms, which are not removed. Regarding the $\langle 1| - \langle 1|$ p-wave molecule, it was observed in [Ina08a]. This work reported the dimer-dimer inelastic loss coefficients, the one-body decay coefficients, and the atom-dimer inelastic collisions coefficients, which are zero in some cases. The longest lifetime was found for the $\langle 1| - \langle 1|$ molecules, and it was about 20 ms. It became clear from this work that conventional forced evaporative cooling would not work for the direct formation these molecules.

Heteronuclear mixtures

Later also mixtures with different fermions [Tag08, Wil08, Voi09, Voi10, Spi09, Spi10, Tie10, Cos10, Nai11, Tre11] were created and studied. Unequal masses and different response to external fields increase the parameter space available for experiments. The first realization was presented in [Tag08], where ^{6}Li and ^{40}K were sympathetically cooled by evaporative cooling of ^{87}Rb. The cooling process was analyzed and it showed that a *catalytic* cooling of ^{6}Li by ^{87}Rb in the presence of ^{40}K enhances the cooling process. The quantum degenerate heteronuclear Fermi-Fermi mixture

and the degenerate Fermi-Fermi-Bose mixture were shown to be stable and good candidates for further studies. The first characterization of the Feshbach resonances between ^{6}Li and ^{40}K was reported in [Wil08]. As explained in this publication and references therein the mixture can rapidly decay via spin relaxation *if* exoergic two-body processes exist that preserve the total projection quantum number $M_\mathrm{F} = m_\mathrm{Li} + m_\mathrm{K}$ where the projection quantum numbers for energy level Li$|i\rangle$ and K$|j\rangle$ are given by $m_\mathrm{Li} = -i + 3/2$ and $m_\mathrm{K} = j - 11/2$. However, if one of the two species is in the absolute ground state and the other in a low-lying state, spin relaxation is strongly suppressed. The resonances observed were both s- and p-wave. They are quite narrow, indicating that they are closed-channel dominated.

Later bosonic molecules resulting from pairing two fermionic atoms were reported in [Voi09]. By means of an s-wave Feshbach resonance an heteronuclear pair was created and studied in the resonance region. The lifetime of the molecules close to resonance was found to be sufficiently long to allow the further study of this state. Subsequently the collisional stability of the mixture was further studied [Spi09], though in a slightly different configuration: one of the atomic species was prepared in a spin mixture with tunable interactions, in this case ^{6}Li in the vicinity of the broad FB resonance at 834 G; the other atom, in this case ^{40}K, weakly interacts with Li. At the end of the evaporation process one had a ratio $N_\mathrm{Li}/N_\mathrm{K} \approx 10^2$ between the two species. What was found is that for this setup there exists a wide region in which elastic collisions dominate over inelastic ones. This stability allows the use of the large Li cloud as a bath that takes away the heat from the K atoms as the two thermalize by simply holding both in the trap, *ie*, sympathetic cooling between the interspecies particles down to a doubly-degenerate sample. The potential of using the weakly interacting cloud as a probe of the many-body regime was put forward. The report of the long sought interspecies broad FB resonance appeared in [Tie10]. Together with a model to predict the position of the broad resonances the observation of one with a width $\Delta B = 1.5$ G was presented. The dependence of the relaxation rates on the mass was studied in [Cos10] for a s-wave resonance and was heralded as paving the way for the study of crossover physics in heteronuclear mixtures. Yet, the detailed experimental and theoretical study of the elastic and inelastic processes in this mixtures led to the crude conclusion that the lifetimes of the FB molecules are in the order of 10 ms, which may be too short for direct formation of a BEC. Moreover, it was found that in general atomic two-body collisions have a resonantly enhanced inelastic component that limits the lifetime of Fermi-Fermi mixtures with resonantly tunable interactions also to about 10 ms [Nai11].

Be that as it may, experiments have been performed in which interspieces strong interactions were created to study the hydrodynamic expansion of the mixture [Tre11]. In addition to the expected inversion of the aspect ratio of the expanding cloud, an effect in which the two clouds seemed to stick together was observed. One would have thought that, due to the different mass and confinement between the two species, the expansion would have happened at different rates. Nevertheless, there is an interspecies drag effect that leads to collective flow during expansion. Further understanding of the hydrodynamic expansion is still required.

Optical lattices

Besides the Feshbach resonance, optical lattices are also used to create strong correlations. First reported experimentally for degenerate fermions in [Mod03a], their work consisted of loading the atoms into a 1D lattice and studying basic properties of the resulting quasi-2D confinement. Later in the experimental studies of [Köh05] noninteracting fermions were loaded into a simple cubic 3D optical lattice, which gives rise to a band insulator. Such a system presents a model of electrons

in a solid, where the crystal lattice has a fundamental role, and is supposed to be an almost ideal realization of the Hubbard model [Jak98]. The Hubbard Hamiltonian [Hub63], including the harmonic potential of the dipole trap, has the form [Sch08b]

$$\hat{H} = -J \sum_{\langle i,j \rangle \sigma} \hat{c}^{\dagger}_{i,\sigma} \hat{c}_{j,\sigma} + U \sum_{i} \hat{n}_{i,\downarrow} \hat{n}_{i,\uparrow} + V_t \sum_{i} \left(i_x^2 + i_y^2 + \gamma^2 i_z^2 \right) \left(\hat{n}_{i,\downarrow} + \hat{n}_{i,\uparrow} \right) . \tag{1.15}$$

Here i, j are the different lattice sites; σ refers to the two possible spin states; $\hat{c}^{\dagger}_{i,\sigma}, \hat{c}_{j,\sigma}$ refer to the creation and annihilation operators of a fermion; $\gamma = \omega_z/\omega_\perp$ is the aspect ratio of the trap; and $\hat{n}_{i,\sigma}$ is the atom number. The relevant energy scales are the hopping matrix element, J, the onsite interaction, U, and the harmonic confinement, $V_t = m\omega_\perp^2 d^2/2$, where d is the lattice constant. Usually the energy parameters are given in terms of the recoil energy, $E_r = \hbar^2 k^2/2m$, where $k = 2\pi/\lambda$. Depending on the ratio between these energy scales one finds one of the following three states: a *metallic* phase, for which $J > 0$ and $U \ll E_t \ll 12J$; a *Mott-insulator* with localized atoms in single occupied sites and $U \gg E_t > 12J$; and a *Band-insulator* that has fully doubly occupied sites and $E_t \gg 12J$. In view of these phases the outcome of the experiment [Köh05] was the measurement of the Fermi surface as a function of density, which clearly showed the filling of the Brillouin zone, *ie*, the band insulator state. This agreed with theoretical predictions. However, also the delocalization of the fermions for incommensurate filling was studied, and even the interactions by use of a bias magnetic field. This latter part was not in full agreement with the theoretical model.

A further study of the insulating phase was reported in [Sch08b]. By determining the global compressibility of the repulsive interacting gas from the cloud size measurement, they were able to study all the different phases of the Hubbard model. For the attractively interacting gas an anomalous expansion was measured in [Hac10]. The cloud expanded instead of contracting as the repulsive interaction was increased. The reason for this effect turned out to be the difference between pair formation within the first band of the optical lattice and in its absence. Finally, also excitations have been studied [Sen10]. The nonequilibrium dynamics and decay of an artificially created double occupancy in the presence of strong repulsive interactions were analyzed. The excitations are found to be surprisingly long lived, which is interpreted as a limitation for the rate at which lattice parameters can be changed while maintaining equilibrium.

Subsequently fermionic dimers were created by means of a Feshbach resonance and loaded into an optical lattice. First reported in [Stö06] the control over the occupancy of the lattice and the methodology to perform thermometry were established. Soon after evidence of superfluidity of the condensed dimers in the optical lattice was presented in [Chi06]. By means of high-contrast interference measurements the presence of a superfluid, namely, long-range phase coherence, was studied for both sides of the Feshbach resonance and as a function of lattice depth. In the experimental work of [Wel09] a novel technique to measure the temperature of the gas was developed and successfully used to measure temperatures as low as 1 nK. The method consists of introducing a magnetic field gradient that segregates the two spin states. Relaying on the fact that at the interface of the two spin domains temperature dependent spin excitations will occur, the measurement of the excitation width gives the temperature of the system. The mean spin, $\langle s \rangle$, as a function of position obeys

$$\langle s \rangle = \tanh\left(-\beta \Delta\mu B(x)/2\right) , \tag{1.16}$$

where $\beta = 1/k_B T$, $B(x)$ is a position dependent magnetic field, and $\Delta\mu$ is the difference between

the magnetic moments of the two spin states. A fit to the measured spin distribution directly gives the temperature.

Recently nearest-neighbors spin correlations in an optical lattice have been studied for repulsive interactions [Gre11]. Using the modulation of the lattice to create double occupancy of a lattice site, the neighboring spin order can be probed. In other words, only neighboring sites with opposite spins could lead to a doubly occupied site. The nearest neighbor correlations are probed for different temperatures by looking at the evolution of the double occupancy as a function of modulation time to get the production rate. From this the correlator is obtained, which decreases as the temperature increases.

Antibunching

Another feature of the ultracold Fermi gas that has been studied is antibunching. For a weakly interacting trapped gas (without a lattice) the study of *local* density fluctuations was done by looking at the cloud *in situ* [Mül10]. This probes the position dependence of the density fluctuations, which reaches a maximum at the center of the trap where the density is largest. However, antibunching has also been observed in optical lattices.

In an optical lattice fermion antibunching was studied in [Rom06]. Spatial antibunching here reflects the fact that Pauli blocking prevents two atoms occupying the same Bloch state. Hence, bearing in mind that the Bloch state is a superposition of plane waves, if an atom is detected at a given position, no other atom will be detected at a position $l = 2\hbar kt/m$ from it, where t is the time-of-flight after release from the optical lattice, and k the wave vector of the laser light. By looking at the shot-noise after time of flight it was possible to study the correlation amplitude as a function of temperature. Fermion antibunching was also reported in [Ian06], where the distance between two detectors was actually varied.

1.2. Dynamics

One of the most interesting aspects of the quantum fluid is its dynamics. One distinguishes between the hydrodynamic and the near-collisionless regimes. The relevant time scales to consider to differentiate between them are the trap frequency, ω, and collision time, τ_{R}. Thus, if a particle undergoes many collisions during one oscillation period of the trap, the fluid is hydrodynamic: $\omega\tau_{\mathrm{R}} \ll 1$. From this criterion it is easy to introduce the near-collisionless regime: in such a system a particle hardly undergoes a collision in the timescale of the inverse trap frequency, $\omega\tau_{\mathrm{R}} \gg 1$. Moreover, in the case of a superfluid, the fluid is always hydrodynamic due to the long range order of the system. For a nonsuperfluid in the hydrodynamic regime the collisions ensure the long range interactions. Hence, in the resonant region one finds quantum hydrodynamic behavior due to the superfluid and collisional hydrodynamic behavior of the nonsuperfluid state [Mad27, Str04]. One way to fulfill the hydrodynamic condition is by changing the trap geometry: in the elongated cigar-shape trap geometry the low axial trap frequency facilitates being in the hydrodynamic regime. For fermions, one may also use a FB resonance to have unitarity limited interactions, at which point τ_{R} is very small.

It should be emphasized that measurements showing hydrodynamic behavior do not suffice to show superfluidity: as mentioned above there are two possible reasons for hydrodynamic behavior. Bearing this in mind collective modes probe different aspects of the strongly interacting cloud, but

not superfluidity unequivocally. Thus, the presence of quantized vortices has been the standard to show the presence of superfluidty. Collective modes are also a tool that allows the study of other dynamics, namely, one can use the quadrupole mode to study rotational dynamics of the gas. For instance, the quenching of the moment of inertia by the superfluid, have tried to offer alternative methods to test for superfluidity. Understandably many studies have focused on characterizing the superfluid, *eg*, the speed of sound and viscosity. Yet other experiments have focused on the rotational properties of the normal state to study the collisional hydrodynamic regime. In what follows we present experimental studies of the dynamic properties of the degenerate Fermi gas.

1.2.1. Experimental studies

Collective modes

Collective modes can be used as a tool to study the dynamics of the gas in the crossover: the frequency and damping are in general interaction strength dependent, in particular when the gas changes from the collisional regime to the near-collisionless. The trapped cloud oscillates with a certain frequency defined by the confining potential. Depending on the collective mode excited are the properties of the cloud that can be studied: for the dipole mode, the center of mass oscillates periodically with the trap frequency, allowing the measurement of the trapping potential; for the compression mode [Alt07a], the density of the cloud changes, giving insight into the equation of state; and in the case of the quadrupole mode [Alt07b], in which the density is constant, the change in frequency of the oscillation allows to identify the position at which the collisional regime changes.

The temperature dependence of the collective modes has also been used to study the properties of the cloud. For instance, the scissors mode serves to study the finite-temperature dynamics [Wri07], which show hydrodynamic behavior well above T_c. Another study with collective modes showed the effect of pair correlations with unitarity limited interactions[Rie08], and showed that the theoretical model including both Pauli blocking and pairing correlations best describes the measured behavior.

Theoretical work specific to collective modes in Fermi gases can be found in [Str04, Hei04, Hu04, Kim04b, Bul05]. First experimental studies using collective modes were done in the low-temperature limit to avoid the possibility of the normal state being collisional hydrodynamic, *ie*, there is almost no normal state. Temperature and magnetic field dependence of the breathing mode was studied in [Kin04a]. This measurement showed the decrease of the damping rate as a function of temperature and the measurement of an oscillation frequency corresponding to that of the hydrodynamic regime. They argued that since the observed behavior could not be explained by collisional hydrodynamic theory nor by the collisionless model the gas had to be a superfluid. Another experiment further studied the magnetic field dependence of the compression mode both in the axial and in the radial directions of a cigar-shape trap [Bar04a]. Both the mode frequency and the damping rate showed some unexpected behavior when joining the BEC- to the BCS-limit. In particular the radial compression mode showed a sharp increase of the damping at the same magnetic field position where the frequency changed abruptly. This was interpreted as a signature of the transition from hydrodynamic to near-collisionless regimes. Other observed effects where a downshift of the frequency where the opposite was expected, and the shift on resonance being larger than predicted. These first revealing yet inconclusive studies on collective modes, in particular pertaining superfluidity, fueled further studies on dynamics and collective modes.

Vortices

Superfluidity was finally directly proven when a lattice of vortices was created and studied throughout the crossover [Zwi05]. This extensive study of vortices in the strongly interacting Fermi gas consisted of generating a vortex lattice at different magnetic fields. In addition, the vortex lattices had a regular number and charge of the vortices, which was a further indication of the quantization of the vortices expected for a superfluid. Last, also the decay rate of the vortices was measured.

Rotational dynamics at finite temperature

Some studies have further focused on the properties of the rotational dynamics of the resonant superfluid at finite temperatures [Cla07, Rie09, Rie11]. First research in [Cla07] studied the hydrodynamic expansion of a rotating strongly interacting Fermi gas. What was observed is that the known inversion of the aspect ratio of an elongated cloud during hydrodynamic expansion is suppressed as a function of the angular momentum transferred to the thermal component of the trapped cloud. More specifically, the cloud does not reach an aspect ratio of one. This nonequilibrium situation is related to the irrotational flow in the cloud, and can be present in both the superfluid and the collisional hydrodynamic normal phase. In other work the angular momentum of the cloud was inferred from the precession of the quadrupole mode [Rie09]. The decay rate of the angular momentum throughout the resonant region showed a minimum around the FB resonance. Further, by comparing the measured decay rate to the theoretical prediction for a Boltzmann gas, the relaxation time of the gas could be extracted. This, in turn, allowed for a characterization of the hydrodynamic degree of the gas, finding indeed $\omega\tau_{\mathrm{R}} \ll 1$. Using these tools to measure the angular momentum of the cloud, the equilibrium situation in which the normal state slowly rotates in presence of a superfluid fraction in the trap was studied in [Rie11]. The purpose was to study the quenching of the moment of inertia due to the presence of a superfluid fraction, which is irrotational. Using a controlled heating scheme, the measurement of the angular momentum of the gas allowed the inference of the quenching of the moment of inertia as a function of temperature. It gives a temperature range over which the phase transition may occur.

Speed of sound

Other experiments related to the dynamics of the gas have looked at the speed of sound [Jos07], together with the critical velocity [Mil07]. The normalized sound velocity, c_0/v_{F}, where $v_{\mathrm{F}} = \hbar k_{\mathrm{F}}/m_a$ is the Fermi velocity, was measured throughout the crossover and deep into the mBEC side. It was found that it decreases as the interactions are tuned from the BCS to the BEC side of the resonance, and seemed to saturate as one went deeper into the mBEC side. In addition, the universal property that the speed of sound should be independent of the density of the gas on resonance was confirmed. The critical velocity in the crossover was measured in [Mil07]. In this interaction regime two effects may limit superfluid flow: pair breaking, and sound waves. The superfluid velocity was predicted to show a peak in the transition regime from a state where one effect dominates to another where the other does. This is indeed what was measured by varying the velocity of a moving lattice and registering the value at which dissipation sets in for different interaction strengths. A pronounced maximum was found on resonance, indicating that superfluidity is most robust around this point.

Viscosity

Interest was quickly directed towards the viscosity of the resonant superfluid [Kov05, Sch07a, Tur08, Cao11]. In the theoretical work [Kov05] the shear viscosity of a fluid is used to characterize how close it is to being a perfect fluid. By using String theory methods a lower bound for the ratio between shear viscosity, η, and entropy per unit volume, s, is derived

$$\frac{\eta}{s} \geq \frac{\hbar}{4\pi k_{\mathrm{B}}}. \tag{1.17}$$

It was proposed that strongly interacting Fermi gases may be a tool to test this bound since they have a finite shear viscosity at nonzero temperature. Moreover, since this bound also applies, for instance, to quark-gluon plasmas (QGP), the ultracold Fermi gas offered a laboratory to test completely different systems. In the work of [Sch07a] the measured damping of the radial breathing mode in [Kin05a] was used to extract the ratio η/s on resonance as a function of temperature. It was found that the value near the critical temperature is the closest that is known to the proposed lower bound, except, probably, for QGP. The radial breathing mode was again studied experimentally, but now with an emphasis on this quantum viscosity [Tur08]. They wrote the ratio as

$$\frac{\eta}{s} \simeq \frac{\hbar}{k_{\mathrm{B}}} \frac{\langle \alpha \rangle}{S/k_{\mathrm{B}}}, \tag{1.18}$$

where $\langle \alpha \rangle$ is the trap average of a universal function determining the shear viscosity, and $S = S_{\mathrm{Tot}}/N$ is the entropy per particle. The former can be extracted from the measured damping rate of the mode, $1/\tau$, and the latter has been measured as a function of energy [Luo07]. Their results place the ratio η/s of the strongly interacting Fermi gas just above that of the QGP and very close to the quantum limit set by String theory, and well within the quantum viscosity regime. Finally, improved precision in the experimental determination of η allowed the investigation of two universal regimes for the viscosity. On the one hand, at $T < T_{\mathrm{F}}$ one finds the universal quantum scale for the viscosity $\eta \propto \hbar n$, where n is the density. On the other hand, for $T > T_{\mathrm{F}}$ the scale is set by $\eta \propto T^{3/2}/\hbar^2$. The two regimes were verified and the $T^{3/2}$ clearly shown.

1.2.2. Collective modes

With respect to the collective modes in the hydrodynamic regime we elaborate on the discussion. In the case of a quantum gas in the zero-temperature limit one starts the theoretical description from the continuity equation and classical Euler equation,

$$\frac{\partial n}{\partial t} = -\nabla (\mathbf{v} n) \text{ and} \tag{1.19}$$

$$\frac{\partial \mathbf{v}}{\partial t} = -\nabla \left(\frac{\mathbf{v}^2}{2} + \frac{V_{ext}(\mathbf{r})}{m} + \frac{\mu(n)}{m} \right) \tag{1.20}$$

respectively. These are a set of coupled differential equations for the density, n, and the velocity field, $\mathbf{v}$. The Euler equation further depends on the confining potential, $V_{ext}(\mathbf{r})$, and the chemical potential, $\mu(n)$. The density dependence of the chemical potential in the crossover region can be conveniently described by a power law, $\mu(n) \propto n^{\gamma}$, where the polytropic index γ depends on the interaction strength [Hei04]. For instance, for $\gamma = 1$ one recovers the weakly interacting BEC

equation of state derived from the Bogoliubov theory, where as for $\gamma = 2/3$ one finds the ideal Fermi gas relation. The task is then to solve the coupled differential equations.

The interest in higher order collective modes began when they were proposed as a tool to investigate second sound in the context of a fermionic superfluid with resonant interactions [Tay09]. The first attempt to observe second sound was in a cloud of ultracold bosonic atoms [Sta98]. It recorded a frequency shift in the dipole mode frequency, presumably as a result of an out of phase oscillation between the thermal and superfluid components. Later experiments showed the superfluid and normal components of the boson cloud oscillating out of phase, albeit in nonequilibrium. By the time that the system reached equilibrium the two components were oscillating in phase [Mep09b]. A description of sound propagation in terms of the two-fluid model was done in [Mep09a]. Yet, second sound in ultracold degenerate gases has remained elusive.

1.2.3. Work presented in this thesis

This thesis mainly concerns itself with the direct study of the dynamics of an ultracold Fermi gas with unitarity limited interactions at finite temperature. The hydrodynamic behavior of the gas is studied using low-lying collective modes and the rotational properties of the degenerate gas, and as of late using higher order collective modes. The purpose has been to characterize the resonant superfluid and distinguish between quantum and collisional hydrodynamic. The ultimate goal would be to use higher order collective modes as a tool to prove second sound, which is the property that, unlike quantized vortices, distinguishes resonant from weakly interacting superfluids.

The structure of the thesis is as follows: in chapter 2 we discuss the *Finite-temperature collective dynamics of a Fermi gas in the BEC-BCS crossover*. Particularly relevant to this work is the existence of a temperature domain above the critical temperature where the noncondensed state is also hydrodynamic. In chapter 3 we focus on the *Collective oscillations of a Fermi gas in the unitarity limit: Temperature effects and the role of pair correlations*. Different collective mode oscillations are measured for temperatures up to about the degeneracy transition temperature. We find that to properly describe the behavior of the gas and its transition from hydrodynamic to near-collisionless one has to include both pair correlation and Pauli blocking. In chapter 4 we move on to the rotational study of *Lifetime of angular momentum in a rotating strongly interacting Fermi gas*. In this case the decay of the angular momentum of the hydrodynamic noncondensed state is used to calculate the relaxation time of the gas, revealing collisional hydrodynamic behavior below theoretically expected temperatures. The know-how to introduce angular momentum into the cloud is used in chapter 5 to study the *Superfluid quenching of the moment of inertia in a strongly interacting Fermi gas*. In this experiment the different nature of the two coexisting hydrodynamic fluids is seen in the effect of the reduced moment of inertia caused by the irrotational nature of the superfluid component. In an experiment not directly related to the study of the dynamics of the cloud, further observation of hydrodynamic behavior on resonance is seen in chapter 6 in the *Observation of interference between two molecular Bose-Einstein condensates*. The hydrodynamic nature of the clouds prevents their overlap, resulting in no interference fringes, but rather in a hydrodynamic collision. Finally, we present our experimental investigation of the *higher order collective modes on resonance in the low-temperature limit* in chapter 7. We established the experimental technique to excite them and the methodology to analyze the resulting density oscillation. The robustness of the excitation suggests that indeed they may be a useful tool to further study two-fluid hydrodynamics on resonance at finite temperature.

2. Publication: Finite-Temperature Collective Dynamics of a Fermi Gas in the BEC-BCS Crossover

Phys. Rev. Lett. 99, 150403 (2007)

M. J. Wright,[1] S. Riedl,[1,2] A. Altmeyer,[1,2] C. Kohstall,[1]
E. R. Sánchez Guajardo*,[1] J. Hecker Denschlag,[1] and R. Grimm[1,2]

[1] *Institut für Experimentalphysik und Zentrum für Quantenphysik, Universität Innsbruck, 6020 Innsbruck, Austria*
[2] *Institut für Quantenoptik und Quanteninformation, Österreichische Akademie der Wissenschaften, 6020 Innsbruck, Austria*

We report on experimental studies on the collective behavior of a strongly interacting Fermi gas with tunable interactions and variable temperature. A scissors mode excitation in an elliptical trap is used to characterize the dynamics of the quantum gas in terms of hydrodynamic or near-collisionless behavior. We obtain a crossover phase diagram for collisional properties, showing a large region where a non-superfluid strongly interacting gas shows hydrodynamic behavior. In a narrow interaction regime on the BCS side of the crossover, we find a novel temperature-dependent damping peak, suggesting a relation to the superfluid phase transition.

Ultracold Fermi gases with tunable interactions have opened up intriguing possibilities to study the crossover from bosonic to fermionic behavior in strongly interacting many-body quantum systems [Ing08]. In the zero-temperature limit, a Bose-Einstein condensate (BEC) of molecules is smoothly connected with a superfluid of paired fermions in the Bardeen-Cooper-Schrieffer (BCS) regime. In recent years, great progress has been achieved in the theoretical description of the ground state at zero temperature, and fundamental properties have been experimentally tested with considerable accuracy [Gio08]. Finite-temperature phenomena in the BEC-BCS crossover, however, pose great challenges for their theoretical description. Experimental observations of finite-temperature behavior in the crossover have focussed on the measurement of condensate fractions [Reg04b, Zwi04], on the spectroscopic investigation of pairing phenomena [Chi04a], or on the special case of unitarity-limited interactions [Kin05a, Ste06, Cla07].

To understand the collective dynamics of an ultracold quantum gas, it is crucial to study the conditions for hydrodynamic behavior. Collective mode experiments have probed the dynamics of strongly interacting Fermi gases for variable interaction strength near zero temperature [Bar04a, Kin04b, Alt07a, Alt07b]. The results show the existence of both a hydrodynamic regime of collective

*The contribution of the author of this thesis to this work is to the interpretation of results and to the discussion during the writing of the publication

motion and a near-collisionless regime with independent motion of the trapped particles. The role of temperature, however, remained essentially unexplored.

In this Letter, we explore the collective behavior of a finite-temperature, strongly interacting Fermi gas of ^{6}Li atoms throughout the BEC-BCS crossover. In order to characterize the transition from hydrodynamic to collisionless behavior, we analyze scissors mode oscillations at different temperatures. With varying temperature, the oscillations show a smooth transition between the two collisional regimes along with a broad maximum in the damping rate. We discover an unexpected second peak in the damping rate at lower temperatures in a narrow region on the BCS side of the crossover, where the gas remains hydrodynamic. This suggests the lower-temperature damping peak to be connected to the transition from a superfluid to a normal hydrodynamic gas.

The scissors mode in ultracold quantum gas experiments [GO99a, Mar00] is an angular oscillation of the cloud about a principle axis of an elliptical trap, see Fig. 2.1(a). In our experiments, we confine the atoms in a harmonic, triaxial optical dipole trap. We choose the geometry of the trap to produce an elliptically shaped gas in the x-y plane with very weak confinement along the z axis. The scissors mode experiments are done in the x-y plane. In terms of trap frequencies, the standard configuration is $\omega_x > \omega_y \gg \omega_z$, where these trap frequencies are defined along the principle axes of the trap. If the gas is hydrodynamic, the angle of the gas oscillates collectively with a single frequency of $(\omega_x^2 + \omega_y^2)^{1/2}$. If the gas is collisionless, the trapped atoms oscillate independently, resulting in a two-frequency oscillation. The larger frequency is given by $\omega_x + \omega_y$. When the collisional regime is changed this frequency is adiabatically connected to the hydrodynamic frequency. The smaller frequency is given by $\omega_x - \omega_y$ and is absent in the hydrodynamic limit [GO99a].

The preparation of a strongly interacting Fermi gas of ^{6}Li proceeds in the same way as described in our previous work [Joc03a, Alt07b]. The result is a deeply degenerate, balanced two-component spin mixture of typically $N = 4\times10^5$ atoms with tunable s-wave interactions near a broad Feshbach resonance, which is centered at a magnetic field $B = 834\,\mathrm{G}$. Rapid spatial modulation of the trapping beam by two acousto-optical deflectors is used to create a time-averaged elliptical trapping potential for the scissors mode [Alt07b]. The aspect ratio is set to $\omega_x/\omega_y \approx 2.0$. We employ a trap with frequencies $\omega_x = 2\pi\times830$ Hz and $\omega_y = 2\pi\times415$ Hz ($\omega_z = 2\pi\times22$ Hz), if not indicated otherwise. This results in a Fermi temperature $T_F = (\hbar\bar{\omega}/k_B)\,(3N)^{1/3} = 0.94\mu$K, where $\bar{\omega} = (\omega_x\omega_y\omega_z)^{1/3}$. The trap depth corresponds to about $12\,T_F$. To excite the scissors mode, we suddenly rotate the angle of the trap by ~ 5 degrees, see Fig. 1(a).

The angle of the oscillating cloud is determined by processing absorption images, taken after a short expansion time of $400\,\mu$s. A two-dimensional Thomas-Fermi profile is fit to the images, where the tilt of the principle axes of the cloud is a free parameter, see Fig. 2.1(a). Note that the short expansion somewhat decreases the ellipticity of the cloud, but increases the amplitude of the scissors mode oscillation [Mod03b]. In the hydrodynamic regime, we fit a damped cosine function to the experimental data. In the collisionless regime, we fit the oscillation to a sum of two damped cosine functions each with their own free parameters. In the region between these two limits, we find that a single damped cosine function fits the data reasonably well, as the lower-frequency component damps out very quickly [GO99a].

First, we examine the collective behavior of the gas at our lowest obtainable temperatures. We compare scissors mode oscillations at different settings of the magnetic field, i.e. different values of $1/k_Fa$. Typical scissors mode oscillations are shown in Fig. 2.1(b). At $B = 661$ G, far on the BEC side of resonance, the gas exhibits nearly collisionless behavior. Here inelastic collisions result in heating the gas above the critical temperature for BEC. In the regime where the gas is

strongly interacting, $B = 750$ G, 834 G, and 900 G, the gas oscillates collectively. High precision measurements taken at $B = 834$ G show the scissors mode oscillation yields a frequency that agrees with theory within one percent. Far on the BCS side, at $B = 970$ G and 1132 G, the gas exhibits behavior that is nearly collisionless. The abrupt transition between the hydrodynamic and collisionless regimes at low temperature occurs at essentially the same magnetic field, $B \approx 950$ G, as in other collective mode experiments [Bar04a, Kin04b, Alt07b].

To explore finite-temperature collisional behavior, we extend the scissors mode measurements. To set the temperature, we use a controlled heating scheme. Here, we suddenly compress the trap and allow for subsequent equilibration [1]. We control the temperature of the gas by adjusting the amount of compression.

The determination of the temperature T in an ultracold, strongly interacting Fermi gas is in general difficult [Kin05b]. We can measure an effective temperature (or entropy) parameter $\tilde{T}$ at the center of the Feshbach resonance, $B = 834$ G. We determine $\tilde{T}$ by fitting integrated, one-dimensional, density profiles in the manner described in [Kin05b, Kin06, Sta05]. At $B = 834$ G, for $T/T_F > 0.3$, the parameter $\tilde{T}$ is proportional to the real temperature with $T/T_F \approx \tilde{T}/1.5$. For lower temperatures, an empirical conversion has been determined [2][Kin05b, Kin06, Sta05]. The parameter $\tilde{T}$, measured in the unitarity limit at 834 G, can be used also as a temperature scale for other interaction regimes under the condition that entropy is conserved in adiabatic sweeps of the magnetic field [Che05].

In Figure 2.2, we show the frequency and damping rate as a function of $\tilde{T}$ for two cases, in the unitarity limit ($1/k_F a = 0.00$) and at the BCS side of the crossover ($1/k_F a = -0.45$). The frequency behavior in Fig. 2.2(a) is qualitatively the same for both cases. At low temperatures, the gas shows the hydrodynamic frequency and, at the highest temperatures, we observe the behavior characteristic for the collisionless gas. With varying temperature, the changing frequency smoothly connects the hydrodynamic with the collisionless regime. Quantitatively, the transition occurs at somewhat higher $\tilde{T}$ in the unitarity limit. In the transition region, the damping rate shows a maximum that accompanies the change in frequency, see Fig. 2.2(b). We introduce the temperature parameter $\tilde{T}_H$ for this damping maximum, marking the transition between hydrodynamic and collisionless behavior.

The temperature dependence of the damping rate in Fig. 2.2(b) reveals a qualitatively different behavior between the two interaction regimes. An additional peak shows up at lower temperatures for the BCS side of the crossover, while this peak is absent in the unitarity limit. Remarkably, this novel feature is not associated with a change in the frequency.

We could detect the low-temperature damping peak only in a very narrow range at the BCS side of the crossover. This feature was found between magnetic fields of 890 G and 920 G, corresponding to interaction parameters $1/k_F a$ between -0.6 and -0.4. In Fig. 2.3, we show the low-temperature damping peak as it changes in this narrow region. Closer to resonance, the peak becomes very narrow, shifts toward higher temperatures, and finally seems to disappear. To mark the location of this peak, we introduce the temperature parameter $\tilde{T}_S$.

We now discuss our observations in terms of a crossover phase diagram for the scissors mode

[1] Sudden compression of the trap excites the axial mode which is long lived. Since the frequency is much smaller than the scissors mode frequency, it can be neglected. Nonetheless, we carried out a direct comparison without the axial mode present and found the same behavior.

[2] $\tilde{T} \approx 1.2(T/T_F)^{1.49}$ for $(T/T_F) < 0.3$.

excitation [3]. In Fig. 2.4(a), we plot $\tilde{T}_H$ (closed circles) and $\tilde{T}_S$ (open squares) as a function of the interaction parameter. The data points for $\tilde{T}_H$ show a pronounced maximum at the center of the resonance. To facilitate an interpretation of the experimental data, we convert $\tilde{T}_H$ and $\tilde{T}_S$ into real temperatures T_H and T_S, following the theory of Ref. [Che05]. Fig. 2.4(b) shows the resulting phase diagram, including a theoretical prediction [Per04] of the temperature T_C for the phase transition to a superfluid state.

Near the center of the Feshbach resonance, hydrodynamic behavior is observed far above the superfluid transition temperature. The large difference between T_H and T_C confirms the existence of a non-superfluid hydrodynamic region above T_C [Min01, Kin05a, Cla07]. Our measurements show that this normal-gas hydrodynamic regime is restricted to the narrow, strongly interacting region near resonance where $1/k_F a$ stays well below unity. On the BEC side, T_H is close to the expected value for T_C. Here one can assume that hydrodynamic behavior essentially results from the formation of a molecular BEC. A surrounding non-condensed molecular gas would exhibit near-collisionless properties, similar to what has been measured in atomic BEC experiments [Mar01]. On the BCS side of resonance, T_H falls off very rapidly. In this region, collective modes may couple to the weakly bound fermion pairs [Bar04a, Alt07b]. We did not observe hydrodynamic behavior beyond that point.

For the low-temperature damping peak found at the BCS side of the crossover near $1/k_F a \approx -0.5$, our phase diagram in Fig. 2.4(b) suggests a close relation to the superfluid phase transition. The peak occurs at roughly $0.6\,T_C$, and it follows the general behavior of the superfluid transition to move toward higher temperature as it approaches the resonance. This points to a scenario where a substantial superfluid core in the center of the trap is surrounded by a non-superfluid, but still hydrodynamic fraction in the outer region of the trap. Whether damping results from the coupling of these two components or whether other mechanisms are responsible for this phenomenon remains an open question. We note that the low-temperature damping peak is not specific to the scissors mode. We have also found a corresponding, but less pronounced peak in measurements of the radial breathing mode. Further investigations and better theoretical understanding will be required to answer the intriguing question whether the novel damping peak does indeed mark the transition from the normal hydrodynamic to the superfluid state.

In conclusion, we have investigated hydrodynamic behavior at finite temperatures in the BEC-BCS crossover using scissors mode excitations. Our measurements highlight the existence of a region of non-superfluid hydrodynamics in the strongly interacting regime where $|k_F a| \gtrsim 1$. In the unitarity limit, predominant hydrodynamic behavior is found up to $\sim 0.6\,T_F$, which substantially exceeds the superfluid transition temperature of $\sim 0.3\,T_F$. With increasing temperature, the transition from hydrodynamic to collisionless behavior proceeds in general smoothly and is accompanied by a local maximum of damping. In addition, we have discovered a novel low-temperature damping peak at the BCS side of the crossover, which suggests a relation to the superfluid phase transition. With this observation, experiments on collective oscillation modes of Fermi gases in the BEC-BCS crossover continue to produce puzzling observations [Bar04a, Kin05a, Alt07b] with the potential to stimulate deeper theoretical understanding of the physics of strongly interacting Fermi gases.

We thank S. Stringari for stimulating discussions. We also thank Q. Chen, K. Levin, and J. E.

[3] In a comparative study of different collective modes [Rie08] we found the scissors mode to behave very similar to the radial quadrupole mode [Alt07b], which is also a surface mode. The radial compression mode behaves quite differently [Kin05a, Rie08]. The axial mode [Bar04a] shows in general hydrodynamic behavior in a much wider parameter range because of its much lower frequency.

Thomas for discussions concerning determination of the temperature. We acknowledge support by the Austrian Science Fund (FWF) within SFB 15 (project part 21). M.J.W. is supported by a Marie Curie Incoming International Fellowship within the 6th European Community Framework Program.

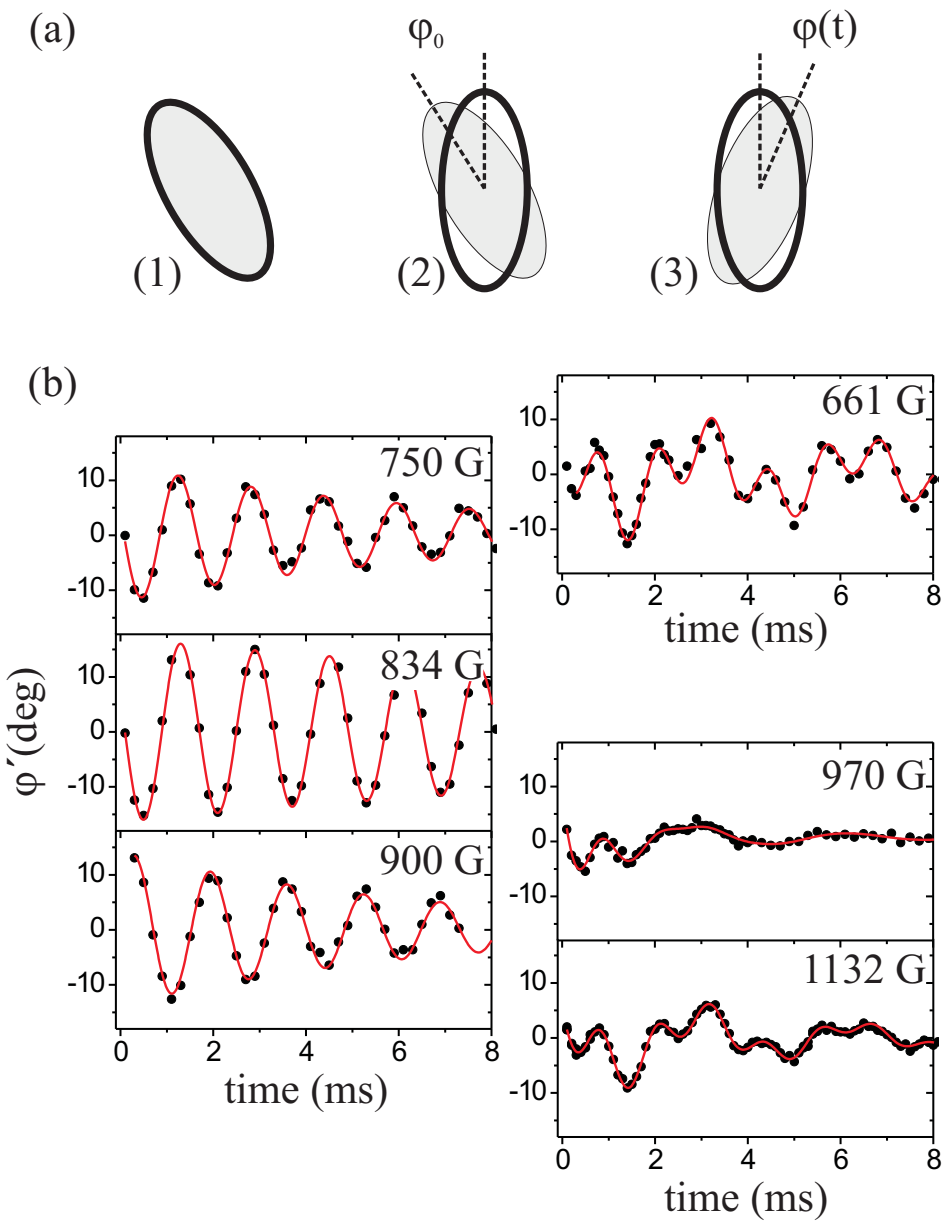

Figure 2.1.: (a) Schematic showing the excitation of the scissors mode. (1) The gas (shaded region) is at rest, in equilibrium with the trap (heavy solid line). (2) The trap is suddenly rotated. (3) The gas oscillates around the new equilibrium position. (b) Scissors mode oscillations observed at the lowest obtainable temperature ($T \approx 0.1T_F$ at 834 G) for various magnetic fields. On the left side, where $B = 750$ G, 834 G, and 900 G ($1/k_F a = 1.4$, 0.0, and -0.6), the gas is hydrodynamic. On the right side, where $B = 661$ G, 970 G, and 1132 G ($1/k_F a = 5.0$, -1.0, and -1.44), the gas is nearly collisionless and exhibits the characteristic two-frequency oscillation. Here $\omega_x = 2\pi \times 580\,\mathrm{Hz}$, $\omega_y = 2\pi \times 270\,\mathrm{Hz}$, and $T_F = 0.69\,\mu\mathrm{K}$.

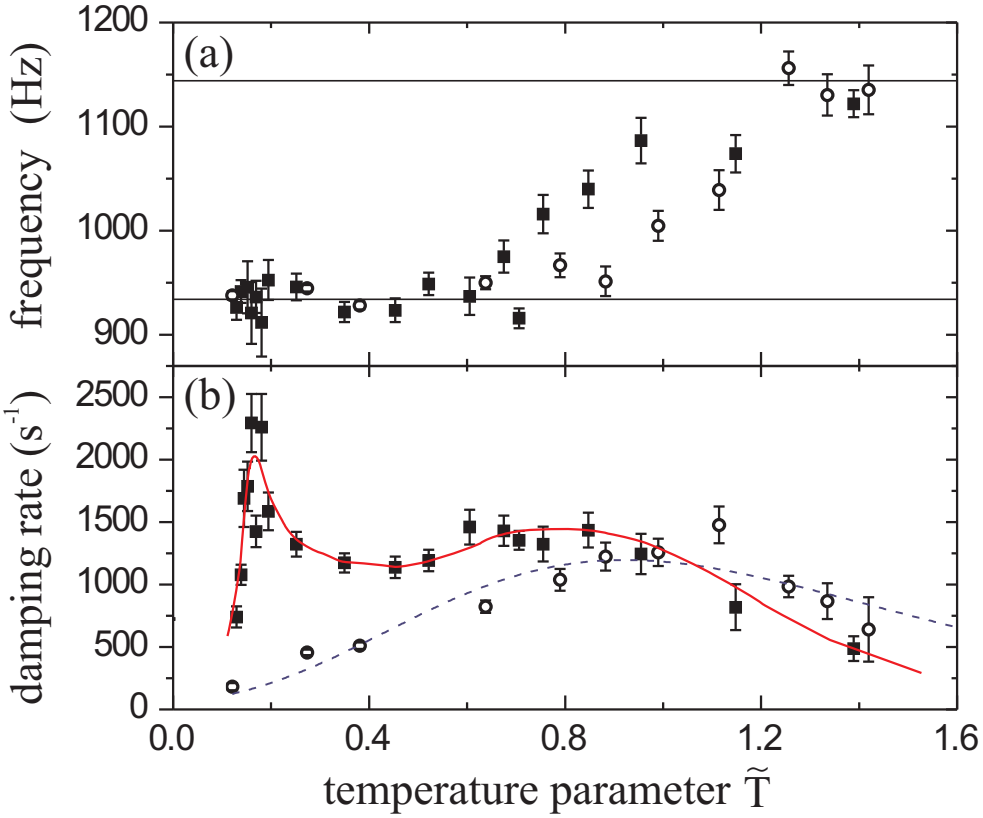

Figure 2.2.: Frequency and damping rate for the scissors mode oscillation for $B = 895$ G ($1/k_F a = -0.45$, solid squares) and at $B = 834$ G ($1/k_F a = 0$, open circles). The frequency limits in the hydrodynamic and collisionless regimes are shown by the horizontal lines in (a), including small corrections for the anharmonicity of the trap [Rie08]. The lines in (b) are introduced as guides to the eye. For $\tilde{T}$ greater than 1.14, the scissors mode oscillations are fit by a two-frequency cosine function (for details see text).

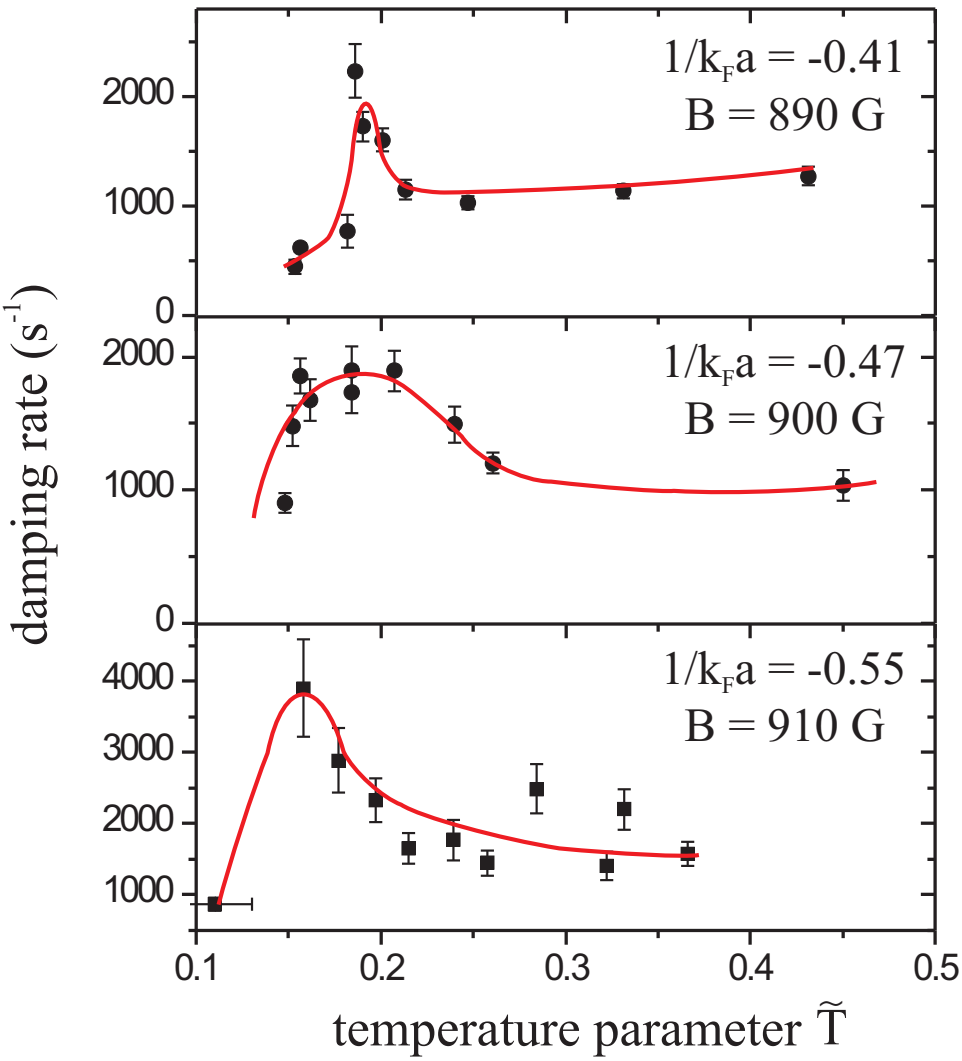

Figure 2.3.: Low-temperature damping peak observed in a narrow magnetic-field region at the BCS side of the resonance ($1/k_F a \approx -0.5$). The solid lines are introduced as guides to the eye.

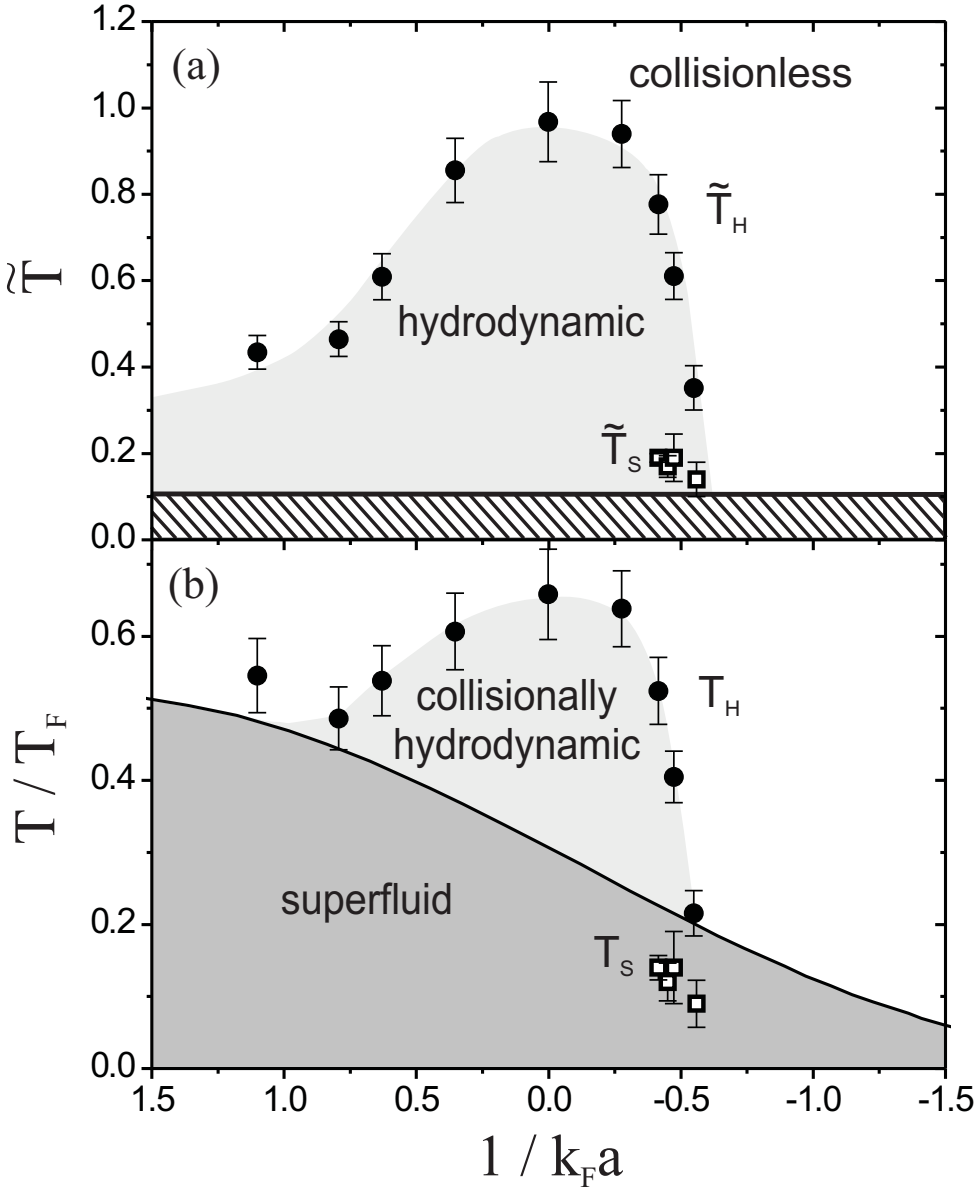

Figure 2.4.: Phase diagram for the hydrodynamic behavior of the scissors mode in terms of (a) the temperature parameter $\tilde{T}$ and (b) the real temperature T. The smooth transition from hydrodynamic to collisionless is characterized by the temperature parameter $\tilde{T}_H$ (temperature T_H). The second damping peak near $1/k_F a \approx -0.5$ is marked by $\tilde{T}_S$ (T_S). In (a) the hatched region indicates the region ($\tilde{T} < 0.1$) where our thermometry does not produce reliable results. In (b) the solid line shows a theoretical curve for the phase transition to superfluidity [Per04].

3. Collective oscillations of a Fermi gas in the unitarity limit: Temperature effects and the role of pair correlations

Phys. Rev. A 78, 053609 (2008)

S. Riedl,[1,2] E. R. Sánchez Guajardo*,[1] C. Kohstall,[1] A. Altmeyer,[1,2]
M. J. Wright,[1] J. Hecker Denschlag,[1] and R. Grimm[1,2]

[1] *Institut für Experimentalphysik und Zentrum für Quantenphysik, Universität Innsbruck, 6020 Innsbruck, Austria*
[2] *Institut für Quantenoptik und Quanteninformation, Österreichische Akademie der Wissenschaften, 6020 Innsbruck, Austria*

G. M. Bruun[3,4] and H. Smith[4]

[3] *Dipartimento di Fisica, Università di Trento and CNR-INFM BEC Center, I-38050 Povo, Trento, Italy*
[4] *Niels Bohr Institute, University of Copenhagen, DK-2100 Copenhagen Ø, Denmark*

We present detailed measurements of the frequency and damping of three different collective modes in an ultracold trapped Fermi gas of ^{6}Li atoms with resonantly tuned interactions. The measurements are carried out over a wide range of temperatures. We focus on the unitarity limit, where the scattering length is much greater than all other relevant length scales. The results are compared to theoretical calculations that take into account Pauli blocking and pair correlations in the normal state above the critical temperature for superfluidity. We show that these two effects nearly compensate each other and the behavior of the gas is close to that of a classical gas.

3.1. Introduction

The study of collective oscillations in quantum liquids and gases has yielded a wealth of insights into the properties of strongly correlated systems. An early example concerning strongly correlated Fermions is the observed transition from ordinary first sound to zero sound in the normal state of liquid ^{3}He as the temperature is lowered [Abe66]. In this Article we explore related phenomena in an ultracold quantum gas of fermions in the unitarity limit [Ing08] by measuring three different collective modes under similar conditions. The frequency and damping of the modes exhibit the

*The contribution of the author of this thesis to this work is to the interpretation of results and to the discussion during the writing of the publication. G.M. Bruun and H. Smith provided us with the theoretical curves, and provided the theoretical section.

characteristic transition from hydrodynamic behavior at low temperature to collisionless behavior at higher temperature. The experimental observations are compared to theoretical model calculations that apply to the normal state of the gas above the critical temperature T_c for superfluidity. In the unitarity limit, the strongly correlated normal state between T_c and the Fermi temperature T_F is arguably not as well understood as the $T = 0$ superfluid phase [Gio08]. It is shown that the combined effects of temperature and pair correlations account for most of the observed features in this interesting temperature regime.

Our measurements of the collective modes are carried out for an elongated trap geometry, which has previously been shown to be well suited for studying the dynamical behavior of a strongly interacting Fermi gas [Bar04a, Kin04a, Kin04b, Kin05a, Alt07a, Alt07b, Wri07]. We focus on two collective excitations of a cylindrically symmetric cigar-shaped cloud, namely the radial compression mode and the radial quadrupole mode. In addition we study the scissors mode under conditions where the cloud exhibits pronounced ellipticity in the plane perpendicular to the direction of the cigar-shaped cloud. In all three modes, the cloud oscillates mainly in the plane normal to the direction of the cigar-shaped cloud. For a sketch of the modes see Figure 3.1.

Previous experiments on collective modes in a strongly interacting Fermi gas studied the effect of the interaction strength in the zero temperature limit. [Bar04a, Kin04a, Kin04b, Alt07a, Alt07b]. Systematic investigations were performed studying the radial compression mode [Bar04a, Kin04a, Alt07a] and the radial quadrupole mode [Alt07b]. Measurements on the compression mode served as a sensitive probe for the equation of state of the gas in the zero temperature limit throughout the BEC-BCS crossover regime. In contrast to the compression mode, the frequency of the radial quadrupole mode allows one to test the hydrodynamic behavior without being influenced by the equation of state. This made it possible to investigate the transition from hydrodynamic to collisionless behavior with decreasing coupling strength of the atom pairs on the BCS side of the crossover.

While the hydrodynamic behavior in the zero-temperature limit is now well understood as a result of superfluidity, an understanding of the effects of temperature on the collective modes has remained a challenge. Only few experiments have so far addressed this problem [Alt07a, Kin05a, Wri07, Kin04a]. Previously, the temperature dependence of the radial compression mode [Kin05a] and the scissors mode was studied [Wri07]. Our present experiments aim at addressing the open questions raised by the different results obtained in these experiments: The frequency and damping of the radial compression mode was studied as function of the temperature in an experiment performed at Duke University [Kin05a]. There the mode frequency appeared to stay close to the hydrodynamic value even for temperatures exceeding the Fermi temperature. This surprising finding stands in contrast to scissors mode measurements, performed later at Innsbruck University [Wri07], which clearly showed a transition to collisionless behavior in the same temperature range. Furthermore the Duke data on the damping of the compression mode did not show a maximum as it was seen in the Innsbruck data on the scissors mode measurement. These apparent discrepancies are a particular motivation for our present study of different collective modes under similar experimental conditions.

3.2. Experimental Procedure

The apparatus and the basic preparation methods for experiments with a strongly interacting Fermi gas of ^{6}Li atoms have been described in our previous work [Joc03a, Bar04b]. As a starting point,

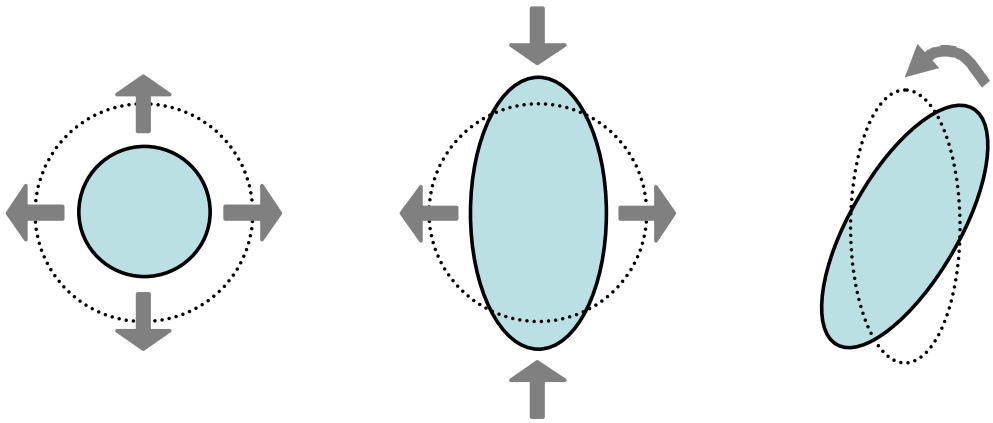

Figure 3.1.: Sketch of the three collective modes investigated in this work: the compression mode, the quadrupole mode and the scissors mode (from left to right). The oscillations take place in the plane of tight confinement, perpendicular to the direction of the elongated, cigar-shaped cloud. While the compression mode represents an oscillation of the overall cloud volume, the other two modes only involve surface deformations. Exciting the quadrupole mode leads to an oscillating elliptic shape. The scissors mode appears as an angular oscillation of an elliptic cloud about a principal axis of an elliptic trap geometry.

we produce a molecular BEC of $^6Li_2$. By changing an external magnetic field, we can control the interparticle interactions in the vicinity of a Feshbach resonance, which is centered at 834 G [Bar05]. The measurements of the collective modes are performed at the center of the Feshbach resonance, where the interactions are unitarity limited.

The atoms are confined in an elongated, nearly harmonic trapping potential, where the trap frequencies ω_x and ω_y in the transverse direction are much larger then the axial trap frequency ω_z. The confinement in the transverse direction is created by an optical dipole trap using a focused 1030 nm laser beam with a waist of 47 μm. Note that the Gaussian shape of the laser beam leads to significant anharmonicities in the trapping potential. The potential in the axial direction consists of a combination of optical and magnetic confinement; the magnetic confinement is dominant under the conditions of the present experiments. The trap parameters, given in Table 3.1, represent a compromise between trap stability and anharmonic effects [1]. The Fermi temperature is given by $T_F = E_F/k$, where the Fermi energy $E_F = \hbar(3N\omega_x\omega_y\omega_z)^{1/3} = \hbar^2 k_F^2/2m$, k_F is the Fermi wavenumber and k is the Boltzmann constant. The parameter V_0 is the trap depth, and N is the total number of atoms, given by $N = 6 \times 10^5$. The interactions are characterized by the dimensionless parameter $1/k_F a$, where a is the s-wave scattering length.

To control the aspect ratio ω_x/ω_y, we use rapid spatial modulation of the trapping beam by two acousto-optical deflectors, resulting in the creation of time-averaged trapping potentials [Alt07b].

[1] Anharmonic effects depend on the ratio between the Fermi energy and trap depth E_F/V_0 [Str]. Reducing this ratio decreases the anharmonic effects. This can be done by increasing the power of the trapping beam since E_F increases more slowly than V_0. On the other hand technical reasons cause heating rates and larger drifts in the trap depth with increasing power.

Table 3.1.: Trap parameters for the differentmodes.

	compression	quadrupole	scissors
$\omega_x/2\pi$ (Hz)	1100	1800	1600
$\omega_y/2\pi$ (Hz)	1100	1800	700
$\omega_z/2\pi$ (Hz)	26	32	30
T_F (μK)	1.8	2.7	1.9
V_0/k (μK)	19	50	40

This on one hand allows us to compensate for residual ellipticity of the trapping potential on the percent level and thus to realize a cylindrical symmetric trap ($\omega_x = \omega_y$). On the other hand it allows for the excitation of surface modes by deliberately introducing elliptic trapping potentials ($\omega_x \neq \omega_y$). The procedures used to excite the modes are outlined in Appendix A. To change the temperature we apply a controlled heating scheme via sudden compression of the gas as described in [Wri07]. Detection of the cloud is done by absorption imaging which displays the shape of the cloud in the x-y plane after expansion. For each mode under investigation we determine the frequency and damping following the procedures of our previous work [Alt07b, Wri07, Alt07a]; see also Appendix A.

Because of the Gaussian shape of the trapping potential, corrections are needed for a precise comparison of the experimental observation to the idealized case of perfect harmonic trapping. Especially for higher temperatures, when the size of the cloud is larger, anharmonic corrections become important. This is demonstrated by measurements of the transverse sloshing mode frequency ω_s (Fig. 3.2), which clearly show a substantial decrease with increasing temperature. To reduce the anharmonic effects on the frequencies of the collective modes under investigation, we normalize the frequencies to the sloshing mode frequency in the transverse direction. This normalization reduces the anharmonic effects to a large extent since the decrease of the sloshing mode frequency with increasing cloud size is of the same order as the corresponding decrease of the frequency of the transverse modes [Str]. To normalize the scissors mode frequency we take the geometric average of the two different sloshing mode frequencies in the transverse direction.

For each of the trap parameters of the different modes we determine the sloshing mode frequency as a function of the temperature. As an example we show ω_s for the trap parameters used for the compression mode measurement; see Fig. 3.2. We compare ω_s/ω_x (dots) to a theoretical model which allows to calculate the sloshing frequency as a function of the cloud size; see Appendix B. Assuming a harmonic potential to derive the mean squared size $\langle x^2 \rangle$ [2] Our calculation of $\langle x^2 \rangle$ is based on density profiles derived by Q. Chen, J. Stajic, and K. Levin, Phys. Rev. Lett. **95**, 260405 (2005) underestimates the anharmonic effects (solid line) in particular for higher temperatures. Taking into account a Gaussian potential to determine $\langle x^2 \rangle$ (dashed line) agrees much better with the measured sloshing frequency.

Since the purpose of this article is the comparative study of different collective modes and not the precision measurement of a single mode as in previous work [Alt07a], we follow a faster yet simpler procedure to normalize the frequencies. We measure the sloshing mode frequency only on particular temperatures of interest. From these points we determine the temperature dependence of the sloshing frequency by interpolation. Even though the normalization takes into account the temperature dependence of the anharmonicity, it does not reduce effects due to drifts in the power

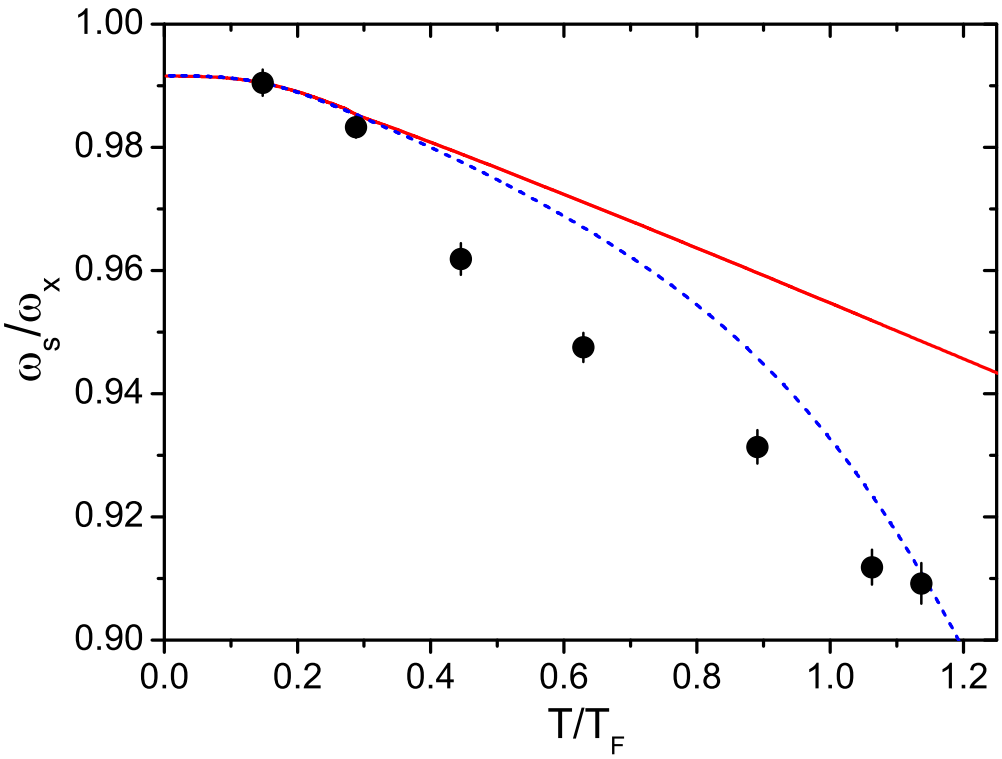

Figure 3.2.: Sloshing mode frequency ω_s normalized by the trap frequency ω_x as a function of temperature. The measured frequency shows a decrease with increasing temperature, (dots) which is due to the increase in the size of the cloud. The lines show the expected frequency from a first-order anharmonic correction; see Appendix B. To determine the cloud size for different temperatures we assume a harmonic potential (solid line) and a Gaussian potential (dashed line), respectively [2]

of the trapping beam. We believe this to be the main source for the scatter of the data in Fig. 3.4.

To determine the temperature of the gas we first adiabatically change the magnetic field to 1132 G [3], where $1/k_F a \approx -1$, to reduce the effect of interactions on the density distribution [Luo07]. Under this condition, for $T > 0.2T_F$, the interaction effect on the density distribution is sufficiently weak to treat the gas as a non-interacting one to determine the temperature from time-of-flight images. We fit the density distribution after 2 ms release from the trap to a finite-temperature Thomas–Fermi profile. The temperature measured at 1132 G is converted to the temperature in the unitarity regime under the assumption that the conversion takes place isentropically, following the approach of Ref. [Che05]. Statistical uncertainties for the temperature stay well below $0.05T_F$.

[3] This is the largest magnetic field for which we can take absorption images in our present set-up.

3.3. Theory

We shall compare our experimental findings to the results of model calculations that apply to the normal state of the gas, i.e. at temperatures above T_c. In this Section, we outline our theoretical approach to the calculation of mode frequencies for $T > T_c$. A more detailed description can be found in Refs. [Mas05] and [Bru05]. We assume that single-particle excitations are reasonably well defined in the sense that most of the spectral weight of the single-particle spectral function is located at a peak corresponding to that of non-interacting particles. The low-energy dynamics of the gas can then be described by a semiclassical distribution function $f(\mathbf{r}, \mathbf{p}, t)$ which satisfies the Boltzmann equation. A collective mode corresponds to a deviation $\delta f = f - f^0$ away from the equilibrium distribution $f^0(\mathbf{r}, \mathbf{p})$. Writing $\delta f(\mathbf{r}, \mathbf{p}, t) = f^0(\mathbf{r}, \mathbf{p})[1-f^0(\mathbf{r}, \mathbf{p})]\Phi(\mathbf{r}, \mathbf{p}, t)$ and linearizing the Boltzmann equation in $\delta f(\mathbf{r}, \mathbf{p}, t)$ yields

$$f^0(1 - f^0)\left(\frac{\partial \Phi}{\partial t} + \dot{\mathbf{r}} \cdot \frac{\partial \Phi}{\partial \mathbf{r}} + \dot{\mathbf{p}} \cdot \frac{\partial \Phi}{\partial \mathbf{p}}\right) = -I[\Phi], \tag{3.1}$$

where $\dot{\mathbf{r}} = \mathbf{v} = \mathbf{p}/m$, $\dot{\mathbf{p}} = -\partial V/\partial \mathbf{r}$ and I is the collision integral. We take the potential $V(\mathbf{r})$ to be harmonic and given by $V(\mathbf{r}) = m(\omega_x^2 x^2 + \omega_y^2 y^2 + \omega_z^2 z^2)/2$.

To describe the collective modes we expand the deviation function in a set of basis functions ϕ_i according to

$$\Phi(\mathbf{r}, \mathbf{p}, t) = e^{-i\omega t} \sum_i c_i \phi_i(\mathbf{r}, \mathbf{p}), \tag{3.2}$$

where ω is the mode frequency. For the compression mode with a velocity field $\mathbf{v} \propto (x, y, z)$, we use the functions

$$\phi_1 = x^2 + y^2,\ \phi_2 = xp_x + yp_y,\ \phi_3 = p_x^2 + p_y^2,\ \phi_4 = p_z^2. \tag{3.3}$$

For the quadrupole mode with a velocity field $\mathbf{v} \propto (y, x, 0)$ (ignoring the small velocity along the axial direction), we use

$$\phi_1 = x^2 - y^2,\ \phi_2 = xp_x - yp_y,\ \phi_3 = p_x^2 - p_y^2, \tag{3.4}$$

whereas the basis functions for the scissors mode are given in Ref. [Bru07]. Our choice of basis functions is physically motivated by the characteristic features of the three different modes illustrated in Fig. 3.1. Since we limit ourselves to a few simple functions, the basis sets are not complete, but we do not expect qualitative changes to occur as a result of including more basis functions in our calculation.

We now insert the expansion (3.2) into (3.1) and take moments by multiplying with the functions ϕ_i and integrating over both $\mathbf{r}$ and $\mathbf{p}$. This yields a set of linear equations for the coefficients c_i for each of the collective modes. The corresponding determinants give the mode frequencies. For the compression mode, we obtain

$$i\omega(\omega^2 - 4\omega_\perp^2) + \frac{1}{\tau}\left(\frac{10}{3}\omega_\perp^2 - \omega^2\right) = 0, \tag{3.5}$$

and for the quadrupole mode, we get

$$i\omega(\omega^2 - 4\omega_\perp^2) + \frac{1}{\tau}\left(2\omega_\perp^2 - \omega^2\right) = 0. \tag{3.6}$$

The equation for the scissors mode is given in Ref. [Bru07].

The effective collision rate $1/\tau$ in (3.5) and (3.6) is given by

$$\frac{1}{\tau} = \frac{\int d^3r d^3p p_x p_y I[p_x p_y]}{\int d^3r d^3p p_x^2 p_y^2 f^0(1-f^0)}. \tag{3.7}$$

Note that this expression for $1/\tau$ involves a spatial average over the cloud. In the collisionless limit, $\omega\tau \gg 1$, the two equations (3.5) and (3.6) both yield $\omega = 2\omega_\perp$, where $\omega_\perp = \omega_x = \omega_y$, while in the hydrodynamic limit, $\omega\tau \ll 1$, they result in $\omega = \sqrt{10/3}\omega_\perp$ for the compression mode and $\omega = \sqrt{2}\omega_\perp$ for the quadrupole mode.

The dependence on temperature T and scattering length a enters through τ. In particular, Pauli blocking and pair correlations strongly depend on T and a, and we now examine their role on the effective collision rate. In Fig. 3.3, we plot $1/\tau$ as a function of temperature for a gas in the unitarity limit $|a| \to \infty$ using three different approximations for the collision integral. First, the

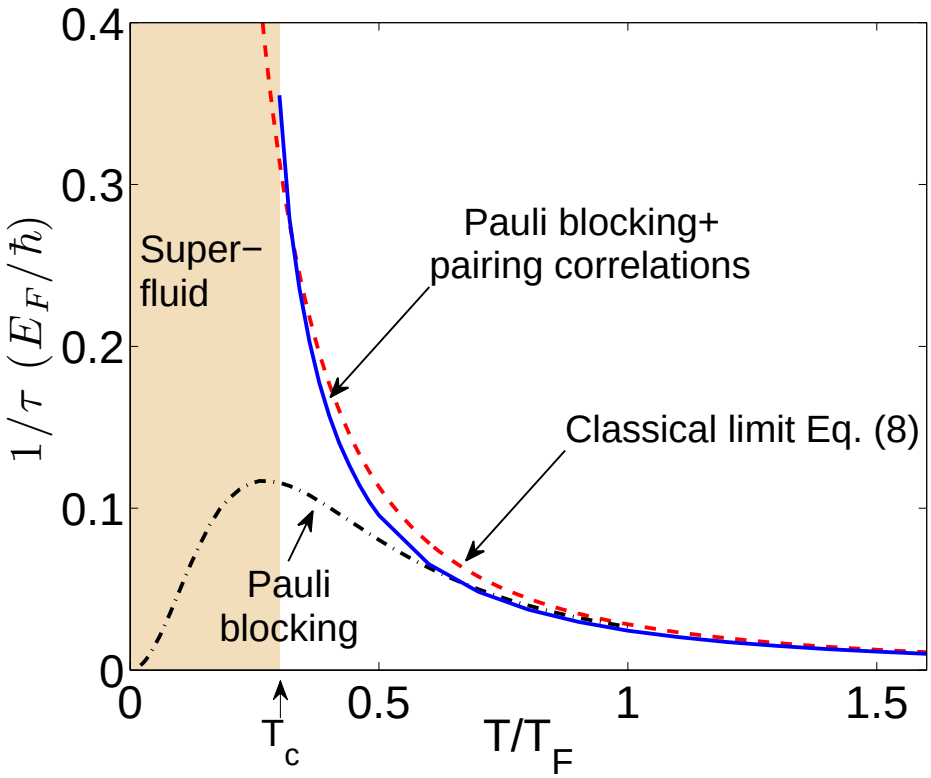

Figure 3.3.: (Color online) The effective collision rate for a gas in the unitarity limit. The dashed curve is the classical result, the dash-dotted includes Pauli blocking, and the solid line includes pairing correlations in the scattering matrix. The superfluid region for $T < T_c$ is indicated.

dashed curve gives the effective collision rate in the classical regime using the vacuum expression $\mathcal{T}_{\text{vac}} = \mathcal{T}_0/(1+iqa)$ for the scattering matrix with $\mathcal{T}_0 = 4\pi\hbar^2 a/m$. The s-wave differential cross

section $d\sigma/d\Omega$ which enters in the collision integral I is related to the scattering $\mathcal{T}$ matrix by $d\sigma/d\Omega = m^2|\mathcal{T}|^2/(4\pi\hbar^2)^2$. In the classical regime, we then get from (3.7)

$$\frac{1}{\tau_{\text{class}}} = \frac{4}{45\pi}\frac{kT_F}{\hbar}\frac{T_F^2}{T^2} \tag{3.8}$$

for a gas in the unitarity limit [Bru07]. The small prefactor $4/(45\pi) \approx 0.028$ in (3.8) implies that the effective collision rate is significantly smaller than what one would expect from simple estimates or dimensional analysis at unitarity. Second, the dash-dotted curve gives the effective collision rate when Pauli blocking effects are included as in [Mas05], while we still use the vacuum expression $\mathcal{T}_{\text{vac}}$ for the scattering matrix. Pauli blocking effects reduce the available phase space for scattering thereby reducing the scattering rate. For $T \ll T_F$ Pauli blocking in a normal Fermi system gives $1/\tau \propto T^2$. Finally, we plot as a solid curve in Fig. 3.3 the effective collision rate taking into account both Pauli blocking and many-body effects for $\mathcal{T}$ in the ladder approximation which includes the Cooper (pairing) instability. This gives $\mathcal{T} = \mathcal{T}_0/(1 - \mathcal{T}_0\Pi)$ where Π is the pair propagator. Since our treatment of the pair correlations only apply to the normal state of the gas, we plot this curve for temperatures greater than the critical temperature T_c, which within the ladder approximation used here is given by $T_c \approx 0.3T_F$ for a trap [Bru05].

We see that $1/\tau$ is increased by the pairing correlations for the $\mathcal{T}$-matrix. The pairing correlations significantly increase the effective collision rate for temperatures $(T - T_c)/T_c \lesssim 1$ [Bru05]. One often refers to this temperature range as the pseudogap regime. In fact, pairing correlations almost cancel the Pauli blocking effect in the collision integral above T_c and $1/\tau$ is fairly accurately given by the classical value as can be seen from Fig. 3.3. At high temperatures, this cancelation can be demonstrated analytically by carrying out a high-temperature expansion of (3.7). We obtain after some algebra the simple expression

$$\frac{1}{\tau} = \frac{1}{\tau_{\text{class}}}\left[1 + \frac{1}{32}\left(\frac{T_F}{T}\right)^3\right]. \tag{3.9}$$

The presence of the small prefactor 1/32 in (3.9) shows that the leading correction to the classical limit is less than 3% at temperatures above the Fermi temperature T_F.

3.4. Results and Discussion

The theoretical results of the previous section were all obtained for a purely harmonic potential. Since anharmonicity plays an important role in our experiments, as discussed in Sec. 3.2, we normalize the measured frequencies and damping rates for the collective modes to the measured temperature-dependent sloshing frequencies, for which an example is shown in Fig. 3.2. In the following we compare our observations to the theoretical results. It should be emphasized that the theoretical expressions for the frequency and damping contain no free parameters to fit theory and experiment.

First we discuss the frequency for the three modes under investigation as a function of the temperature, as plotted in Fig. 3.4. In all three cases the theoretical expression for the frequency (the full lines in Fig. 3.4) smoothly changes from the hydrodynamic value at the lowest temperature considered to the collisionless value at high temperatures. The normalized frequencies in the hydrodynamic limit for the quadrupole mode and compression mode are $\sqrt{2} \approx 1.41$ and $\sqrt{10/3} \approx$

1.83, respectively. The normalized frequency in the collisionless limit for both these modes is 2. Using the geometric average of the trap frequencies to normalize the scissors mode frequency, one gets, using the ratio $\omega_x/\omega_y = 16/7$ from Table I, that $\sqrt{(\omega_x^2+\omega_y^2)/(\omega_x\omega_y)} \approx 1.64$ in the hydrodynamic limit and $(\omega_x+\omega_y)/\sqrt{\omega_x\omega_y} \approx 2.17$ in the collisionless limit. Note that the scissors mode consists of a two-frequency oscillation in the collisionless limit. Here we only consider the larger frequency component. The lower frequency component exhibits increasing damping towards lower temperatures and disappears in the hydrodynamic limit [GO99a].

Figure 3.4 illustrates that there is a reasonable overall agreement between experiment and theory, although some differences exist. The agreement is best for the scissors mode, while for the quadrupole mode the changeover from hydrodynamic to collisionless behavior happens at a lower temperature than the one found theoretically. The measured compression mode frequency, which shows considerable scatter, increases with increasing temperature and is close to the collisionless value at the highest temperature measured.

The observed change from the hydrodynamic to the collisionless frequency for the compression mode is in contrast to Ref. [Kin05a], where the frequency remains at the hydrodynamic value for the same temperature range. We attribute this discrepancy to different treatments of anharmonic effects, which are particularly important for this mode since the difference between the hydrodynamic and collisionless frequency is of the same order as the frequency shift due to anharmonic effects. In Ref. [Kin05a] the data are corrected by including anharmonic effects to first order, while we adopt the point of view that the main anharmonic effects can be taken into account by normalizing the measured oscillation frequencies to the measured temperature-dependent sloshing frequencies. Fig. 3.2 illustrates that a simple first-order treatment of anharmonic effects on the sloshing frequency does not account quantitatively for the observed variation with temperature.

At very low temperatures the measured frequencies are close to the hydrodynamic values because the gas is in the superfluid phase [Alt07a, Alt07b]. Without pair correlations, but with Pauli blocking, at these low temperatures the frequencies would assume their collisionless values as illustrated by the dashed-dotted lines in Fig. 3.4.

We now proceed to consider the damping of the oscillations. The experimental values for the normalized damping rate are shown in Fig. 3.5. Theoretically, one expects the damping to vanish in the hydrodynamic and collisionless limits and exhibit a maximum in between, as brought out by the calculations in Sec. 3.3. Experimentally, both the quadrupole and the scissors mode exhibit the expected maximum in damping in the transition region. For the compression mode, however, the damping does not decrease at higher temperatures. This surprising behavior for the compression mode has already been found in [Kin05a]. A possible reason for the increasing damping is dephasing-induced damping due to anharmonicity. Anharmonic effects are more important for the compression mode as the intrinsic damping is relatively small due to the small difference between the frequencies in the collisionless and hydrodynamic limits [GO99b]. In contrast to the case of frequency discussed above, we cannot expect to take into account the main effects of anharmonicity by normalizing the measured damping rate to the temperature-dependent sloshing mode frequencies. This makes it delicate to compare our experimental results to those of a theory based on a purely harmonic potential. The damping of the quadrupole mode shows the expected qualitative behavior, although the maximum in damping happens at a lower temperature compared to theory. This is consistent with the frequency data for this mode, since the transition there also happens at lower temperature. For the scissors mode the experimental data agree fairly well with theory, although some discrepancy exists at the lowest temperatures.

We can relate the frequency and damping of the quadrupole mode directly to each other by eliminating the collision rate $1/\tau$ in (3.6). Writing $\omega = \omega_Q - i\Gamma_Q$ for the solution of (3.6) with ω_Q and Γ_Q being the quadrupole frequency and damping, we obtain

$$\Gamma_Q = \sqrt{-\omega_\perp^2 - \omega_Q^2 + \sqrt{8\omega_Q^2 - 7\omega_\perp^2}}. \tag{3.10}$$

A similar relation holds for the two other modes. This allows us to compare theory and experiment independently of any approximations involved in the evaluation of $1/\tau$. Figure 3.6 shows the normalized damping rate versus the normalized frequency of the quadrupole and the scissors mode; we do not show the data for the compression mode because of the apparent problems discussed before. We find that the maximum damping of the quadrupole mode is larger than expected. For the scissors mode the damping is larger only at low frequencies. This suggests that the difference between theory and experiment is not a consequence of the approximations entering the calculation of the relaxation rate but could be due to anharmonic effects or the need for larger basis sets to describe the modes [see (3.3) and (3.4)].

3.5. Conclusion

In this work we have presented measurements of the frequency and damping of three different collective modes under similar conditions for an ultracold Fermi gas of ^{6}Li atoms in the unitarity limit. The experimental results obtained in the normal state of the gas are in reasonable agreement with our theoretical calculations, which take into account Pauli blocking and pair correlations. The remaining discrepancies may originate in a variety of sources such as our treatment of anharmonic effects, the temperature calibration, and the use of a restricted basis for solving the Boltzmann equation. Also they may reflect the need to incorporate further interaction effects in the kinetic equation, which forms the starting point for the theoretical calculations. For instance, there are self-energy shifts on the left-hand side of the kinetic equation which could be important. The study of collective modes is a sensitive probe of the properties of strongly interacting particles such as the gas of ^{6}Li atoms under investigation, and further work on temperature-dependent phenomena will undoubtedly shed more light on these interesting many-body systems.

We acknowledge support by the Austrian Science Fund (FWF) within SFB 15 (project part 21). M.J.W. was supported by a Marie Curie Incoming International Fellowship within the 6th European Community Framework Program. Fruitful discussions with S. Stringari are appreciated. We thank Q. Chen and K. Levin for providing us with density profiles and temperature calibration curves.

3.6. Appendix A

Here we present more details on the experimental procedures to excite the three collective modes.

To excite the radial quadrupole mode we adiabatically deform the radially symmetric trap to an elliptic shape while keeping the average trap frequency constant before turning off the deformation suddenly [Alt07b]. The deformation is chosen such that the amplitude of the mode oscillation relative to the cloud size is below 10%. A two-dimensional Thomas-Fermi profile is fitted to the images, taken after a short expansion time of 0.5 ms. The difference in the width of the main axes is

determined for different hold times and fitted to a damped sine function, from which we determine the frequency and damping of the mode.

The excitation of the radial compression mode is done by a sudden compression of the cloud. To determine the frequency and damping of the compression mode we follow the same procedure as for the quadrupole mode but fitting to the sum of the widths. Here we use an expansion time of 2 ms before taking the image.

The scissors mode appears as an angular oscillation of an elliptic cloud about a principal axis of an elliptic trap. To excite this oscillation we create an elliptic trap in the x-y plain and suddenly rotate the angle of the principal axes by 5 degrees [Wri07]. The tilt of the principal axes of the cloud is determined 0.8 ms after releasing the cloud from the trap for different hold time. If the gas is hydrodynamic, we fit a single damped sine function to the oscillation of the angle. However, for a collisionless gas, the oscillation exhibits two frequencies. Thus we fit a sum of two damped sine functions each with their own free parameters. When the behavior changes from hydrodynamic to collisionless the single damped sine function fits the data reasonably well, as discussed in [Wri07]. Since the larger of the two frequencies in the collisionless regime smoothly connects to the hydrodynamic frequency at low temperatures we only consider this frequency in the paper.

3.7. Appendix B

Here we briefly discuss the calculation of the transverse sloshing modes including anharmonic corrections to lowest order. The transverse trapping potential is

$$V(x,y) = V_0(1 - e^{-x^2/a^2 - y^2/b^2}) \simeq V_0\left(\frac{x^2}{a^2} + \frac{y^2}{b^2} - \frac{x^4}{2a^4} - \frac{y^4}{2b^4} - \frac{x^2y^2}{a^2b^2}\right). \tag{3.11}$$

Concentrating without loss of generality on the sloshing mode in the x-direction, we choose the function $\Phi = c_1 x + c_2 p_x$. Putting this into the linearized Boltzmann equation (3.1), eliminating c_2, and taking the moment $\int dxdyn(x,y)$ with $n(x,y)$ the density (we ignore the axial direction), we obtain for the sloshing frequency

$$\omega_s^2 = \omega_x^2\left(1 - \frac{m\omega_x^2\langle x^2\rangle + m\omega_y^2\langle y^2\rangle}{2V_0}\right). \tag{3.12}$$

Here $\langle x^2\rangle = \int n(x,y)x^2dxdy/\int n(x,y)dxdy$ and we have used $\omega_x^2 = 2V_0/ma^2$ together with $\omega_y^2 = 2V_0/mb^2$.

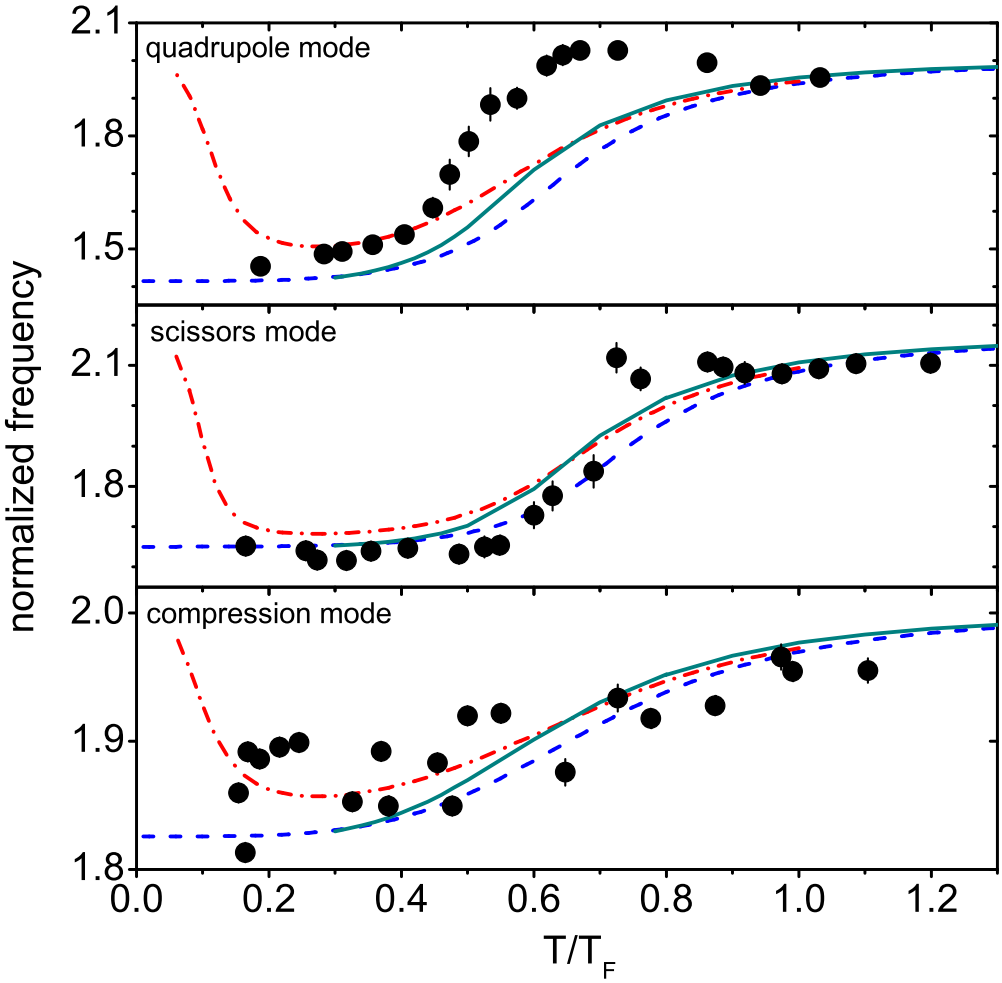

Figure 3.4.: The three panels show the observed normalized mode frequencies versus temperature for the quadrupole mode, the scissors mode and the compression mode. The error bars indicate the statistical error of a single frequency measurement. The full lines are the result of the theory for the normal state described in the section 3.3, which includes the combined effects of Pauli blocking and pair correlations; note that these curves start at $T = 0.3T_F$, which in the ladder approximation used here is the transition temperature to the superfluid state. For illustrative purposes we also show the theoretical results when only Pauli blocking is taken into account (dash-dotted lines) and those for a classical gas (dashed lines).

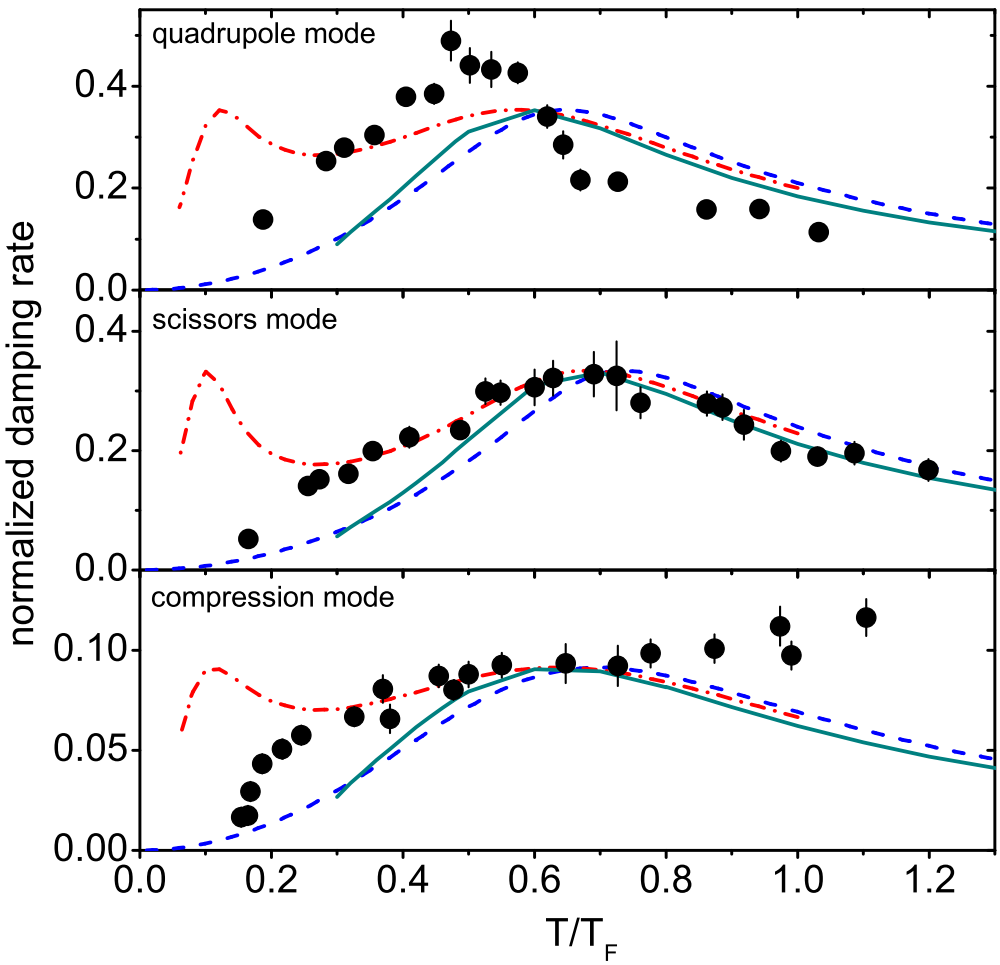

Figure 3.5.: Normalized mode damping versus temperature for the quadrupole mode, the scissors mode and the compression mode. The points are experimental values, while the full lines represent our calculated values, taking into account both Pauli blocking and pairing effects. The dash-dotted line only takes Pauli blocking into account, while the dashed line is the classical (high-temperature) result.

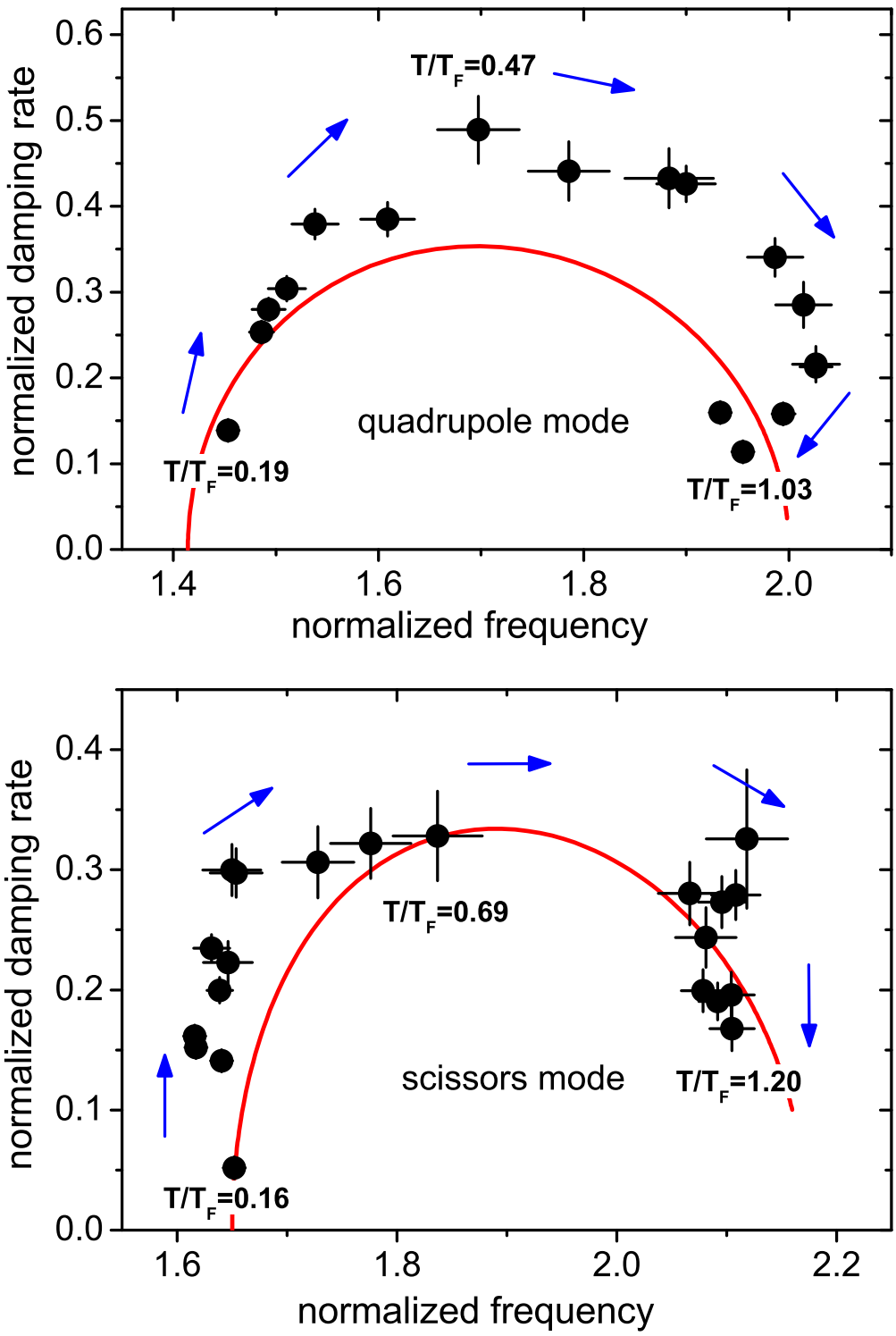

Figure 3.6.: Normalized mode damping versus normalized frequency for the quadrupole and scissors mode. The solid line shows the expected behavior for a harmonic trap. The arrows point toward the direction of increasing temperature.

4. Publication: Lifetime of angular momentum in a rotating strongly interacting Fermi gas

Phys. Rev. A 79, 053628 (2009)

S. Riedl,[1,2] E. R. Sánchez Guajardo*,[1,2] C. Kohstall,[1,2]
J. Hecker Denschlag,[1] and R. Grimm[1,2]

[1] *Institut für Experimentalphysik und Zentrum für Quantenphysik, Universität Innsbruck, 6020 Innsbruck, Austria*
[2] *Institut für Quantenoptik und Quanteninformation, Österreichische Akademie der Wissenschaften, 6020 Innsbruck, Austria*

We investigate the lifetime of angular momentum in an ultracold strongly interacting Fermi gas, confined in a trap with controllable ellipticity. To determine the angular momentum we measure the precession of the radial quadrupole mode. We find that in the vicinity of a Feshbach resonance, the deeply hydrodynamic behavior in the normal phase leads to a very long lifetime of the angular momentum. Furthermore, we examine the dependence of the decay rate of the angular momentum on the ellipticity of the trapping potential and the interaction strength. The results are in general agreement with the theoretically expected behavior for a Boltzmann gas.

4.1. Introduction

The dynamics of an ultracold quantum gas is an important source of information on the physical nature of the system. A particularly interesting situation is an atomic Fermi gas in the vicinity of a Feshbach resonance [Ing08, Gio08]. The Feshbach resonance allows us to tune the two-body interaction and thus to control the coupling between the atoms. It connects a molecular Bose-Einstein condensate (BEC) with a Bardeen-Cooper-Schrieffer (BCS) superfluid. In the crossover region between these two limiting cases the center of the Feshbach resonance is of special interest. Here the unitarity-limited interactions lead to universal behavior of the Fermi gas.

The strong two-body interactions close to the Feshbach resonance lead to very low viscosity and hydrodynamic behavior in the normal phase, similar to properties of a superfluid [Cla07, Wri07]. The coexistence of normal and superfluid hydrodynamic behavior is a special property of the strongly interacting Fermi gas, which stands in contrast to ultracold Bose gases, where deep hydrodynamic behavior is usually restricted to the superfluid condensate fraction. The low-viscosity hydrodynamic behavior leads to a long lifetime of collective motion in the system. Using collective modes the dynamics has been investigated in a broad range of temperatures and interaction strengths in the crossover region [Cla07, Wri07, Bar04a, Kin04a, Kin04b, Kin05a, Alt07a, Alt07b,

*The contribution of the author of this thesis to this work consisted in taking data, fitting the data, and participating in the data analysis.

Rie08], including the hydrodynamic regime in the normal phase. Another important collective motion is the rotation of the gas, which is of particular interest in relation to superfluidity [Zwi05].

In this Article, we study the lifetime of the angular momentum of a rotating strongly interacting Fermi gas. We determine the angular momentum using the precession of the radial quadrupole mode. This method is well established to study the angular momentum in experiments with BEC [Che00, Hal01a, Lea02]. We observe that the unique hydrodynamic behavior of the strongly interacting Fermi gas leads to particularly long lifetimes of the angular momentum. We perform a quantitative analysis of the dissipation of the angular momentum caused by the trap anisotropy for a gas in the unitarity limit. The measurements show general agreement with the expected behavior for a Boltzmann gas [GO00]. As shown in a previous study comparing experiment and theory [Rie08], a Boltzmann gas describes the behavior of a gas in the normal state with unitarity-limited interactions reasonably well. Finally we study the dependence of the lifetime on the interaction strength of the gas in the crossover region between the BEC and BCS regime.

4.2. Experimental procedure

To realize an ultracold strongly interacting Fermi gas we trap and cool an equal mixture of ^{6}Li atoms in the lowest two atomic states as described in our previous work [Joc03a, Alt07b]. We control the interparticle interaction by changing the external magnetic field in the vicinity of a broad Feshbach resonance centered at 834 G [Bar05]. The atoms are held by an optical dipole trap using a red-detuned, single focused laser beam and an additional magnetic trap along the beam; this magnetic confinement dominates over the optical confinement along the beam under the conditions of the present experiments. The resulting trap provides weak confinement along the beam (z axis) and stronger transverse confinement (x-y plane), leading to a cigar-shaped cloud. The trap is well approximated by a harmonic potential with trap frequencies $\omega_x \approx \omega_y \approx 2\pi \times 800\,\mathrm{Hz}$ and $\omega_z = 2\pi \times 25\,\mathrm{Hz}$. The trap in general also has a small transverse ellipticity, which can be controlled during the experiments. We define an average transverse trap frequency as $\omega_r = \sqrt{\omega_x \omega_y}$. The Fermi energy of the noninteracting gas is given by $E_F = \hbar(3N\omega_x\omega_y\omega_z)^{1/3} = \hbar^2 k_F^2/2M$ where $N = 5 \times 10^5$ is the total atom number, M is the atomic mass and k_F is the Fermi wave number. The corresponding Fermi temperature is $T_F = E_F/k = 1.3\,\mu\mathrm{K}$, with k the Boltzmann constant. The interaction strength is characterized by the dimensionless parameter $1/k_F a$, where a is the atomic s-wave scattering length.

To dynamically control the shape of the trapping potential in the transverse plane we use a rapid spatial modulation of the trapping laser beam by two acousto-optical deflectors, which allows us to create time-averaged trapping potentials [Alt07b]. The control over the potential shape has two different applications for the measurements. As a first application we use it to adjust the static ellipticity $\epsilon = (\omega_x^2 - \omega_y^2)/(\omega_x^2 + \omega_y^2)$ of the trap in the x-y plane. This allows us to compensate for residual ellipticity of the trapping potential, i.e. of the trapping laser beam, and also to induce a well defined ellipticity. The second application is the creation of a rotating elliptic potential with a constant ellipticity ϵ' [1]. This is needed to spin up the gas. Both the static ellipticity in the x-y plane and the rotating elliptic potential can be controlled independently. To determine the ellipticity we measure the frequency of the sloshing mode along the two principal axes of the elliptic potential. This allows controlling the ellipticity with an accuracy down to typically 0.005.

[1] $\epsilon' = (\omega_x'^2 - \omega_y'^2)/(\omega_x'^2 + \omega_y'^2)$, where ω_x' and ω_y' are the trap frequencies in the frame of the rotating potential.

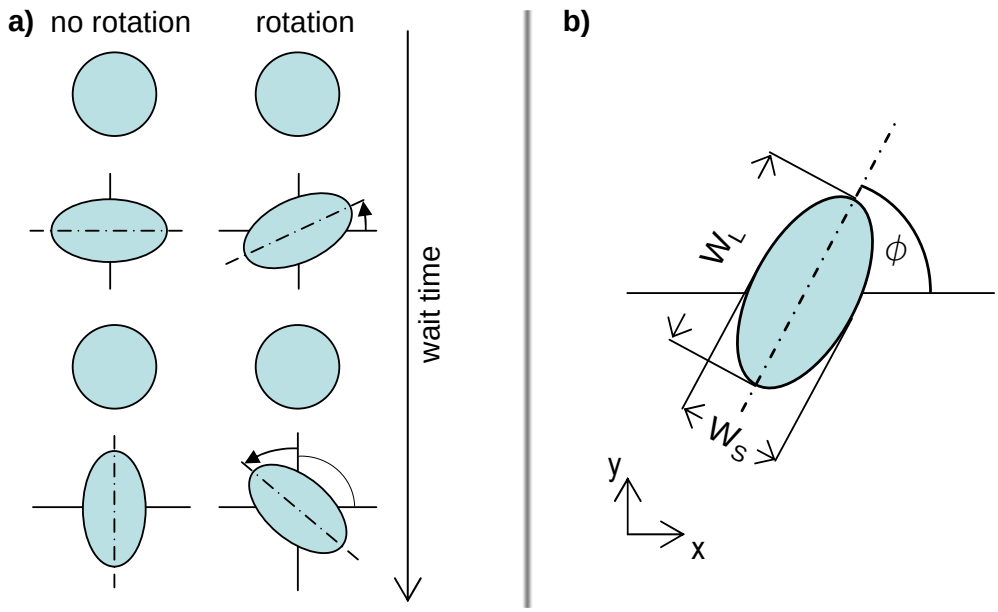

Figure 4.1.: Oscillation of the cloud after excitation of the radial quadrupole mode. For a rotating hydrodynamic gas the principal axes of the quadrupole mode oscillation precess with a frequency determined by the angular momentum of the gas. To follow the precession we measure the angle of the long axis of the cloud. Note that every half oscillation period this angle changes by $\pi/2$ because of the mode oscillation; see also Fig. 4.2. The oscillation of the cloud shape is determined by measuring the widths along the short (W_S) and the long axis (W_L) of the cloud.

To measure the angular momentum of the cloud we exploit the fact that collective excitation modes are sensitive to the rotation of the cloud. Here we use the precession of the radial quadrupole mode to determine the angular momentum of the rotating cloud; see Fig. 4.1. This method works under the general condition that the gas behaves hydrodynamically [Che03]. In our case of a strongly interacting Fermi gas, this method probes both the superfluid and the classically hydrodynamic part and does not distinguish between these two components. For the case of atomic BEC, the precession has been well studied in theory [Sin97, Dod97, Svi98, Zam98] and used in experiments to determine the angular momentum of the BEC [Che00, Hal01a, Lea02]. For an atomic BEC the non-condensed part is usually collisionless and does not contribute to the mode precession.

The radial quadrupole mode consists of two collective excitations with angular quantum numbers $m = +2$ and $m = -2$ and frequencies ω_+ and ω_-, respectively. These two excitations correspond to an elliptic deformation of the cloud rotating in opposite directions. The superposition of the excitations results in the radial quadrupole mode. For a gas at rest the two excitations are degenerate, while for a gas carrying angular momentum the frequencies are different, which causes a precession of the mode, see Fig. 4.1. The mode precesses with a frequency $\Omega_\phi = (\omega_+ - \omega_-)/4$. The

angular momentum itself can be calculated from the precession frequency [Zam98] using

$$\Omega_\phi = L_z/(2Mr_{\mathrm{rms}}^2). \tag{4.1}$$

Here L_z is the average angular momentum per atom and r_{rms}^2 is the mean value of $x^2 + y^2$ of the density distribution [2].

To excite the quadrupole mode we switch on an elliptic potential for $50\,\mu$s; this short elliptic deformation does not affect the angular momentum of the gas. For the excitation we make sure that ω_r does not change. This ensures that no compression mode is excited and only an equal superposition of the $m = \pm 2$ modes is created [Alt07b].

To follow the quadrupole oscillation we determine the angle of the long axis, ϕ, and the difference of the widths along the principle axes of the cloud, $\Delta W = W_L - W_S$, after a variable wait time in the trap; see Fig. 4.1. Therefore we fit a zero temperature, two-dimensional Thomas-Fermi profile to absorption images [3]. We also keep the angle of the long axis a free fit parameter. The width of the cloud is defined as twice the Thomas-Fermi radius.

To resolve the density distribution in the x-y plane we let the cloud expand for 0.8 ms before taking the image. The expansion does not only increase the width of the cloud but also leads to an increase of the precession angle as a consequence of the angular momentum. A quantitative analysis of the small contribution to the total precession angle that results from the expansion is given in Appendix B.

Figure 4.2 shows the evolution of the precessing quadrupole mode. The upper part shows the precession angle. The finite value of ϕ at zero wait time results from the expansion. The periodic jumps of the precession angle reflect the alternation between the long and the short axis while the quadrupole mode evolves. As the precession proceeds, these jumps become more and more smooth. This is caused by stronger damping of the $m = -2$ excitation compared to the $m = +2$ excitation. Similar behavior has been observed in Ref. [Bre03] for the case of a BEC. There the authors discuss two possible mechanisms where the difference in damping is either due to a rotating thermal cloud [Wil02] or Kelvin mode excitations [Che03]. From our measurements we cannot discriminate between these two mechanisms.

To fit the observed precession of the quadrupole mode we use the function given in Appendix A. We find very good agreement between the data and the expected behavior. For the data set shown in Fig. 4.2 the angular momentum is $1.7\hbar$. The average damping rate is $(\Gamma_- + \Gamma_+)/2 = (460 \pm 30)\,\mathrm{s}^{-1}$, while the difference in the damping rate of the $m = -2$ compared to the $m = +2$ excitation is $\Gamma_- - \Gamma_+ = (80 \pm 40)\,\mathrm{s}^{-1}$.

We find that a simplified procedure can be used to determine the angular momentum from a single measurement, instead of fitting the whole precession curve. If the measurement is taken at a time when ΔW^2 has a local maximum, the precession angle ϕ is independent of the distortion caused by the difference in the damping rates between the two excitations; see Fig. 4.2. This allows us to determine the difference $\omega_+ - \omega_- = 4\,\phi/\Delta t$ and therefore to determine L_z with a single measurement. The duration Δt is the sum of the wait time in the trap and an effective precession

[2] We determine r_{rms} at unitarity from the trap parameters using $E_F = 2M\omega_r^2 r_{\mathrm{rms}}^2\sqrt{1+\beta}$ where we used the universal scaling parameter $\beta = -0.56$ [Gio08]. Note that this underestimates r_{rms} by a few percent because it does not take into account the finite temperature and the rotation of the gas. This does not affect the measurement of the lifetime of rotation as this depends on the relative change of L_z.

[3] For the parameters used in the experiment a zero temperature Thomas-Fermi profile fits the density distribution reasonably well.

time t_e, which accounts for the precession of the quadrupole mode during expansion as discussed in Appendix B. Depending on the damping of the mode oscillation we measure the precession angle at the first or second maximum of ΔW^2 [4].

To determine the temperature of the gas in the unitarity limit we first adiabatically change the magnetic field to 1132 G [5], where $1/k_F a \approx -1$, to reduce the effect of interactions on the density distribution [Luo07]. Under this condition, for $T > 0.2T_F$, the interaction effect on the density distribution is sufficiently weak to treat the gas as a noninteracting one and to determine the temperature from time-of-flight images. We fit the density distribution after 2 ms release from the trap to a finite-temperature Thomas–Fermi profile. The temperature measured at 1132 G is converted to the temperature in the unitarity limit under the assumption that the conversion takes place isentropically, following the approach of Ref. [Che05].

4.3. Spinning up the gas

To spin up the gas we introduce a rotating anisotropy into the initially round trap in the x-y plane. More specifically, we suddenly switch to a rotating elliptic trap potential with a rotation frequency Ω_t and ellipticity $\epsilon' = 0.03$, rotate for a time t_{rot} on the order of 100 ms, and then ramp down the ellipticity in 50 ms while the trap is still rotating.

In the case of hydrodynamic behavior of the gas this spinning up method is resonantly enhanced in a certain range of rotation frequencies; see Fig. 5.3. The reason for this behavior is the resonant excitation of quadrupolar flow which leads to a dynamic instability when Ω_t is close to half the oscillation frequency of the radial quadrupole mode $\omega_q/2 = 0.71\,\omega_r$. This effect was used to nucleate vortices in a BEC [Mad00] and was further studied in Refs. [Mad01, Hod02]. A signature of the resonant excitation is a strong elliptic deformation of the cloud shape which exceeds the ellipticity of the trap ϵ' during the spin-up process. We clearly see this effect when we spin up the gas. We also find that the rotation frequency where L_z starts to increase strongly depends on ϵ' and t_{rot} in a similar way as it was observed in Refs. [Mad01, Hod02]. Note that we cannot draw any conclusion concerning superfluidity from the resonant behavior of L_z in Fig. 5.3 because it is only a consequence of hydrodynamic behavior and the strongly interacting gas is hydrodynamic both below and above T_c. In fact, for temperatures clearly above T_c we find similar behavior for L_z as a function of Ω_t.

For an atomic BEC, L_z was found to first increase abruptly from 0 to $1\hbar$ with Ω_t, caused by the appearance of a centered vortex [Che00]. As the formation of pairs is necessary for superfluidity in the BEC-BCS crossover regime, the angular momentum per atom of a single vortex in the center of the cloud amounts to $L_z = \hbar/2$. We do not observe such an abrupt increase of L_z. Nevertheless this does not exclude that vortices are created during our spin-up process; the abrupt change of L_z is not a necessary consequence of the creation of vortices as the angular momentum of a vortex depends on its position in an inhomogeneous gas [Che00]. Furthermore our measurement of L_z cannot distinguish between the angular momentum carried by the superfluid and the normal part of the cloud. Also we cannot directly observe vortices in our absorption images; we believe that the reason is the very elongated cloud which strongly decreases the contrast of the vortex core in

[4] Note that the frequency of quadrupole mode oscillation ω_q depends on the rotation frequency of the gas via $\omega_q^2 = 2\omega_r^2 - \Omega^2$. This leads to a tiny shift of the maxima of ΔW^2 but does not affect our measurement of L_z within our experimental uncertainty.

[5] This is the largest magnetic field where absorption images can be taken with our current experimental setup.

the absorption images.

During our spin-up process we observe a significant heating of the gas depending on the rotation frequency and the rotation time. We keep these two parameters as small as possible. We find that a rotation frequency of $\Omega_t/\omega_r = 0.6$ and $t_{\mathrm{rot}} = 200\,\mathrm{ms}$ lead to an angular momentum of about $L_z = 2\hbar$. This is sufficient to perform the measurements, and at the same time does only moderately increase the temperature.

We determine the temperature of the gas after the spin-up process. To avoid complications in the temperature measurement we wait until the rotation has completely decayed. To keep this wait time short, on the order of 100 ms, we speed up the decay by increasing the ellipticity of the trap; see discussion below. Note that the low initial angular momentum used in the experiments, always staying below $3\hbar$, does not lead to a significant increase in the temperature when the rotation energy is completely converted into heat [6].

4.4. Lifetime of the angular momentum

In an elliptic trap the angular momentum is not a conserved quantity and hence can decay. The dissipation of L_z is due to friction of the gas caused by the trap anisotropy. Here we investigate the dependence of the decay of L_z on the static ellipticity for the case of unitarity-limited interactions. We compare our experimental results to the predicted behavior for a rotating Boltzmann gas [GO00]. Finally we study the dependence of the decay rate on the interaction strength in the BEC-BCS crossover regime.

The fact that the gas consists of two different components, the normal and the superfluid part, leads in general to a complex behavior for the decay of L_z. For example, in the case of a BEC an exponential decay is related to the co-rotation of the thermal cloud with the condensate [Zhu01, Abo02]. When the thermal cloud is not rotating, theoretical [Zhu01] and experimental [Mad00] studies show nonexponetial behavior. For a gas completely in the hydrodynamic regime it is expected that the decrease in L_z has an exponential form [GO00].

To measure the decay rate of the angular momentum we use the following procedure. After spinning up the gas as discussed in Sec. 4.3, we slowly increase the static ellipticity within 10 ms, wait for a certain hold time to let the angular momentum partially decay and then we remove the ellipticity again within 10 ms. Finally we excite the radial quadrupole mode and observe the precession to determine L_z using the simplified procedure discussed earlier.

In Figure 4.4 we show two examples for the decay of L_z. We find that the decay of the angular momentum perfectly fits an exponential behavior for all the static ellipticities, temperatures, and interaction strengths we used. For the lowest temperatures obtained the lifetime for a gas in the unitarity limit goes up to 1.4 s, presumably limited by a residual anisotropy of the trap. This lifetime is by more than a factor of thousand larger then the radial trap oscillation period. Furthermore the lifetime of the angular momentum is much larger than the lifetime of collective excitation modes. For example the lifetime of the radial quadrupole mode under the same conditions is only 2 ms. A larger ellipticity of the trap significantly decreases the lifetime of L_z.

[6] To estimate the increase of the temperature through the decay of the rotation we assume that the rotation energy is completely converted into heat. In the experiments L_z is well below $3\hbar$ which leads to a relative temperature increase of $\Delta T/T < 0.02$ in the relevant temperature range. This is clearly below the uncertainty of our temperature measurement.

In the following we investigate quantitatively the dependence of the decay rate of the angular momentum, λ, on ellipticity and temperature. The experimental results are shown in Fig. 4.5 for two different temperatures. The full circles display the data for a temperature of $T/T_F = 0.22(3)$ and the open circles correspond to a temperature of $T/T_F = 0.35(2)$. For better comparison with theory we plot the normalized decay rate λ/ω_r. A strong increase of the decay rate with increasing ellipticity shows the important role of the trap anisotropy on the lifetime of the angular momentum. For both temperatures the qualitative behavior of the decay rate is the same.

Next we compare the behavior of the decay rate with a theoretical prediction for a Boltzmann gas [GO00]. As we showed recently in Ref. [Rie08], a Boltzmann gas describes the behavior of a unitarity-limited gas in the normal state reasonably well. The predicted behavior of the decay rate is given by $\lambda/\omega_r = 2\epsilon^2\omega_r\tau$ under the assumption that $\epsilon \ll 1/(4\omega_r\tau)$ [7], where τ is the relaxation time or effective collision time [Rie08, Vic00, Hua87]. This condition is well fulfilled in our system because the gas is in the hydrodynamic regime where $\omega_r\tau \ll 1$. We compare this theoretical prediction, with τ as a free parameter, to our measurements. We find $\omega_r\tau = 0.108(5)$ for the lower temperature and $\omega_r\tau = 0.28(1)$ for the higher temperature data.

Note that at very low ellipticity, $\epsilon < 0.02$, the observed decay rate for both temperatures lies significantly above the expected behavior; see inset of Fig. 4.5. We attribute this to an additional anisotropy of the trap beyond simple ellipticity. This weak anisotropy becomes relevant only at very low ϵ. Furthermore the finite linear heating rate of the trapped gas of $0.05\,T_F\,\mathrm{s}^{-1}$ becomes important when the decay rate is very low, which means that the lifetime of L_z is on the order of seconds. In this case the temperature cannot be assumed to be constant during the decay of L_z.

A recent calculation of the relaxation time τ for a Fermi gas in the unitarity limit [Rie08] allows us to compare the experimental values for $\omega_r\tau$ to theory. For $T/T_F = 0.35$ the obtained relaxation time of $\omega_r\tau = 0.28$ is clearly larger than the calculated value of $\omega_r\tau = 0.13$. This means that the theory predicts that the gas is somewhat deeper in the hydrodynamic regime compared to the experimental findings. Similar deviations showed up when the theory was compared to the temperature dependence of collective oscillations [Rie08]. For the lower temperature the obtained value for $\omega_r\tau$ cannot be compared to the calculation of Ref. [Rie08] as the theory is restricted to higher temperatures.

Finally we study the decay of the angular momentum in the crossover region between the BEC and BCS regimes. We measure the decay rate for different interaction parameters $1/k_Fa$. The experimental sequence is the same as for the decay rate in the unitarity limit beside ramping the magnetic field to the desired value in 100 ms before increasing the ellipticity and ramping back the magnetic field in 100 ms before exciting the quadrupole mode. Here the magnetic field is changed slowly such that the gas is not collectively excited. The ellipticity for all magnetic fields is set to be $\epsilon = 0.09$. This sizeable value of ϵ ensures that a small anisotropy beyond ellipticity does not affect the decay rate and makes the measurement less sensitive to heating while the angular momentum damps out as discussed above.

Figure 4.6 shows the decay rate of the angular momentum as a function of the interaction strength. The lifetime is largest where the interaction is strongest and accordingly the relaxation time is short. In addition to the two-body interaction strength, pairing effects play an important role for the relaxation time [Rie08]. This might explain the higher decay rates for $1/k_Fa < 0$, where the pairing is weak, compared to the decay rates for $1/k_Fa > 0$, where the atoms are bound to molecules. Similar behavior has been seen in [Zwi05] for the lifetime of a vortex lattice. Note that

[7] For the temperatures used in the measurements $1/(4\omega_r\tau) > 0.9$ for a gas in the unitarity limit.

Ref. [Zwi05] also reports a decrease of the lifetime in a narrow region around $1/k_F a = 0$, which we do not observe for our trap parameters.

In summary the hydrodynamic behavior in the crossover region leads to a very long lifetime of L_z.

4.5. Conclusion

In this work we have presented measurements on a strongly interacting Fermi gas carrying angular momentum. The angular momentum of the gas exhibits long lifetimes due to the deeply hydrodynamic behavior of the normal state in such a system. We investigated the decay rate of the angular momentum depending on the ellipticity of the trapping potential for two different temperatures. We find that the experimental results are in good agreement with the expected behavior for a simple Boltzmann gas. The dependence of the decay rate of the angular momentum on the interaction strength in the BEC-BCS crossover region confirms that collective motion is very stable as long as the interaction strength is sufficiently large.

The long lifetime of the angular momentum in a rotating strongly interacting Fermi gas allows us to further investigate rotational properties both in the superfluid and normal phase in detail and with high precision. Currently we investigate the moment of inertia of the gas for different temperatures [Rie11].

We acknowledge support by the Austrian Science Fund (FWF) within SFB 15 (project part 21) and SFB 40 (project part 4).

4.6. Appendix A

To calculate the precession angle and the oscillation of the width we assume that the frequency and damping rate for the $m = \pm 2$ excitations are independent. For the damping of each excitation we assume a exponential behavior. A superposition of the two excitations results in the fit function for the precession angle [Bre03]

$$\tan\left(2(\phi - \phi_e)\right) = \frac{e^{-(\Gamma_+ - \Gamma_-)t}\sin\left(\omega_+ t + 2\phi_0\right) - \sin\left(\omega_- t + 2\phi_0\right)}{e^{-(\Gamma_+ - \Gamma_-)t}\cos\left(\omega_+ t + 2\phi_0\right) + \cos\left(\omega_- t + 2\phi_0\right)} \tag{4.2}$$

Here $\omega_\pm$ are the frequencies, $\Gamma_\pm$ are the damping rates, ϕ_0 is the initial angle for the two excitations and ϕ_e is the precession angle resulting from the expansion of the cloud. For the oscillation of the width difference ΔW we get

$$\begin{aligned} \Delta W^2 &= 4Ae^{-(\Gamma_+ + \Gamma_-)t}\cos^2\left(\frac{(\omega_+ + \omega_-)}{2}t + 2\phi_0\right) \\ &+ A(e^{-\Gamma_+ t} - e^{-\Gamma_- t})^2, \end{aligned} \tag{4.3}$$

where A is the amplitude of the oscillation.

4.7. Appendix B

Here we calculate the effect of the expansion of the cloud on the precession angle. Assuming conservation of angular momentum during the expansion, the rotation frequency Ω of the gas decreases as the size of the cloud is increasing. We introduce an effective precession time t_e which accounts for the changing precession angle ϕ during expansion. The total change of the precession angle resulting from the expansion is given by

$$\phi_e = \int_0^{t_{\mathrm{TOF}}} \dot{\phi}(t)dt = \dot{\phi}(0)t_e, \tag{4.4}$$

where $\dot{\phi}(0)$ is the precession frequency when the gas is still trapped and t_{TOF} is the expansion time. Assuming that also during the expansion $\dot{\phi}(t) = L_z/(2Mr^2_{\mathrm{rms}}(t))$ is still valid and inserting this into Eq. 4.4 we get

$$t_e = \int_0^{t_{\mathrm{TOF}}} r^2_{\mathrm{rms}}(0)/r^2_{\mathrm{rms}}(t)dt. \tag{4.5}$$

To calculate the relative increase of the cloud size during expansion, $r^2_{\mathrm{rms}}(t)/r^2_{\mathrm{rms}}(0)$, we use the scaling approach; see e.g. [Alt07b]. For our experimental parameters, $\omega_r = 800\,\mathrm{Hz}$ and $t_{\mathrm{TOF}} = 0.8\,\mathrm{ms}$, we get an effective precession time of $t_e = 0.26\,\mathrm{ms}$. This is shorter than the typical precession time in the trap of $0.75\,\mathrm{ms}$.

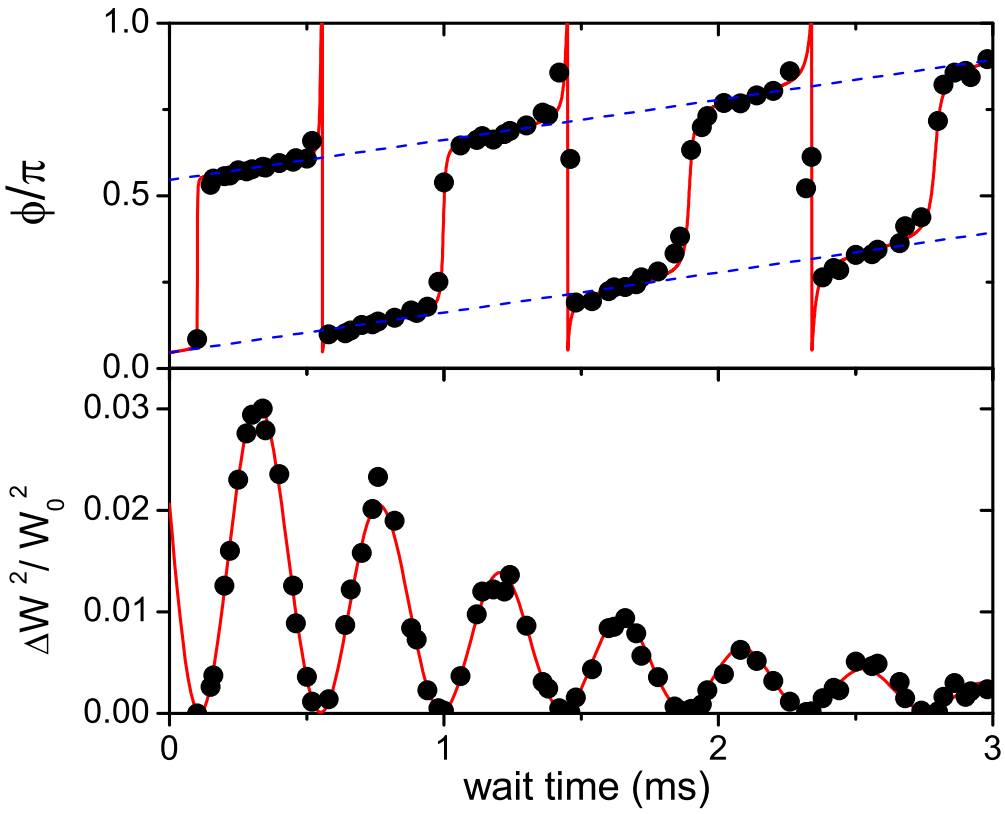

Figure 4.2.: Evolution of the quadrupole mode in a rotating Fermi gas in the unitarity limit. The upper panel shows the precession of the principal axes of the mode. The experimental data are shown by the dots. The solid line represents a fit according to Eq. 4.2. The dashed lines correspond to the idealized precession of the angle when there is no damping present in the mode. Whenever the oscillation of the difference in widths $\Delta W^2/W_0^2$ (lower panel) has a local maximum the observed precession angle coincides with the idealized precession. The parameter W_0 is the average width of the cloud. The finite value of ϕ at zero wait time results from the precession of the cloud during expansion. Here $L_z = 1.7\hbar$ and $T/T_F \approx 0.2$.

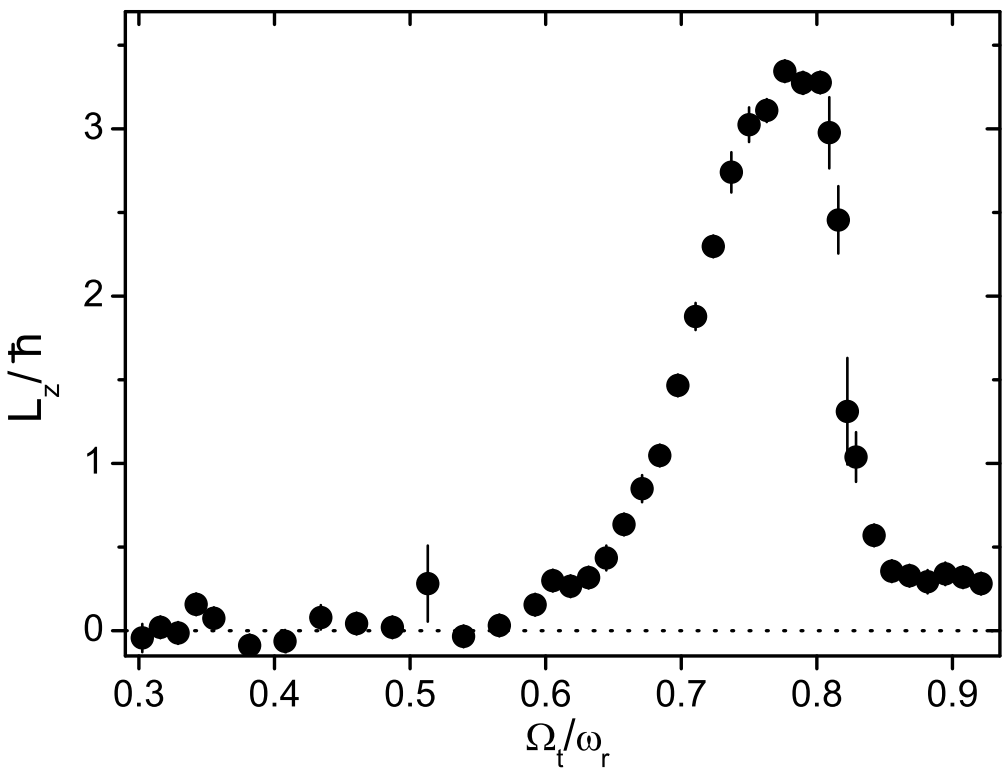

Figure 4.3.: The angular momentum L_z as a function of the rotation frequency Ω_t of the elliptic trap. Here we spin up the gas for $t_{\mathrm{rot}} = 60\,\mathrm{ms}$. The temperature is $T/T_F \approx 0.2$. The gas is in the unitarity limit.

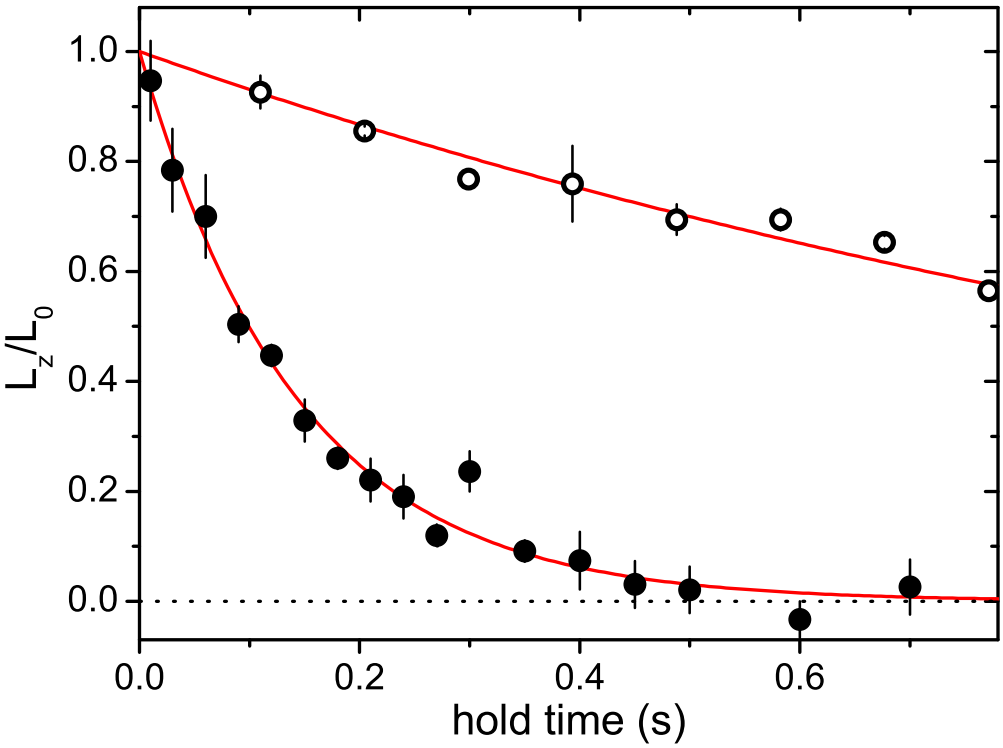

Figure 4.4.: Decay of the angular momentum L_z for a gas in the unitarity limit. The temperature is $T/T_F = 0.22(3)$. We fit an exponential decay behavior (solid lines) to the experimental data points. For low ellipticity $\epsilon = 0.009$ (open dots) the lifetime is 1.4 s, while at higher ellipticity $\epsilon = 0.1$ (filled dots) the lifetime is only 0.14 s. To better see the difference of the lifetime for the two ellipticities we normalized L_z by its initial value L_0. For the lower ellipticity $L_0 = 2.2\hbar$ and for the higher ellipticity $1.6\hbar$.

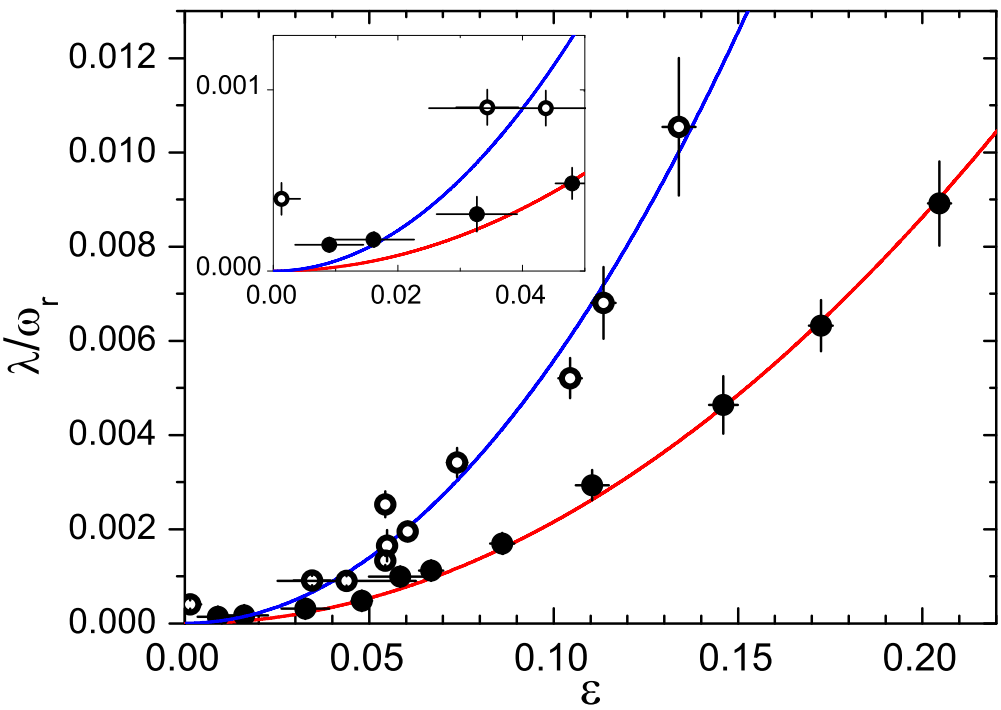

Figure 4.5.: Normalized decay rate of the angular momentum as a function of the ellipticity for a gas in the unitarity limit. The temperatures are $T/T_F = 0.22(3)$ (filled dots) and $0.35(2)$ (open dots). The solid lines are fits based on the expected behavior for a Boltzmann gas [GO00]. The inset shows the low ellipticity region.

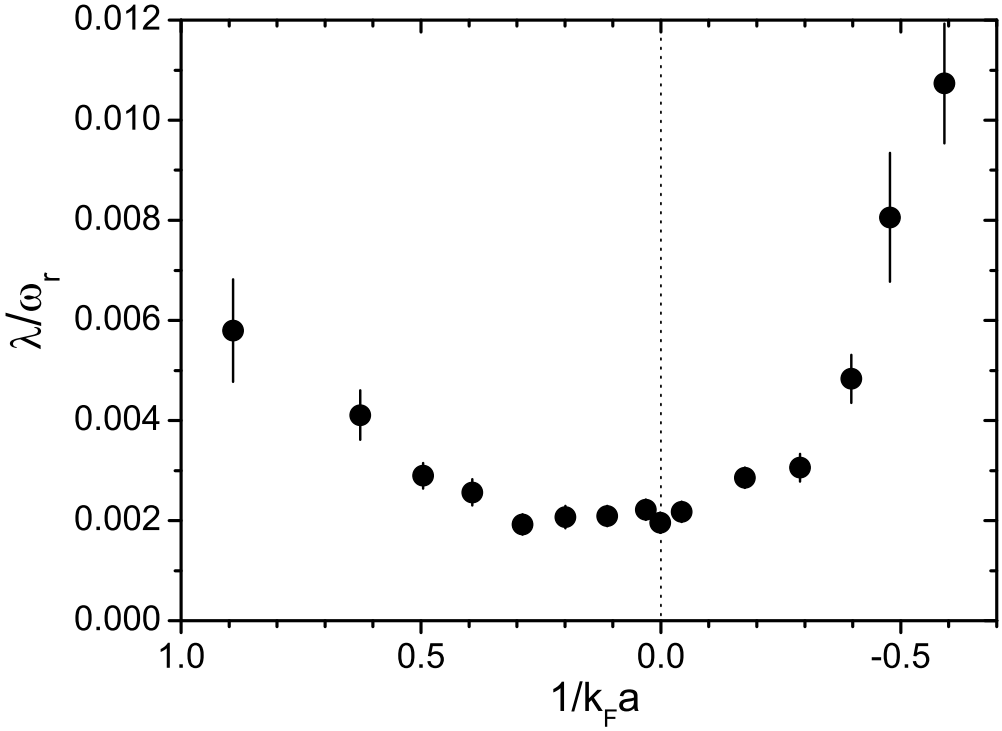

Figure 4.6.: Lifetime of the angular momentum versus interaction parameter $1/k_F a$ for $\epsilon = 0.09$. The temperature for $1/k_F a = 0$ is $T/T_F = 0.22(3)$.

5. Publication: Superfluid quenching of the moment of inertia in a strongly interacting Fermi gas

New J. Phys. 13, 035003 (2011)

S. Riedl,[1,2] E. R. Sánchez Guajardo*,[1,2] C. Kohstall,[1,2]
J. Hecker Denschlag,[1] and R. Grimm[1,2]

[1] *Institut für Experimentalphysik und Zentrum für Quantenphysik, Universität Innsbruck, 6020 Innsbruck, Austria*
[2] *Institut für Quantenoptik und Quanteninformation, Österreichische Akademie der Wissenschaften, 6020 Innsbruck, Austria*

We report on the observation of a quenched moment of inertia as resulting from superfluidity in a strongly interacting Fermi gas. Our method is based on setting the hydrodynamic gas in slow rotation and determining its angular momentum by detecting the precession of a radial quadrupole excitation. The measurements distinguish between the superfluid and collisional origins of hydrodynamic behavior, and show the phase transition.

5.1. Introduction

Superfluidity is a striking property of quantum fluids at very low temperatures. For bosonic systems, important examples are liquids and clusters of ^{4}He and atomic Bose-Einstein condensates. In fermionic systems, superfluidity is a more intricate phenomenon as it requires pairing of particles. Fermionic superfluidity is known to occur in atomic nuclei and ^{3}He liquids and it is also at the heart of superconductivity, thus being of great technological importance. Recent advances with ultracold Fermi gases have opened up unprecedented possibilities to study the properties of strongly interacting fermionic superfluids [Gio08, Ing08]. Early experiments on ultracold Fermi gases with resonant interparticle interactions compiled increasing evidence for superfluidity [O'H02a, Reg04b, Kin04a, Bar04a, Chi04a, Kin05b] until the phenomenon was firmly established by the observation of vortex lattices [Zwi05].

Here we report on the manifestation of superfluidity in a quenched moment of inertia (MOI) in a strongly interacting Fermi gas that undergoes slow rotation. The basic idea of a quenched MOI as a signature of superfluidity dates back to more than 50 years ago in nuclear physics, where MOIs below the classical, rigid-body value were attributed to superfluidity [Rin80]. The quenching of the

*The contribution of the author of this thesis to this work consisted in taking data, and participating in the interpretation and discussion of the results.

MOI was also shown in liquid ^{4}He [Hes67] and has, more recently, served for the discovery of a possible supersolid phase [Kim04a]. Here we introduce the observation of the quenched MOI as a new method to study superfluidity in ultracold Fermi gases.

5.2. Basic idea of the measurement

The basic situation that underlies our experiments is illustrated in Fig. 5.1. At a finite temperature below the critical temperature T_c, the harmonically trapped cloud consists of a superfluid core centered in a collisionally hydrodynamic cloud. We assume that the trapping potential is close to cylindrical symmetry, but with a slight, controllable deformation that rotates around the corresponding axis with an angular velocity Ω_{trap}. The nonsuperfluid part of the cloud is then subject to friction with the trap and follows its rotation with an angular velocity Ω [1], which in a steady state ideally reaches $\Omega = \Omega_{\text{trap}}$. The corresponding angular momentum can be expressed as $L = \Theta\Omega$, where Θ denotes the MOI. The superfluid core cannot carry angular momentum, assuming that vortex nucleation is avoided, and therefore does not contribute to the MOI of the system. Thus Θ represents the MOI of the whole system.

The case of a rotating system in a steady state, where the normal part carries the maximum possible angular momentum, allows us to distinguish the superfluid quenching of the MOI from a non-equilibrium quenching effect as studied in Ref. [Cla07]. There the authors investigated the hydrodynamic expansion of a gas with a known angular momentum. This situation, where the velocity fields of the normal and superfluid components are not in a steady state, can also be discussed in terms of a MOI below the rigid-body value. In contrast to the phenomenon investigated in our present work, the effect of Ref. [Cla07] is related to irrotational flow and can occur for both the superfluid and the collisionally hydrodynamic normal phase.

Our measurements rely on the possibility to determine the total angular momentum L of a rotating hydrodynamic cloud by detecting the precession of a radial quadrupole excitation. This method is well established and has been extensively used in the context of atomic Bose-Einstein condensates [Che00, Hal01a, Lea02]. We have recently applied it to a rotating, strongly interacting Fermi gas to investigate the slow decay of angular momentum [Rie09]. The method works under the general condition that the gas behaves hydrodynamically. Then the precession frequency can be written as $\Omega_{\text{prec}} = L/(2\Theta_{\text{rig}})$ [Zam98], where Θ_{rig} corresponds to a moment of inertia as calculated from the density distribution under the assumption that the whole cloud, including the superfluid part, would perform a rigid rotation. Substituting $\Theta\Omega$ for L, we obtain $\Omega_{\text{prec}} = \Theta/(2\Theta_{\text{rig}})\ \Omega$, with $\Theta/\Theta_{\text{rig}} = 1$ for the full MOI in a normal system, and $\Theta/\Theta_{\text{rig}} < 1$ for a MOI that is quenched because of the superfluid core.

5.3. Experimental setup and procedures

The starting point of our experiments is an optically trapped, strongly interacting Fermi gas consisting of an equal mixture of ^{6}Li atoms in the lowest two atomic states [Joc03a, Alt07b]. The broad 834-G Feshbach resonance [Ing08] allows us to control the s-wave interaction. If not otherwise stated, the measurements presented here refer to the resonance center. Here a unitarity-limited

[1] We assume that the normal cloud performs a rigid rotation with an angular velocity Ω. This can be justified by the internal friction in the non-superfluid component along with the fact that the rotating trap deformation is applied to all regions of the cloud simultaneously.

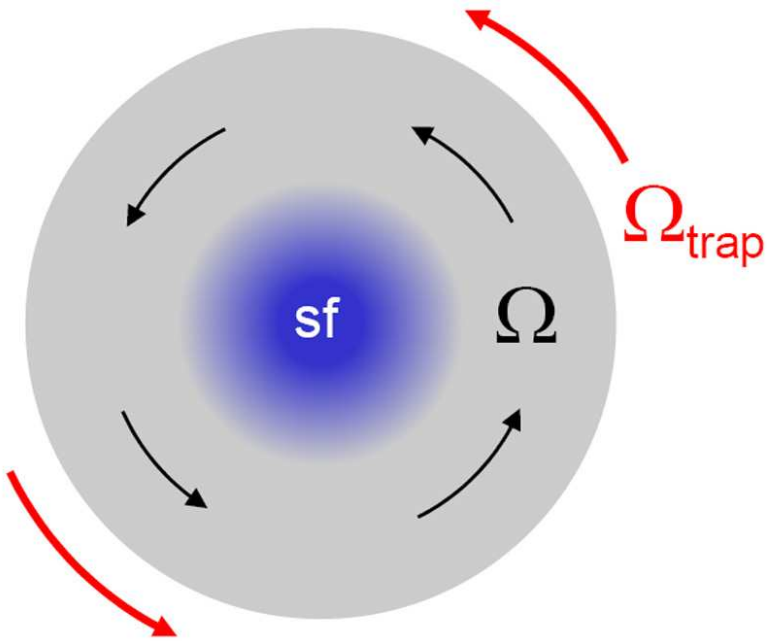

Figure 5.1.: Schematic illustration of a strongly interacting Fermi gas in a slowly rotating trap. The normal part rotates with a frequency Ω, which in an equilibrium state approaches the rotation frequency Ω_{trap} that is imposed by the trap. The superfluid core (sf) does not carry angular momentum and therefore does not contribute to the MOI.

Fermi gas [Gio08, Ing08] is realized, which is known to exhibit deep hydrodynamic behavior even well above the critical temperature for superfluidity, see e.g. [Wri07]. The cigar-shaped quantum gas is confined in a far red-detuned, single-beam optical dipole trap with additional axial magnetic confinement. The trap can be well approximated by a harmonic potential with radial oscillation frequencies $\omega_x = \omega_y \approx 2\pi \times 680\,\text{Hz}$ and an axial frequency of $\omega_z = 2\pi \times 24\,\text{Hz}$. The Fermi energy of the noninteracting gas is given by $E_F = \hbar(3N\omega_x\omega_y\omega_z)^{1/3}$, where $N = 6 \times 10^5$ is the total atom number. The Fermi temperature is $T_F = E_F/k = 1.3\,\mu\text{K}$, with k denoting the Boltzmann constant.

Our scheme to study the rotational properties is described in detail in Ref. [Rie09]. It is based on a rotating elliptical deformation of the trap, characterized by a small ellipticity parameter [Rie09] $\epsilon' = 0.1$. In contrast to our previous work, we use a lower rotation frequency of $\Omega_{\text{trap}} = 2\pi \times 200\,\text{Hz}$ $\approx 0.3\,\omega_x$. This low value allows us to avoid a resonant quadrupole mode excitation, which is known as an efficient mechanism for vortex nucleation [Mad01, Hod02]. To excite the quadrupole mode [Alt07b] we switch on an elliptic trap deformation for $50\,\mu$s. We detect the resulting oscillation by taking absorption images of the cloud after a variable hold time in the trap and a short free expansion time after release from the trap. More details on this excitation and detection scheme are given in Ref. [Rie09].

At this point it is important to discuss the consequences of residual trap imperfections, still present when we attempt to realize a cylindrically symmetric optical potential. As we showed in previous work [Rie09], we can control the ellipticity down to a level of $\sim$1%. Moreover, deviations

from perfect cylindrical symmetry may occur because of other residual effects, such as corrugations of the optical trapping potential. As a consequence, a certain rotational damping is unavoidable, but damping times can reach typically one second [Rie09]. This has two main effects for our observations. First, our measurements yield precession frequencies slightly below Ω_{prec}. This is because of a delay time of 20 ms between turning off the rotating trap ellipticity and applying the quadrupole mode excitation. It is introduced to make sure that any possible collective excitation resulting from the rotating trap has damped out when the mode precession is measured. Because of rotational damping during this delay time, the measured precession frequencies Ω'_{prec} are somewhat below Ω_{prec}. To compensate for this effect, we directly measure the reduction of Ω_{prec} that occurs during a 20 ms hold time to determine the corresponding damping parameter $\kappa = \Omega'_{\mathrm{prec}}/\Omega_{\mathrm{prec}}$ for each set of measurements, finding day-to-day variations with typical values between 0.85 and 0.9. The second effect is induced by friction with static (nonrotating) trap imperfections when the rotating ellipticity is applied. This leads to equilibrium values for Ω typically a few percent below Ω_{trap}, depending on the ratio between the time constants for spin up and damping [GO00]. For this second effect there is no straightforward compensation, and it needs to be explicitly discussed when interpreting the experimental results.

Thermometry is performed after the whole experimental sequence. We damp out the rotation by stopping the trap rotation and keeping the ellipticity [2]. We convert the gas into a weakly interacting one by a slow magnetic field ramp to 1132 G, and we finally measure the temperature $\mathcal{T}$ [Rie09]. Note that the isentropic conversion tends to decrease the temperature such that $\mathcal{T}$ is always somewhat below the temperature T at unitarity [Che05]. The relative statistical uncertainty of the temperature measurement is about 5% in the relevant temperature range.

5.4. Experimental results

To discuss our experimental results we introduce a dimensionless precession parameter $\mathcal{P}$ by normalizing our observable Ω_{prec} to its maximum possible value of $\Omega_{\mathrm{trap}}/2$,

$$\mathcal{P} = 2\,\frac{\Omega_{\mathrm{prec}}}{\Omega_{\mathrm{trap}}} = \frac{\Theta}{\Theta_{\mathrm{rig}}} \times \frac{\Omega}{\Omega_{\mathrm{trap}}}\,. \tag{5.1}$$

The maximum possible value of $\mathcal{P} = 1$ corresponds to a fully rotating, classically hydrodynamic cloud. Values $\mathcal{P} < 1$ show the presence of at least one of the two effects, namely the incomplete rotation of the normal part ($\Omega/\Omega_{\mathrm{trap}} < 1$) or the superfluid quenching of the MOI ($\Theta/\Theta_{\mathrm{rig}} < 1$). It is crucial for the interpretation of our experimental results to distinguish between these two effects. Our basic idea to achieve this relies on the fact that $\Theta/\Theta_{\mathrm{rig}}$ represents a temperature-dependent *equilibrium* property, whereas $\Omega/\Omega_{\mathrm{trap}}$ depends on the dynamics of the spin-up before the system has reached an equilibrium. Experimentally, however, measurements of equilibrium properties at a fixed temperature are not straightforward because of the presence of residual heating leading to a slow, steady temperature increase. In the rotating trap we always observe some heating, which under all our experimental conditions can be well described by a constant rate $\alpha = 170\,\mathrm{nK/s} = 0.13\,T_F/\mathrm{s}$ [3].

[2] The temperature increase resulting from conversion of rotational energy into heat is neglibly small.

[3] To determine the temparature increase in the rotating trap we measure $\mathcal{T}$ after variable rotation times. We find that, in the relevant temperature range, the behavior of $\mathcal{T}$ is well approximated by a linear increase with time. This justifies the description in terms of a constant heating rate.

5.4.1. Equilibrium state of rotation

To identify the conditions under which our cloud reaches its equilibrium state of rotation, we have developed a special procedure based on the timing scheme illustrated on top of Fig. 5.2. Our procedure takes advantage of the constant heating rate α to control the final temperature of the gas when $\mathcal{P}$ is measured. We apply the trap rotation in two separate stages of duration t_{heat} and t_{spin}. In an intermediate time interval of $t_{\mathrm{damp}} = 200\,\mathrm{ms}$ [4] we damp out the rotation that is induced by the first stage. The angular momentum disappears, but the heating effect remains [5]. The second stage spins up the cloud again and induces further heating. When $t_{\mathrm{tot}} = t_{\mathrm{heat}} + t_{\mathrm{spin}}$ is kept constant, we find that the total heating by the two rotation stages is $\Delta\mathcal{T} = \alpha\, t_{\mathrm{tot}}$. As only the second stage leads to a final angular momentum, the equilibrium state reached at a constant temperature can be identified when $\mathcal{P}(t_{\mathrm{spin}})$ reaches a constant value for increasing t_{spin} and fixed t_{tot}. The temperature can be controlled by a variation of the parameter t_{tot} and is obtained as $\mathcal{T} = \mathcal{T}_0 + \Delta\mathcal{T}$. The temperature offset $\mathcal{T}_0$ is set by the initial cooling and some unavoidable heating during the experimental sequence without trap rotation. Under our conditions $\mathcal{T}_0 \approx 0.11\, T_F$.

Our experimental results for $\mathcal{P}(t_{\mathrm{spin}})$ are shown in Fig. 5.2 for four different values of the heating parameter $\Delta\mathcal{T}/T_F$ in a range between 0.026 to 0.104, which corresponds to a range of $\mathcal{T}$ between about 0.14 and $0.21\, T_F$. All four curves show qualitatively the same behavior. Within a few 100 ms, $\mathcal{P}$ rises before reaching a final equilibrium value. This time-dependent increase of $\mathcal{P}$ is related to the spin-up dynamics [6]. We find that the observed increase and saturation of $\mathcal{P}(t_{\mathrm{spin}})$ can be well fit by simple exponential curves (solid lines), and we use these fits to extract the different equilibrium values $\mathcal{P}_{\mathrm{eq}}$.

The equilibrium values $\mathcal{P}_{\mathrm{eq}}$ exhibit an interesting temperature dependence. The lower three values show a pronounced increase with temperature, $\mathcal{P}_{\mathrm{eq}} = 0.68$, 0.81, and 0.91 for $\Delta\mathcal{T}/T_F = 0.026$, 0.052, and 0.078, respectively. We interpret this increase as a consequence of the decreasing superfluid core and thus the decreasing MOI quenching effect. For our highest temperature ($\Delta\mathcal{T}/T_F = 0.104$) we only observe a marginal further increase to $\mathcal{P}_{\mathrm{eq}} = 0.93$. This indicates that the superfluid core is very small or absent leading to a disappearance of the quenching effect. The fact that the maximum $\mathcal{P}_{\mathrm{eq}}$ stays a few percent below 1 can be explained by trap imperfections as discussed in Sec. 5.3.

Let us comment on the possible influence of vortices [Zwi05]. We cannot exclude their presence [7], as their nucleation can proceed not only via a resonant quadrupole mode excitation [Mad01, Hod02], but also via a coupling to the thermal cloud [Hal01b]. Vortices would result in additional angular momentum in the rotating cloud and its collective behavior would be closer to the normal case. This would tend to increase $\mathcal{P}$ at lower temperatures, counteracting the behavior that we observe.

[4] The ellipticity is kept at its full level while the rotation is turned off. To speed up the damping we increase the magnetic field to 920G.

[5] The temperature increase resulting from conversion of rotational energy into heat is neglibly small.

[6] The curves do not show the spin-up process directly, as our measurement procedure fixes the temperature at the time of the measurement of $\mathcal{P}$.

[7] In our setup we cannot directly observe vortices by absorption imaging. The main reason is the technical limitation that our coil system does not allow for fast enough magnetic field ramps as required for increasing the size of vortex cores during expansion [Zwi05].

5.4.2. Superfluid phase transition

In a second set of experiments, we study the superfluid phase transition in a way which is experimentally simpler, but which requires information on the equilibrium state as obtained from the measurements presented before. The trap rotation is applied continuously, and we observe the increase of $\mathcal{P}$ with the rotation time t_{rot}. All other parameters and procedures are essentially the same as in the measurements before. Here the temperature is not constant, but rises according to $\mathcal{T} = \mathcal{T}_0 + \alpha t_{\mathrm{rot}}$, where the heating rate $\alpha = 170\,\mathrm{nK/s}$ is the same as before and $\mathcal{T}_0 = 0.085 T_F$ is somewhat lower because of the less complex timing sequence.

Figure 5.3 shows how $\mathcal{P}$ increases with the rotation time t_{rot} (filled symbols); the upper scale shows the corresponding temperature $\mathcal{T}$. The observed increase of $\mathcal{P}$ generally results from both factors in Eq.(5.1), corresponding to the rising $\Omega/\Omega_{\mathrm{trap}}$ (spin-up dynamics) and the rising $\Theta/\Theta_{\mathrm{rig}}$ (decrease of the superfluid MOI quenching). Figure 5.3 also shows the values $\mathcal{P}_{\mathrm{eq}}$ as determined from Fig. 5.2 (crosses), for which we know that the spin-up of the normal component has established an equilibrium with $\Omega/\Omega_{\mathrm{trap}}$ being close to one. The comparison shows that already for $t_{\mathrm{rot}} = 0.4\,\mathrm{s}$ the data set obtained with the simpler procedure follows essentially the same behavior. The small quantitative difference that the crosses are slightly below the open symbols can be explained by a somewhat stronger influence of trap imperfections in the earlier measurements of Sec. 5.4.1 [8] or by the uncertainty in the initial temperature $\mathcal{T}_0$. For $t_{\mathrm{rot}} \geq 0.4\,\mathrm{s}$, we can assume that the system is in an equilibrium state, which follows the slowly increasing temperature, and we can fully attribute the further increase of $\mathcal{P}$ to the quenching of the MOI.

The superfluid phase transition corresponds to the point where the precession parameter $\mathcal{P}$ reaches its saturation value. This is observed for a time $t_{\mathrm{rot}} \approx 0.95\,\mathrm{s}$, when $\mathcal{T}/T_F \approx 0.21$. The conversion of this temperature parameter (measured in the weakly interacting regime after an isentropic change) to the actual temperature in the unitarity-limit regime [Luo09] yields a value for the critical temperature T_c of about $0.2\,T_F$. This result is consistent with previous experimental results [Reg04b, Luo07, Ina08b, Luo09, Hor10, Nas10b], the range of which is indicated by the shaded region in Fig. 5.3. The result is also consistent with theoretical predictions [Gio08, Hau08].

For a more precise extraction of T_c from experimental MOI quenching data, a theoretical model would be required that describes the saturation behavior of $\Theta/\Theta_{\mathrm{rig}}$ as T_c is approached. Theoretical predictions are available for the BEC limit [Str96] and the BCS limit [Far00, Urb03, Urb05]. In the unitarity limit it should, in principle, be possible to extract the MOI from spatial profiles of the normal and the superfluid fraction [Per04, Sta05]. Clearly, more work is necessary to quantitatively understand the quenching effect in the strongly interacting regime.

5.5. Conclusion

We have demonstrated the quenching of the moment of inertia that occurs in a slowly rotating, strongly interacting Fermi gas as a consequence of superfluidity. This effect provides us with a novel probe for the system as, in contrast to other common methods such as expansion measurements and studies of collective modes, it allows us to distinguish between the two possible origins of hydrodynamic behavior, namely collisions in a normal phase and superfluidity.

[8] This explanation is supported by the fact that we measured a slower decay of angular momentum for the later experiments of Fig. 5.3 ($\kappa = 0.90$) than we did for the earlier measurements of Fig. 5.2 ($\kappa = 0.85$). Between the two sets of measurements the optical setup of the trapping beam was readjusted, leading to reduced imperfections in the later experiments.

We thank L. Sidorenkov and M. K. Tey for discussions. We acknowledge support by the Austrian Science Fund (FWF) within SFB 15 (project part 21) and SFB 40 (project part 4).

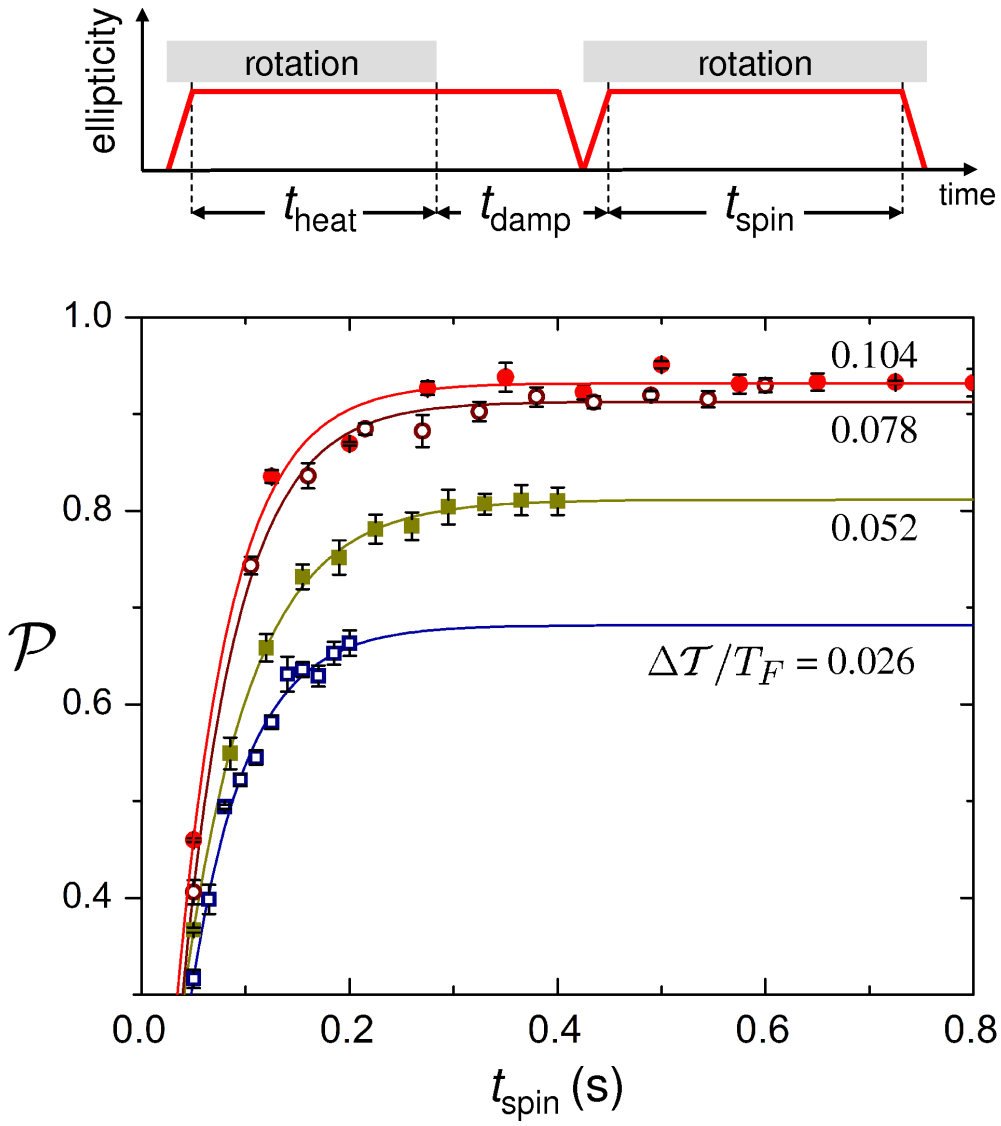

Figure 5.2.: Precession parameter $\mathcal{P}$ versus spin-up time t_{spin} for various values of the final temperature, as characterized by the heating parameter $\Delta\mathcal{T}$ (see text). The quenching of the MOI shows up in the temperature-dependent saturation behavior. The applied timing sequence to facilitate measurements at constant temperature is illustrated above the graph. For these sets of measurements $\kappa = 0.85$.

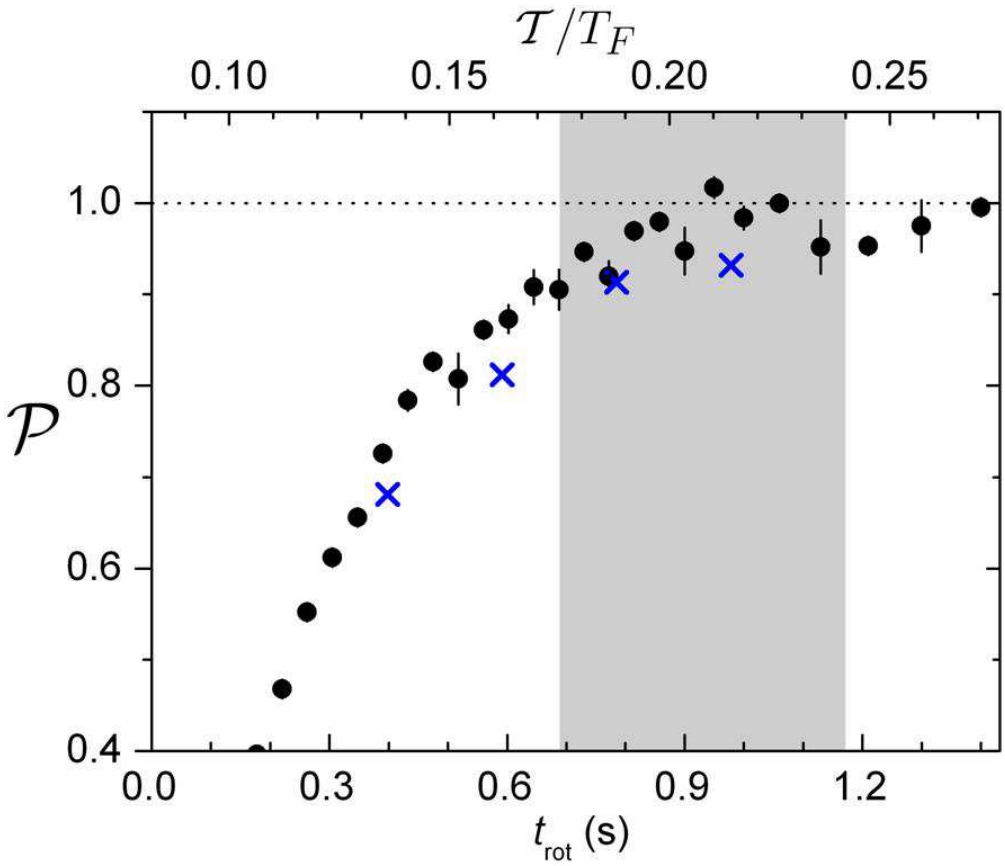

Figure 5.3.: The precession parameter $\mathcal{P}$ as a function of the rotation time t_{rot} (filled symbols); the upper scale shows the corresponding temperature $\mathcal{T}$. For comparison, the crosses show the equilibrium values $\mathcal{P}_{\mathrm{eq}}$ as obtained from Fig. 5.2. The shaded region indicates the range in which we expect the superfluid phase transition according to previous experiments [Reg04b, Luo07, Ina08b, Luo09, Nas10b, Hor10]. For this set of measurements $\kappa = 0.90$.

6. Publication: Observation of interference between two molecular Bose-Einstein condensates

New J. Phys. 13, 065027 (2011)

C. Kohstall,[1,2] S. Riedl,[1,2] E. R. Sánchez Guajardo*,[1,2] L. Sidorenkov,[1,2]
J. Hecker Denschlag,[1] and R. Grimm[1,2]

[1] *Institut für Experimentalphysik und Zentrum für Quantenphysik, Universität Innsbruck, 6020 Innsbruck, Austria*
[2] *Institut für Quantenoptik und Quanteninformation, Österreichische Akademie der Wissenschaften, 6020 Innsbruck, Austria*

We have observed interference between two Bose-Einstein condensates of weakly bound Feshbach molecules of fermionic ^{6}Li atoms. Two condensates are prepared in a double-well trap and, after release from this trap, overlap in expansion. We detect a clear interference pattern that unambiguously demonstrates the de Broglie wavelength of molecules. We verify that only the condensate fraction shows interference. For increasing interaction strength, the pattern vanishes because elastic collisions during overlap remove particles from the condensate wave function. For strong interaction the condensates do not penetrate each other as they collide hydrodynamically.

6.1. Introduction

Interference manifests the wave nature of matter. The concept of matter waves was proposed by de Broglie in 1923 [de 23] and now represents a cornerstone of quantum physics. Already in the 1920's, experiments demonstrated the diffraction of electrons [Dav27] and of atoms and molecules [Est30]. These early achievements led to the field of atom optics and interferometry [Ada94, Bon04, Cro09].

With the realization of Bose-Einstein condensates (BECs) [And95, Dav95, Bra95], sources of macroscopically coherent matter waves became available. The interference between two BECs was first observed by Andrews et al. [And97b]. This landmark experiment evidenced interference between two independent sources and revealed the relative phase between them [Cas97]. Since then, interference measurements have developed into an indispensable tool for research on BEC. Applications include detection of the phase of a condensate in expansion [Sim00], investigation of a condensate with vortices [Ino01], and studies of quasi-condensates [Had06] or Luttinger liquids [Hof07] in reduced dimensions. Another fundamental line of research in matter-wave optics is to explore the transition from the quantum to the classical world by detecting the wave nature of progressively larger particles, like clusters [Sch94], C_{60} [Arn99], and other giant molecules [Ger11].

*The contribution of the author of this thesis to this work was to take data and discuss the results for publication.

The creation of molecular Bose-Einstein condensates (mBECs) of paired fermionic atoms [Joc03a, Gre03, Zwi03] provides us with macroscopically coherent molecular matter waves. In this article, we present the interference of two such mBECs and demonstrate interference as a tool to investigate condensates of atom pairs. This work extends the interference of condensates towards larger, composite particles.

In a Young-type interference experiment, we release two mBECs from a double-well trap and, after the condensates have overlapped, we observe an interference pattern by absorption imaging. In Sec. 6.2, we describe the experimental procedures in detail. In Sec. 6.3, we present our main experimental results, demonstrating the *molecular* de Broglie wavelength and the dependence of the interference contrast on temperature and interaction strength. Increasing the interaction strength reduces the visibility because of increasing elastic scattering losses depleting the coherent matter wave. Section 6.4 gives an outlook to possible extensions and applications of interference of pair condensates.

6.2. Experimental procedures

6.2.1. Preparation of the molecular Bose-Einstein condensate

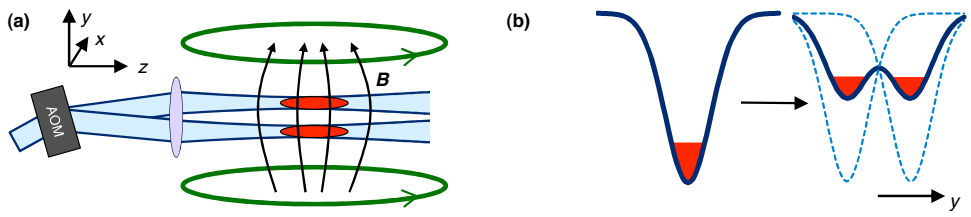

Figure 6.1.: Illustration of the trapping and splitting of the mBEC in the presence of a magnetic field B. An acousto-optical modulator (AOM) toggles the laser beam between two positions, which creates an effective double-well potential for trapping two mBECs. (a) Along the x- and y-directions, the optical potential is dominant; along the z-axis the magnetic potential is dominant. (b) The potential shape of the optical dipole trap is Gaussian. The double-well potential is generated from the superposition of two Gaussian potentials.

We create a molecular Bose-Einstein condensate (mBEC), starting from an atomic Fermi gas consisting of an equal mixture of ^{6}Li in the lowest two spin states. The preparation follows the procedures described in our previous work [Joc03a, Bar04b, Alt07a, Rie08].

The atoms are trapped in the potential of a focused, far red-detuned laser beam with a beam waist of 45 μm, derived from a 25 W, 1030 nm single-mode laser source, as illustrated in Fig. 6.1. We choose the coordinate system such that the laser beam propagates along the z-axis and gravity acts in $-y$-direction. A magnetic bias field B can be applied along the y-axis. A broad Feshbach resonance centered at $B = 834$ G [Bar05] facilitates precise tuning of the atomic s-wave scattering length a. Below resonance, a weakly bound molecular state exists [Joc03b]. Molecules in this state represent halo dimers, since their wave function extends far into the classically forbidden range

[Fer08]. Their size is given by a and their binding energy is $\hbar^2/(ma^2)$, where m denotes the atomic mass and $\hbar$ is Planck's constant h divided by 2π. The intermolecular scattering length is $a_M = 0.6a$ [Pet05b].

To create the mBEC we perform evaporative cooling by reducing the laser beam power at a constant magnetic field $B = 764\,\mathrm{G}$. During evaporation, the halo dimers are created through three-body collisions [Joc03a] and eventually they form a mBEC [Ing08]. After evaporation, we increase the trap depth, thereby compressing the condensate, to avoid spilling particles in all further stpdf of the experimental sequence. The beam power is adiabatically increased by a factor of about 10 to 45 mW. The trap center can be closely approximated by a harmonic potential. The oscillation frequencies of the molecules, which are the same as the ones of free atoms, are $(\omega_x, \omega_y, \omega_z) = 2\pi \times (250, 250, 20.6 \times \sqrt{B/700\,\mathrm{G}})\,\mathrm{Hz}$. The axial confinement essentially results from the curvature of the magnetic field. We obtain a cigar-shaped cloud containing $N = 1.8 \times 10^5$ molecules. The condensate fraction exceeds 90 % [Joc03a].

Most of our measurements are carried out in the regime of weak interaction between the molecules. We ramp the magnetic field adiabatically down to 700 G in 200 ms, thereby decreasing the scattering length to about $a_M = 1000\,\mathrm{a_0}$; at lower fields the molecules become unstable [Pet05a, Cub03, Joc03b] and limit the lifetime of the mBEC. At 700 G, the chemical potential of the mBEC is $k_B \times 200\,\mathrm{nK}$, with k_B denoting the Boltzmann constant, and the binding energy of the molecules is $k_B \times 8\,\mu\mathrm{K}$. In view of the crossover from BEC to a Bardeen-Cooper-Schrieffer (BCS) type regime [Gio08, Ing08], one can also express the interaction conditions in terms of the commonly used dimensionless parameter $1/(k_F a)$, where k_F is the Fermi wave number of a non-interacting Fermi gas with $(\hbar k_F)^2/(2m) = E_F$, where $E_F = \hbar(6N\omega_x\omega_y\omega_z)^{1/3}$ is the Fermi energy. For the condition of our mBEC at 700 G we obtain $1/(k_F a) = 3$. Strongly interacting conditions are realized for $1/(k_F a) < 1$, which can be achieved at fields closer to resonance.

6.2.2. Condensate splitting

The mBEC is split into two equal parts along the y-axis. We transform the Gaussian shaped optical dipole potential into a double-well potential, as illustrated in Fig. 6.1(b). This is accomplished by using time-averaged potentials. An acousto-optical deflection system modulates the trapping beam position so fast that the atoms do not follow and feel the time-averaged beam intensity as their motional potential [Alt07b, Shi04]. The modulation frequency is 200 kHz and the trapping beam is toggled between two positions, the distance of which is increased from 0 to 68 μm within 50 ms. The distance between the minima of the resulting double well is somewhat smaller because the two Gaussian potentials still overlap. The measured distance between the centers of the two condensates is $s = 56\,\mu\mathrm{m}$ and the measured oscillation frequencies in each well are $(\omega_x, \omega_y, \omega_z) = 2\pi \times (164, 146, 20.6 \times \sqrt{B/700\,\mathrm{G}})\,\mathrm{Hz}$. The chemical potential of both condensates is $k_B \times 100\,\mathrm{nK}$ and the interaction parameter is $1/(k_F a) = 4$. The barrier height is $k_B \times 160\,\mathrm{nK}$, which leads to a fully negligible tunneling rate. The number ratio between the two condensates after splitting is sensitive to imperfections of the optical potential. To control equal number splitting, we fine-tune the magnetic gradient field that is applied to compensate for the effect of gravity.

6.2.3. Expansion in the magnetic field

The specific expansion dynamics of the released mBECs in our setup is the key to making interference clearly observable, and the understanding of the expansion is essential for the interpretation

of our results. We identify two effects, which result from the curvature of the magnetic field, that are favorable for the observation of interference.

The coils generating the magnetic offset field in our set-up are not in Helmholtz configuration, which leads to second-order terms in $B(x, y, z)$. The resulting magnetic potential is a saddle potential, where the molecules are trapped along the x- and z-directions, but they are anti-trapped along the y-axis, the symmetry axis of the field. The oscillation frequencies are $(\omega_x, \omega_y, \omega_z) = 2\pi \times (20.5, i \times 29, 20.5) \times \sqrt{B/700\,\mathrm{G}}\,\mathrm{Hz}$, where the imaginary frequency denotes the anti-trap along the y-axis.

We model the expansion by adopting the scaling approach as applied in Refs. [Men02, Alt07b]. Figure 6.2(b) shows the predicted evolution of the Thomas-Fermi (TF) radii R_x, R_y and R_z, which we also verify experimentally. At the beginning, the expansion is driven by the pressure gradient in the cloud, which leads to a fast acceleration in the radial direction. This expansion is then further accelerated along y and decelerated along x because of the magnetic saddle potential. Along the z-axis, the long axis of the trapped cloud, the trap remains basically unchanged when the cloud is released from the optical potential. As the mean field pressure of the expanding cloud decreases, the magnetic confinement leads to a spatial compression of the cloud. We find that after $t_{\mathrm{TOF}} \approx 14\,\mathrm{ms}$ the parameter R_z has a minimum because of this compression effect.

For high interference contrast, large overlap of the two clouds at the time of detection is essential. To achieve this, the condensates are kicked towards each other by switching on the original single-well trap, typically for 0.1 ms right after release from the double well. The solid lines in Fig. 6.2(a) show the calculated center-of-mass motion of the clouds after the initial kick to assure large overlap at $t_{\mathrm{TOF}} \approx 14\,\mathrm{ms}$.

The interference pattern is determined by the relative velocity between the two condensates. The relative velocity v_{rel} at $y = 0$ and $t_{\mathrm{TOF}} = 14\,\mathrm{ms}$ can be directly deduced from the slopes of the solid lines in Fig. 6.2(a). This velocity is substantially smaller than it would be in free expansion without magnetic potential, where particles meeting at $y = 0$ and $t_{\mathrm{TOF}} = 14\,\mathrm{ms}$ would follow the dashed trajectories in Fig. 6.2(a). This deceleration of v_{rel} can be readily visualized by the condensates climbing up the potential hill resulting from the anti-trap in y-direction. This anti-trap also accelerates the expansion in y-direction, see R_y in Fig. 6.2(b). Remarkably, since the velocity field in each of the clouds stays linear, v_{rel} is independent of the position. More rigorously, we calculate v_{rel} using the scaling approach and taking into account the center-of-mass motion of the clouds.

Thus expansion dynamics brings about two favorable effects: First, the spatial compression along the z-axis facilitates clear detection of interference fringes by absorption imaging. Second, the decreased relative velocity leads to an increased fringe period. This means that the anti-trap acts as a magnifying glass for the interference fringes.

6.2.4. Detection and analysis of interference fringes

We detect the clouds by absorption imaging. Figure 6.3(a) shows a typical image of interference after 14 ms time of flight. The imaging beam propagates along the z-axis. It is overlapped with the trapping beam using dichroic mirrors. The imaging light pulse is on for 10 μs and its intensity is about the saturation intensity of ^{6}Li atoms. We state-selectively image the atoms in the second-to-lowest Zeeman state. Already the first photon scattering event is likely to dissociate the weakly bound molecule [Bar04b], followed by about 10 more photons scattered by the free atom.

From the absorption images, we determine the visibility and fringe period of the interference pattern. The column density is integrated along the x-direction over the region depicted in Fig. 6.3(a) [1] resulting in a one-dimensional density distribution D, shown in Fig. 6.3(b). The density distribution contains various kinds of noise (e.g. photon or atom shot noise, or camera readout noise), which may be misinterpreted as interference signal. Therefore we analyze the density distribution in Fourier space by considering the Fourier transformed density distribution $\mathcal{F}(D)$, see Fig. 6.3(c). Here all those types of noise are approximately white and show up as a constant offset, whereas, the signal of interference is monochromatic and shows up as a peak. This gives the possibility to subtract the average contribution of noise from the signal. We determine the visibility and fringe period by the custom fit function in Fourier space

$$f = \sqrt{|\mathcal{F}((a + b\ y + c\ y^2) \times (1 + v\ \sin(2\pi/d\ y + \phi)))|^2 + n^2}, \tag{6.1}$$

yielding the fringe period d, the visibility v, and the relative phase ϕ. The term $a+b\ y+c\ y^2$ account for the somewhat non-uniform density distribution. The white noise n is the offset in Fourier space. Since the phase between the signal and the noise is random, the corresponding contributions are added quadratically. The discrimination of the noise via this fitting routine is crucial when the visibility is low.

The largest observed visibility is about 30 %. We find that this upper limit can be essentially attributed to the finite resolution of our imaging system. We determine the modulation transfer function of the imaging system and it gives about 30 ± 10 % visibility for structures with period $d = 20\,\mu$m. Also other sources can contribute to a reduction of visibility, like a blurring because of a limited depth of focus or a tilt of the planes of constructive and destructive interference. The planes are in general somewhat tilted with respect to the line of sight, thereby obscuring the fringe pattern on the image. But these effects are suppressed by the spatial compression along the imaging axis caused by the magnetic saddle potential. This can be seen by comparing the compression of R_z in Fig. 6.2(b) to the detected visibility in Fig. 6.2(c). The minimum of R_z after $t_{\mathrm{TOF}} = 14$ ms coincides with the peak in visibility. The peak value of almost 30 % agrees with the resolution limit of the imaging system. All following measurements are performed when the clouds are compressed to about $1\,\mu$m along the imaging axis; in this case, only the limited resolution is relevant. The spatial compression is an alternative to the slicing imaging technique used in Ref. [And97b] and brings along the advantage that all particles are imaged.

6.3. Experimental results

The observed interference pattern is the standing wave formed by two macroscopically occupied matter waves, the two molecular BECs. Here we present our main experimental results. In Sec. 6.3.1, we investigate the fringe period, which evidences that the interfering particles are molecules. In Sec. 6.3.2, we study the visibility when heating the cloud to above the critical temperature for condensation to show that the interference is established by the condensate fraction. In Sec. 6.3.3, we explore the dependence of the visibility on the interaction strength and find that non-forward scattering processes depopulate the momentum component of the matter wave that is responsible for the interference pattern.

[1] The size of the region was chosen to produce the optimal signal to noise.

6.3.1. Fringe period

The fringe period is an central observable in interference experiments. Figure 6.4 shows the measured fringe period at $B = 700\,\mathrm{G}$ as a function of time of flight. The de Broglie relation yields the fringe period

$$d = \frac{h}{M v_{\mathrm{rel}}}, \tag{6.2}$$

which is determined by the mass M of the interfering particles and by the relative velocity v_{rel} of the two condensates. In our experiment, we calculate v_{rel} from the expansion and center-of-mass motion of the condensates in the magnetic field curvature, as discussed in Sec. 6.2.3. The result is in contrast to the simple relation $v_{\mathrm{rel}} = s/t_{\mathrm{TOF}}$ that holds for the free expansion usually considered in experiments of this type. The solid line in Fig. 6.4 displays the calculated fringe period d for molecules, where we set $M = 2m$. All input parameters for this calculation are determined independently. Their combined uncertainties result in typical uncertainty of 3 % for the fringe period, with the main contribution stemming from the uncertainty in the cloud separation. The data are in remarkable agreement with the calculation. For comparison, we also plot the fringe period for interfering atoms ($M = m$), which is clearly incompatible with the data.

The dotted line in Fig. 6.4 displays the fringe period that would result for freely expanding mBECs without the magnetic saddle potential. Comparing this curve to the much larger fringe period that we observe, highlights the effect of the magnetic field curvature to magnify the fringe period, as discussed in Sec. 6.2.3. The same magnification effect was reported in Ref. [Zaw10].

Note that the fringe period can be increased by interaction-induced slowing down of the two overlapping condensates [Sim00]. The mean-field of one condensate represents a potential hill for the other condensate, which slows down when climbing this hill. Under our experimental conditions at 700 G, the effect is found to be negligible. For stronger interaction, we see indications of this effect in agreement with a corresponding model calculations.

6.3.2. Dependence of interference visibility on condensate fraction

To demonstrate that the interference results only from the condensed molecules and not from the thermal fraction, we perform a controlled heating experiment and show the loss of visibility with vanishing condensate fraction. Starting from an almost pure condensate [Joc03a], we hold the gas in the recompressed optical dipole trap for a variable hold time before splitting. Intensity fluctuations and pointing instabilities of the laser beam as well as inelastic collisions between the molecules [Pet05a] heat the gas and lead to a monotonous temperature increase [Sav97, Wri07]. To demonstrate that the interference results from the condensate, it is sufficient to determine the hold time at which the critical temperature for condensation T_c is reached. Therefore, we fit a Gaussian profile to the density distribution of the cloud, which is recorded after expansion for $t_{\mathrm{TOF}} = 5\,\mathrm{ms}$ from the single-well trap. We find that the integrated residual of the fit gives a good measure whether the cloud shape deviates from a thermal one. The inset in Fig. 6.5 shows that the integrated residual goes to zero after a hold time slightly below 3 s, which locates the phase transition.

The visibility data in Fig. 6.5 are recorded at $B = 700\,\mathrm{G}$ after $t_{\mathrm{TOF}} = 14\,\mathrm{ms}$ [2]. The visibility decreases as the temperature increases and vanishes for a hold time that coincides with the hold

[2] We verify on images after $t_{\mathrm{TOF}} = 0.4\,\mathrm{ms}$ that the clouds are still separated in the double-well potential despite the higher thermal energies.

time when T_c is reached. The observed decrease of visibility is continuous because we image the full column density including the growing thermal fraction, which does not clearly separate from the condensate in expansion at 700 G. Above T_c, the density distribution does no more show any fringes. Still, the fitting routine produces finite mean values because it can output only positive values. But if the measured visibility is not larger than the standard deviation, its distinction from zero is not significant. The vanishing visibility above the critical temperature confirms that, as expected, the interference is established by the condensate fraction.

Further intriguing evidence that the interference is caused by the condensate is the observation of interference between independent ultracold clouds. An independent production rules out that the interference can be caused by self interference of particles [Mil05]. To investigate interference between independent clouds, we split them already at a temperature far above the critical temperature to a large distance of 180 μm and then create two mBECs independently. Shortly before release, we reduce the distance to obtain the identical geometry as in all the other measurements and proceed as usual. We observe the same kind of interference pattern with a visibility of about 15 %. The lower visibility can be explained by a less efficient evaporation and less control over the equal number preparation in the double well.

6.3.3. Dependence of interference visibility on interaction strength

In a further set of measurements, we investigate how the fringe visibility depends on the interaction strength. Therefore we perform the interference experiment for different magnetic field values, thereby changing the molecular scattering length a_M according to the upper panel of Fig. 6.6 [3]. The observed visibility as a function of the magnetic field is shown in the lower panel in Fig. 6.6. The highest visibility is found at about 700 G. For lower fields, the visibility is decreased, which we attribute to inelastic decay. The inelastic collisions of molecules lead to heating of the gas and loss of particles. The heating reduces the condensate fraction, which decreases the visibility as observed in the previous section. The loss also reduces the signal on the images. This leads to a higher statistical uncertainty in the determination of the visibility, showing up in the larger standard deviations below 700 G.

Towards larger interaction strength, our data show a pronounced decrease of visibility, and the visibility vanishes at about 780 G. This coincides with the onset of strong interaction in the trap, where $1/k_F a \approx 1$. We find that the main effect causing the decrease is elastic non-forward scattering. It is known from experimental and theoretical work on colliding condensates [Chi00, Ban00] that elastic non-forward scattering of particles removes them from the condensate wave function. In contrast to the forward scattering accounted for within the usual mean-field approach, this non-forward scattering transfers particles into momentum states of random direction, which therefore do no more contribute to the observed interference pattern. Non-forward scattering is a particle-like excitation, which requires v_{rel} to exceed the speed of sound v_s. The process is suppressed for smaller v_{rel} [Chi00, Ban01]. To estimate the decrease of visibility through this process, we perform a simple model calculation. The velocity dependence of non-forward scattering is included by the following approximation: no suppression for $v_{\mathrm{rel}} \geq v_s$ and full suppression otherwise. We calculate the mean number of non-forward scattering events N_e for a representative molecule with molecules of the other condensate until the moment of detection. This representative

[3] We verify on images after $t_{\mathrm{TOF}} = 0.4$ ms that the clouds are still separated in the double-well potential despite the higher chemical potential at higher interaction strength.

molecule travels along the center-of-mass path of the condensate; see Fig. 6.2(a). We take the bosonically enhanced, unitarity limited scattering cross section $\sigma = 8\pi a_M^2/(1 + (ka_M)^2)$, with $k = mv_{\mathrm{rel}}/\hbar$. From N_e, we derive the probability for a molecule to still be part of the condensate. This probability is e^{-N_e} and directly corresponds to the expected visibility, which we fit to the data, excluding the three data points below 700 G. We obtain the solid line in Fig. 6.6. The only fit parameter is a normalization factor, which allows us to account for the reduced detected visibility because of the limited imaging resolution. The fit yields a factor of 0.32, which is consistent with the imaging resolution discussed in Sec. 6.2.4. We find that our simple model for non-forward scattering can very well explain the decrease of visibility towards high interaction strength.

There are also other effects that decrease the visibility for increasing interaction strength, but they turn out to be minor for our experimental conditions: Strong interaction lead to a depletion of the condensate [Dal99]. Only the condensate contributes to the interference pattern and not the depleted fraction.The depleted fraction amounts to about 10 % at 780 G. As we expect the reduction of visibility to be proportional to the depletion, the reduction is negligible (at 780 G from 2.6 % to 2.3 %). Another effect reducing the visibility is the collisional dissociation of molecules during overlap. However, this effect can only occur above 800 G, where the collision energy exceeds the binding energy.

To directly demonstrate the effect of non-forward scattering, we study the collision of two condensates when their relative velocity v_{rel} is much faster than the their expansion velocity. This allows us to observe the non-forward scattered particles in an s-wave shell [Bug04], well separated from the condensates, see Figure 6.7. This separation was not present in the interference experiments reported before because v_{rel} was similar to the expansion velocity. We apply our simple model to calculate the fraction of non-forward scattered particles and find good agreement, confirming our model in an independent and direct way.

Close to the Feshbach resonance, we enter a regime where the number of collisions becomes large. This leads to hydrodynamic behavior also above T_c [O'H02a, Wri07]. The time of flight series in Fig. 6.8, taken on resonance, shows that the clouds do not penetrate each other in this regime. Instead, the flow of the particles is redirected into the the x-z-plane leading to the observed high column density in the center. Unlike at low magnetic fields, the clouds do not superimpose. This directly excludes interference of two independent condensates in the strongly interacting regime. The scenario is similar to the one in Ref. [Jos04] and may be described by the analysis therein.

The hindered overlap could be overcome by a magnetic field ramp to weak interaction after release and before overlapping, as done for the detection of vortices in Ref. [Zwi05]. Like the observation of vortices, the observation of interference would evidence the coherence of the strongly interacting superfluids.

In further measurements, performed above the Feshbach resonance towards the BCS regime, we did not observe interference. To discuss possible reasons for the absence of interference fringes, let us first consider the effect of non-forward scattering on the visibility. As on the BEC side, this effect may hinder overlap and interference for $1/k_F a < -1$, i.e. below 910 G. However, we also have to consider that the pairs on the BCS side may not persist in expansion [Sch07b], unlike on resonance or on the BEC side. For the lowest achievable temperature in our experiment and at 910 G, the pairs would be already unstable after a very short expansion time according to Ref. [Sch07b].

6.4. Conclusion and outlook

In conclusion, we have observed the interference between two molecular BECs. The interference pattern visualizes the standing matter wave of the weakly bound Feshbach molecules and shows coherence over the spatial extension of the cloud. The contrast of interference vanishes above the critical temperature of condensation, demonstrating that the interference is established by the condensed molecules only. We find that non-forward elastic scattering processes can lead to a depletion of the condensate wave function while the clouds overlap. This effect increases towards higher interaction strength and prevents us from observing interference in the strongly interacting regime. On resonance we observe that the two clouds do not overlap but rather collide and deform as a result of deep hydrodynamic behavior.

Interference between condensates of paired fermionic atoms can serve as a powerful tool to investigate many exciting aspects of those systems. A future application will be given, for example, if p-wave condensates become available. Here, interference is predicted to reveal the vector nature of the order parameter [Zha07]. A conceptually interesting regime will be entered when the size of the pairs becomes comparable to the fringe period. Then the detected distribution of atoms may not reveal the interference pattern of the pair distribution. Besides investigating condensates of paired fermions themselves, the system could be used to study the fundamental processes of interference. The wide tunability of the interaction strength could be used to assist self-interference [Ced07] or to investigate to which extent interaction build up the observable relative phase [Xio06].

Suppressing the effect of non-forward scattering during overlap could extend the range of applications of condensate interference. Such a suppression may be achieved by reducing the interaction strength before overlap using fast magnetic field ramping techniques [Gre03, Zwi05]. This technique would allow for investigating the interference in the regime of strong interaction or even on the BCS side of the resonance, where the interference of Cooper-type pairs is an intriguing question in itself.

We thank Christopher Gaul for stimulating discussions. We acknowledge support by the Austrian Science Fund (FWF) within SFB 15 (project part 21) and SFB 40 (project part 4).

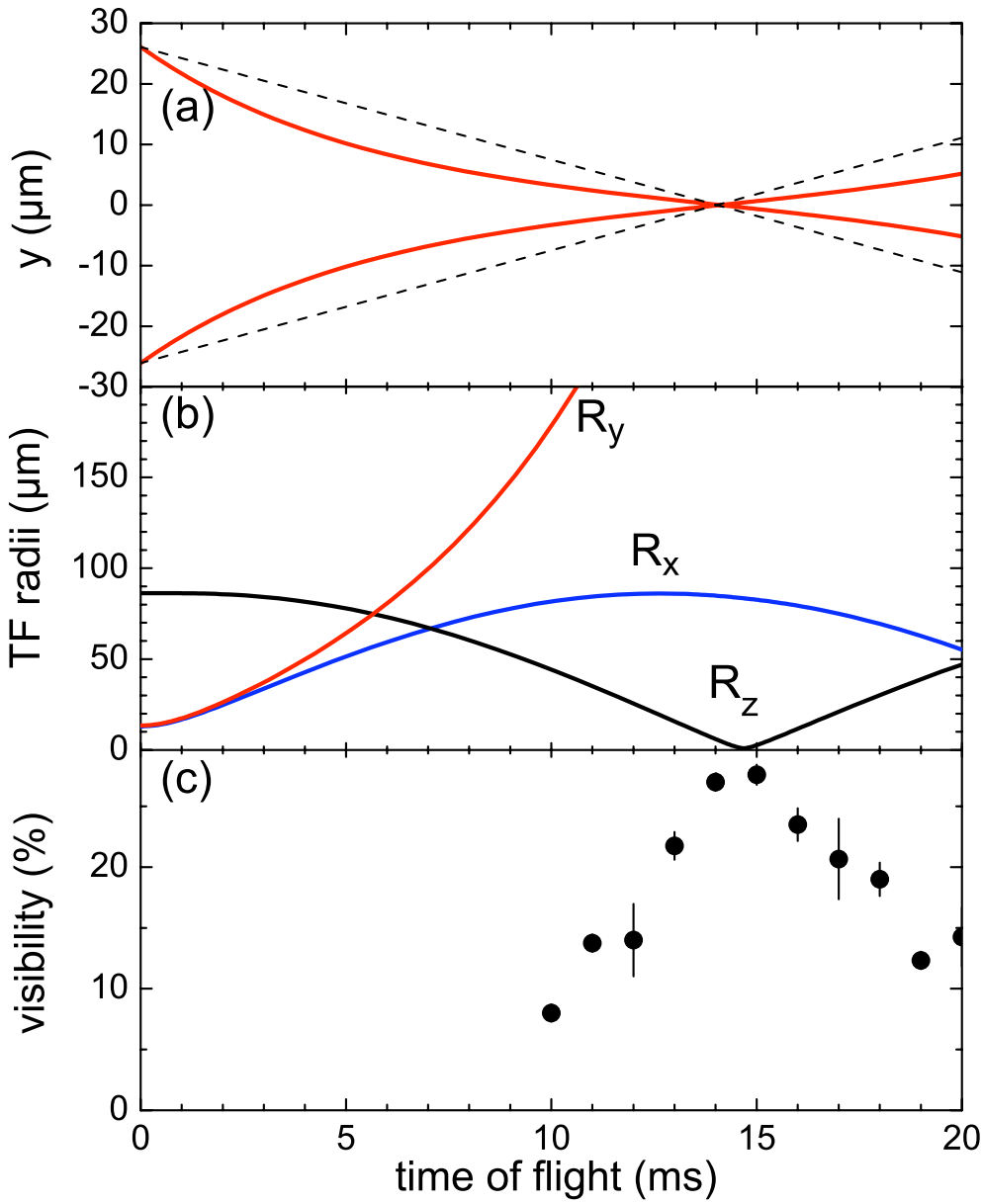

Figure 6.2.: Expansion dynamics of the condensates in the magnetic saddle potential. (a) The solid lines are the calculated center-of-mass motion of the condensates, taking into account an initial kick towards each other, see text. The trajectories intersect after $t_{\mathrm{TOF}} = 14\,\mathrm{ms}$. For comparison, the dashed lines represent the trajectories of particles in free expansion intersecting at the same point. (b) The calculated Thomas-Fermi radii of the condensates show the expansion along the x- and y-axis and the compression along the z-axis. The initially cigar-shaped mBEC evolves into a flat disc. (c) The measured visibility of the fringe pattern shows a clear peak, which coincides with the minimum in R_z. The bars indicate the statistical uncertainties derived from 10 individual measurements.

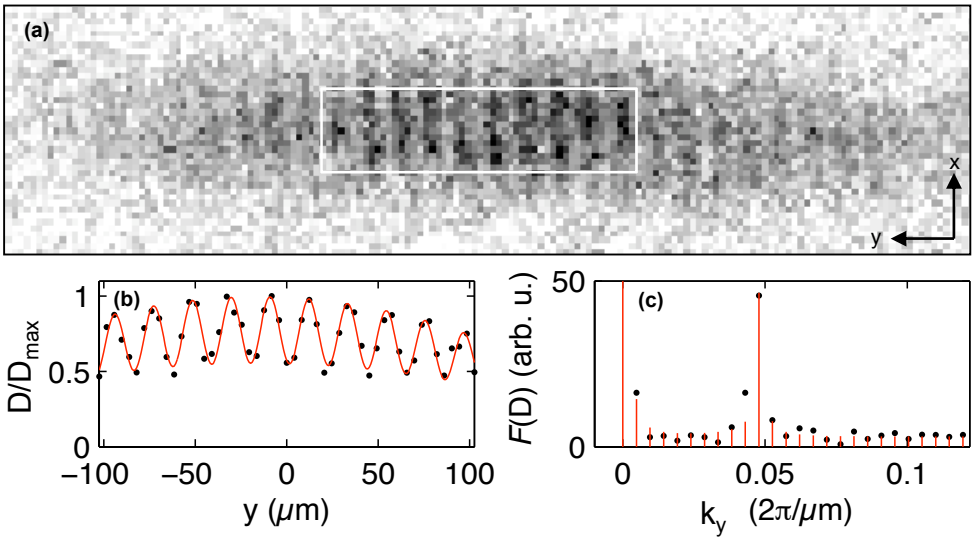

Figure 6.3.: Interference image and analysis. (a) The column density along the z-axis after $t_{\mathrm{TOF}} = 14\,\mathrm{ms}$ shows the interference pattern. The field-of-view is $660\,\mu\mathrm{m}\times170\,\mu\mathrm{m}$. The inner box indicates the region used for analysis. (b) The column density integrated along x gives the density distribution D along y (dots). The solid curve is the result of the fit in Fourier space, see text. (c) The density distribution is Fourier transformed (dots) and fitted (bars).

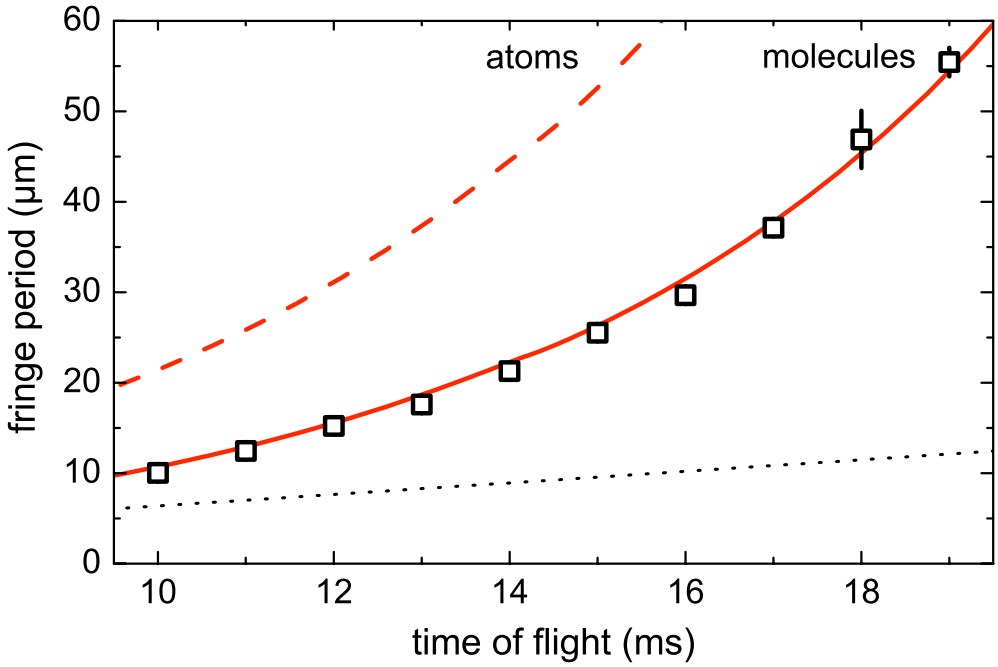

Figure 6.4.: Fringe period as a function of time of flight. The symbols are the measured periods with bars, mostly smaller than the symbol size, indicating the statistical uncertainties resulting from 10 individual measurements at a given time of flight. The solid line is the calculated period for molecules and the dashed line for atoms. For free expansion without the magnetic saddle potential, the fringe period of molecules would be much smaller (dotted line).

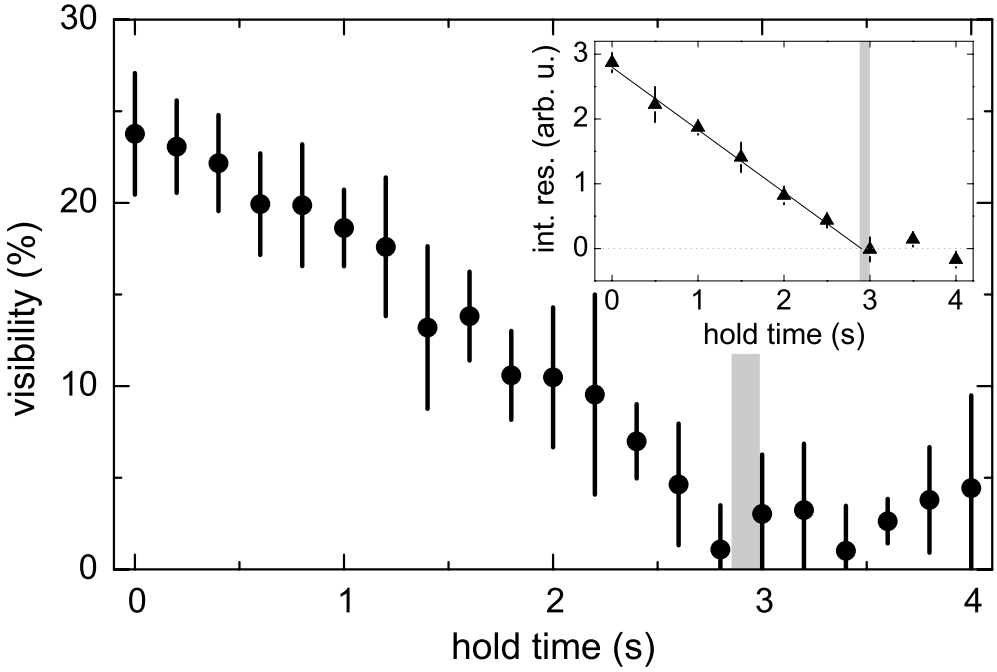

Figure 6.5.: Visibility of interference for increasing temperature. The main figure shows the measured mean visibility with bars indicating the standard deviation resulting from 11 measurements. Here, we plot the standard deviation and not the statistical uncertainty to better illustrate the range of measured values. During the hold time in the trap, the temperature increases from low temperature to above T_c. The hold time after which T_c is reached is indicated by the grey bar. The inset shows the integrated residuals of a Gaussian fit, see text. A linear fit to the first six points facilitates a simple extrapolation to zero, which marks the vanishing of the condensate fraction.

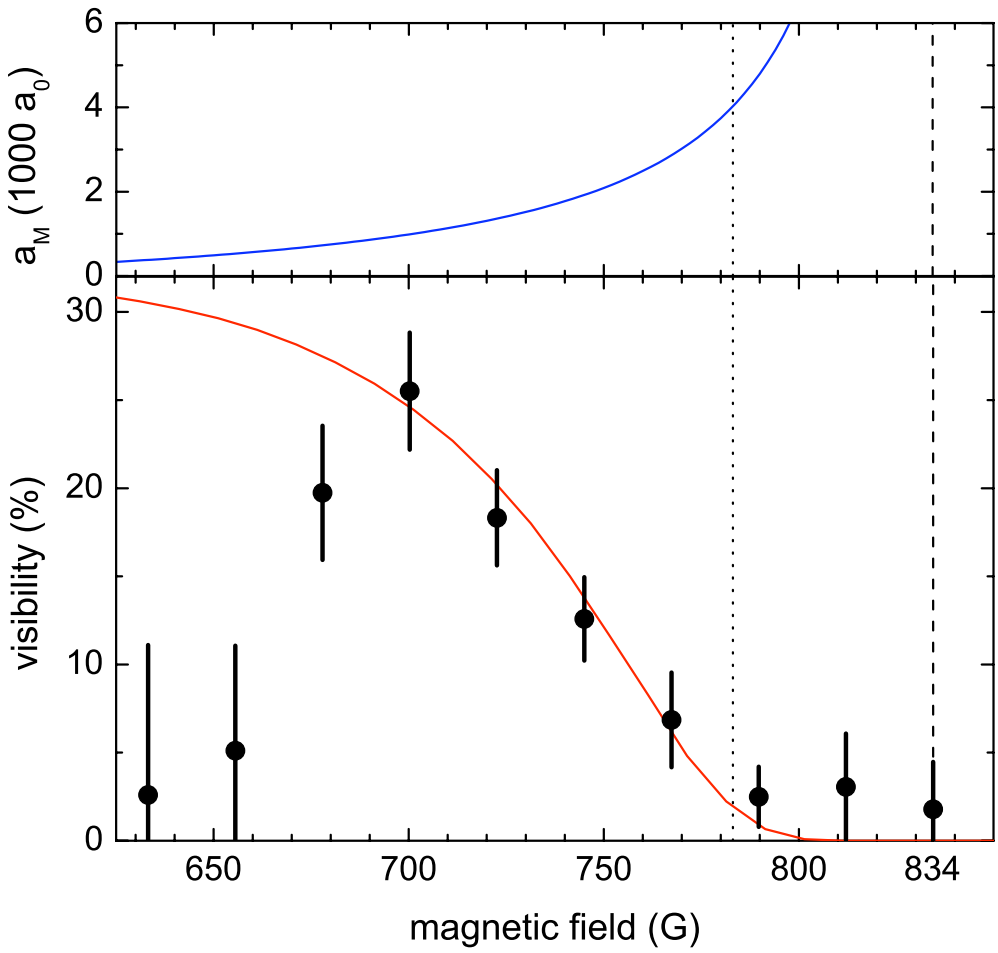

Figure 6.6.: Visibility of interference from weak to strong interaction. The upper panel shows how the molecular scattering length a_M increases towards the Feshbach resonance at 834 G, marked by the dashed line. The onset of the strongly interacting regime is marked by the dotted line. In the lower panel, the dots represent the mean visibility with bars indicating the standard deviation resulting from 20 individual measurements. The solid line is the predicted visibility from the simple calculation modeling the non-forward scattering events.

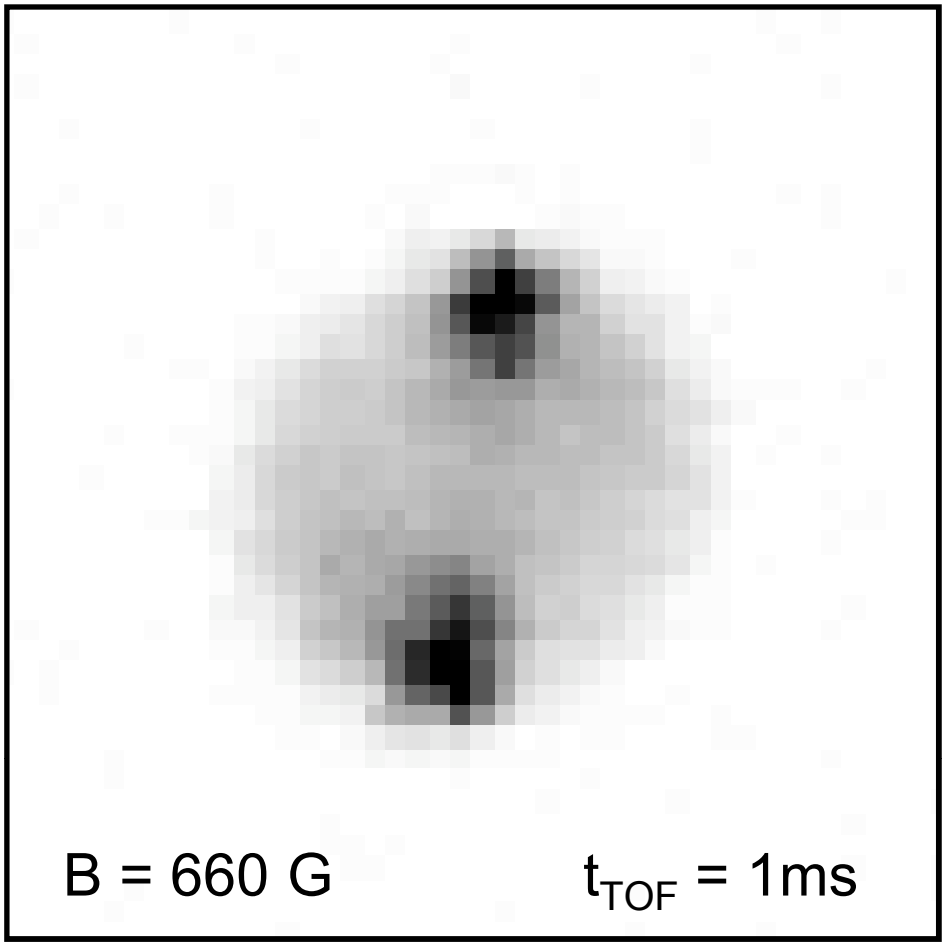

Figure 6.7.: Absorption image 1 ms after the collision of two BECs. A spherical shell of scattered particles clearly separates from the two BECs. The field of view is $180 \times 180\,\mu$m.

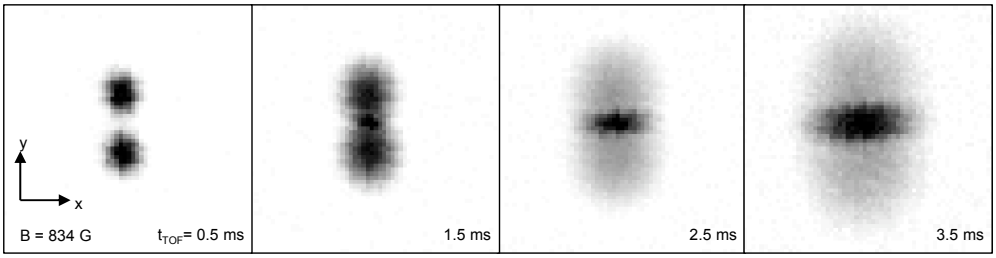

Figure 6.8.: The hindered overlap on resonance. The series shows the first few milliseconds of expansion. The two clouds do not penetrate each other, but splash according to hydrodynamics. The field of view is $180 \times 180\,\mu$m.

7. Higher order collective modes

In this chapter we investigate higher order collective modes in a Fermi gas composed of the two lowest hyperfine states of ^{6}Li with unitarity limited interactions*. The experiments are done in the zero-temperature limit. Higher order modes, besides being interesting in their own right, have been proposed as a tool to study second sound in ultracold trapped atoms.

Second sound takes place in a system where two coexisting and coupled fluids, one of them a superfluid, oscillate with respect to each other. The oscillation can be in-phase, known as *first sound,* or out-of-phase, referred to as *second sound*. One key point is that both fluids have to be hydrodynamic in order to ensure *local* thermal equilibrium. Thus, the normal fluid is collisional hydrodynamic, while the superfluid quantum hydrodynamic. Note that the fact that the equilibrium is local implies that the thermodynamic variables depend on both position and time. Another basic feature is the superfluid: it introduces a degree of freedom, the entropy, that reflects the fact that the quantum fluid has no entropy. Hence, the entropy fluctuations are a local depletion of the superfluid that indeed adds up to an out-of-phase oscillation of the densities.

The unitarity limited degenerate Fermi gas is produced in a single focused laser beam dipole trap. This results in an elongated cigar-shape trap geometry. In order to experimentally study higher order modes we modify our set up in two ways (see App. A): we introduce a far blue-detuned laser beam (532 nm) perpendicular to our single focused-laser dipole trap, and we implement a camera to image the axial distribution of the cloud. We excite the axial modes by modulating the height of the repulsive potential created by the blue-detuned beam. Along this direction both normal and superfluid components are deeply hydrodynamic. In addition, the larger size of the cloud makes it experimentally easier to engineer the perturbing potential and excite the cloud.

We first give a brief historical review of two-fluid hydrodynamics in section 7.1; in section 7.2 we discuss the general theoretical framework; the experiment is presented in section 7.3; then we discuss the analytical methodology in section 7.4; finally we discuss the results in section 7.5 before arriving at the conclusions in section 7.6.

7.1. Brief historical recollection

Two-fluid hydrodynamics was first discussed in 1938 in the context of superfluid helium [Tis38, Tis40a, Tis40b]. The theory was put forth shortly after in [Lan41]. Experimentally, the prediction that an entropy wave should arise in the system was confirmed using liquid helium II in [Pes44], which is also when the term "second sound" was coined. The speed of an entropy wave was measured soon after [Lan47].

*The author of the present thesis developed the experimental procedure, performed the measurements and made the data analysis. He was supported by M.K. Tey and L. Sidorenkov. F. Schreck and R. Grimm contributed ideas and suggestions. Theoretical support was given by Sandro Stringari.

The first studies in ultracold atoms were focused on weakly interacting Bose gases. From the theoretical side, the first calculations of first and second sound oscillations were done by Zaremba, Griffin, and Nikuni (ZGN) [Zar98] and by Shenon and Ho [She98]. Experimentally, the hydrodynamic condition introduced in Ch. 1, $\omega\tau_{\mathrm{R}} \ll 1$, is generally difficult to fulfill in a BEC: either the gas is too dilute or the scattering length too small in order to avoided losses. The first attempt to see traces of the entropy wave dates back to 1997 [And97a, And98], followed by a direct study the year after [Sta98]. This last experiment was eventually proven to have been carried out under conditions where the the two-fluid model holds [Nik01]. The experiment consisted in heating up the cloud locally with near-resonant light. A decade later it has been tried to see the effect in a BEC of Na were the hydrodynamic condition was achieved due to a very large number of atoms, and large axial trap frequency [Mep09a]. In this experiment sound propagation was studied using a repulsive barrier to excite the cloud. However, the required accuracy was not achieved to measure the expected behavior.

In a Fermi gas, where the Pauli exclusion principle suppresses losses, the hydrodynamic condition is fulfilled by adjusting the tunable interaction strength in the vicinity of a Feshbach resonance to result in a very small τ_{R}. This is a huge advantage from the experimental point of view. In the case of a trapped Fermi gas research on collective modes has been done extensively for the zero-temperature limit [Str04, Hei04, Kim04b, Kim04c, Hu04, Bul05, Man05, Ast05], and for the nondegenerate case [Bru99, Ped03, Mas05]. In the former limiting case one is dealing with a pure condensate described by *quantum hydrodynamics* [Pit98], and in the latter with a normal Fermi liquid described by *collisional hydrodynamics*.

The temperature region in between, where two-fluids hydrodynamics takes place, has also been studied for Fermi systems. It has been shown theoretically that the normal state of the unitarity limited gas is properly described by collisional hydrodynamics throughout the experimentally accessible temperatures [Mas05]. An initial study of first and second sound in these systems is found in [Ho04]. One recent model in particular uses a variational approach similar to that of ZGN to study the collective modes in an isotropic trap. The theoretical framework developed in [Tay05] circumvents the difficulty of solving the Landau equations for the normal modes. This is achieved by introducing displacement fields for the velocities instead of using Lagrange multipliers to minimize the action: the linearized conservation equations are rewritten as constraints for the fluctuations of the total density and the entropy, and expressed in terms of these displacement fields. Now one incorporates these constraints into the Taylor-expanded action and drops the Lagrange multipliers. The result is that the original action, which depended on the velocity and density fields of the normal and superfluid states, the entropy, and the Lagrange multipliers, is now a function of the displacement fields for the normal and superfluid state only. The task becomes to minimize the simplified action with respect to these new fields in order to find the *linearized* Landau two-fluid equations. One ends up with two coupled harmonic oscillators. Using the appropriate *Ansätze* for the displacement fields leads to the collective mode frequency.

This methodology was later used to calculate the temperature dependence of the low-lying collective modes [Tay08]. Together with numerical results for the dipole and breathing modes it was also suggested that Bragg spectroscopy could be a possible route to experimentally measure second sound. In subsequent research the hybridization of the higher order adiabatic waves with the entropy waves, which had already been predicted in [He07], was derived. This led to the conclusion that the coupling between adiabatic and entropy waves gives rise to a signature of the latter in the experimentally accessible absorption imaging of the former [Tay09]. The comparison between both

approaches is discussed in [Hu10].

On a separate research, the propagation of first and second sound pulses at finite temperature has been studied for the uniform case [Ara09], and predicted that second sound should have a sizable amplitude in the density response function which is separated from that of first sound. Just recently first studies on density and entropy waves propagating in the experimentally feasible elongated trap geometry were done [Ber10]. In it the conditions for hydrodynamic behavior in the 1D case were discussed.

Experimentally, neither higher order modes nor second sound have been studied in ultracold degenerate two-component Fermi gases. Yet it is exactly the Landau two-fluid equations and its ramifications which are appropriate to describe this region. In other words, the predictions of two-fluid hydrodynamics at unitarity are what distinguishes it from the weakly interacting superfluid, and pertain exclusively to strongly correlated quantum fluids. This is the motivation for our present line of work.

7.2. Concise theoretical background

The experimental results presented in this chapter relate to the zero-temperature limit of the theory. In this case exact solutions to the two-fluid hydrodynamic equations for the collective modes on resonance can be found. Be that as it may, for completeness and bearing in mind the larger scope and outlook of the project, we give a description of the variational method that generally describes the zero-temperature limit, the nondegenerate case, and the temperature region in between. However, it would be futile to attempt to explain in its full breadth the theoretical framework. Hence, we refer the reader to the references below, and content ourself here with a general sketch of the theory. All the models start from the dissipationless Landau two-fluid equations in a trap [Lan41, Tay05, Gri09, Tay09]:

$$\begin{aligned} \frac{\partial \rho}{\partial t} + \nabla \cdot \mathbf{j} &= 0, \\ \frac{\partial s}{\partial t} + \nabla \cdot (s\mathbf{v}_n) &= 0, \end{aligned} \tag{7.1}$$

and

$$\begin{aligned} m\frac{\partial \mathbf{v}_s}{\partial t} &= -\nabla\left(\mu + V_{\text{ext}}\right), \\ \frac{\partial \mathbf{j}}{\partial t} &= -\nabla P - n\nabla V_{\text{ext}}. \end{aligned} \tag{7.2}$$

Eqs. (7.1) are the conservation of mass and of entropy correspondingly; $\mathbf{j} = \rho_s\mathbf{v}_s + \rho_n\mathbf{v}_n$ is the total mass current, $\mathbf{v}_s$ and $\mathbf{v}_n$ the superfluid and normal fluid velocities, ρ_s and ρ_n the superfluid and normal fluid densities, and $\rho = \rho_s + \rho_n$ the total mass density. The second set of equations, Eqs. (7.2), are Euler's equations for irrotational flow; s is the entropy density, P is the local pressure of the gas, μ is the local chemical potential, and V_{ext} is the external trapping potential.

In addition, one needs to define an action, $S[s, \rho, \rho_n, \mathbf{v}_s, \mathbf{v}_n]$. The phenomenological action proposed in [Zil50] is expanded in powers of the fluctuations $(\delta\rho, \delta s, \delta\mathbf{v}_s, \delta\mathbf{v}_n)$ about the equilibrium values $(\rho_{s0}, s_0, \mathbf{v}_{s0}, \mathbf{v}_{n0})$ up to quadratic order [Tay08] (linear terms drop out during the variation process and higher order terms are disregarded). This action, $S^{(2)}$, describes the hydrodynamic

fluctuations, and still contains Lagrange multipliers. The traditional procedure would be to minimize the variation of the action with respect to the fluctuations. What is done instead is linearize Eqs. (7.1) and (7.2),

$$\begin{aligned} \frac{\partial \delta\rho}{\partial t} + \nabla\cdot(\rho_{s0}\mathbf{v}_s + \rho_{n0}\mathbf{v}_n) &= 0 \\ \frac{\partial \delta s}{\partial t} + \nabla\cdot(s_0\mathbf{v}_n) &= 0, \end{aligned} \tag{7.3}$$

and introduce the displacement fields

$$\mathbf{v}_n \equiv \frac{\partial \mathbf{u}_n(\mathbf{r},t)}{dt}, \text{ and } \mathbf{v}_s \equiv \frac{\partial \mathbf{u}_s(\mathbf{r},t)}{dt}. \tag{7.4}$$

The resulting constraint expressions $\delta\rho$ and δs are substituted into $S^{(2)}$,

$$\begin{aligned} S^{(2)} = \int d\mathbf{r}dt \Bigg\{ & \frac{1}{2}\rho_{s0}\dot{\mathbf{u}}_s^2 + \frac{1}{2}\rho_{n0}\dot{\mathbf{u}}_n^2 \\ & -\frac{1}{2}\left(\frac{\partial\mu}{\partial\rho}\right)_s [\nabla\cdot(\rho_{s0}\mathbf{u}_s + \rho_{n0}\mathbf{u}_n)]^2 \\ & -\left(\frac{\partial T}{\partial\rho}\right)_s [\nabla\cdot(s_0\mathbf{u}_n)]\,[\nabla\cdot(\rho_{s0}\mathbf{u}_s + \rho_{n0}\mathbf{u}_n)] \\ & -\frac{1}{2}\left(\frac{\partial T}{\partial s}\right)_\rho [\nabla\cdot(s_0\mathbf{u}_n)]^2 \Bigg\}. \end{aligned} \tag{7.5}$$

This results in an action that *only* depends on the two displacement fields, $\mathbf{u}_s(\mathbf{r},t)$ and $\mathbf{u}_n(\mathbf{r},t)$. This is the central part of the model.

We would like to find now the variational solutions with respect to these new fields. By choosing *Ansätze* of the form

$$u_{si}(\mathbf{r},t) = a_{si} f_i(\mathbf{r}) \cos\omega t \tag{7.6a}$$

and

$$u_{ni}(\mathbf{r},t) = a_{ni} g_i(\mathbf{r}) \cos\omega t, \tag{7.6b}$$

where i corresponds to each Cartesian direction, the minimization of the action becomes

$$\frac{\partial S^{(2)}}{\partial a_{si}} = 0 \text{ and } \frac{\partial S^{(2)}}{\partial a_{ni}} = 0. \tag{7.7}$$

Hence, what remains is to find suitable trial functions $f_i(\mathbf{r})$ and $g_i(\mathbf{r})$ to produce the appropriate collective mode frequency or, in the case of a uniform gas, the speed of first and second sound.

At this point it is convenient to substitute Eqs. (7.6) into $S^{(2)}$. Performing the time integration one finds the following Lagrangian

$$L^{(2)} = K[\mathbf{u}_s,\mathbf{u}_n]\omega^2 - U[\mathbf{u}_s,\mathbf{u}_n], \tag{7.8}$$

where

$$K[\mathbf{u}_s,\mathbf{u}_n] = \frac{1}{2}\int d\mathbf{r}\left\{\rho_{s0}\mathbf{u}_s^2 + \rho_{n0}\mathbf{u}_n^2\right\} \tag{7.9}$$

and

$$\begin{aligned} U[\mathbf{u}_s, \mathbf{u}_\mathrm{n}] &= \int d\mathbf{r} \left\{ -\frac{1}{2} \left(\frac{\partial \mu}{\partial \rho} \right)_s [\nabla \cdot (\rho_{s0} \mathbf{u}_\mathrm{s} + \rho_{\mathrm{n}0} \mathbf{u}_\mathrm{n})]^2 \right. \\ &\quad - \left(\frac{\partial T}{\partial \rho} \right)_s [\nabla \cdot (s_0 \mathbf{u}_n)] \, [\nabla \cdot (\rho_{s0} \mathbf{u}_s + \rho_{n0} \mathbf{u}_n)] \\ &\quad \left. - \frac{1}{2} \left(\frac{\partial T}{\partial s} \right)_\rho [\nabla \cdot (s_0 \mathbf{u}_n)]^2 \right\}. \end{aligned} \tag{7.10}$$

Equation (7.8) has exactly the form of a *harmonic oscillator*, where K is the kinetic energy part, and U the potential energy one. Now one varies $L^{(2)}$ instead of $S^{(2)}$.

As an example and to further illustrate the theoretical procedure we look at the *dipole* mode. This is the center of mass oscillation of the cloud. Choosing the z-axis as the one along which the oscillation takes place, the corresponding displacement field *Ansätze* , $f_i(\mathbf{r}) = \delta_{i,z}$ and $g_i(\mathbf{r}) = \delta_{i,z}$, lead to $\mathbf{u}_s(\mathbf{r}, t) = a_s \hat{z}$ and $\mathbf{u}_n(\mathbf{r}, t) = a_n \hat{z}$. One readily finds from Eq. (7.9)

$$K[a_s, a_n] = \frac{1}{2} \left(M_s a_s^2 + M_n a_n^2 \right), \tag{7.11}$$

where the masses are given by

$$M_s = \int d\mathbf{r} \rho_{s0}, \quad M_n = \int d\mathbf{r} \rho_{n0}. \tag{7.12}$$

For the potential part the result is

$$U[a_s, a_n] = \frac{1}{2} \left(k_s a_s^2 + k_n a_n^2 + k_{sn} (a_s - a_n)^2 \right), \tag{7.13}$$

where the *spring constants* k_s, k_n, and k_{sn} can be found in [Tay05]. These spring constants contain the thermodynamic information of the system.

To find the mode frequencies we first perform the variation of $L^{(2)}$ with Eqs. (7.11) and (7.13). The result is best expressed as

$$\begin{pmatrix} M_s \omega^2 - k_s - k_{sn} & k_{sn} \\ k_{sn} & M_n \omega^2 - k_n - k_{sn} \end{pmatrix} \begin{pmatrix} a_s \\ a_n \end{pmatrix} = 0. \tag{7.14}$$

After some simplifications that are described in the aforementioned reference, one solves the eigenvalue problem to find

$$\left[M_s M_n (\omega^2 - \omega_z^2) - k_{sn} (M_s + M_n) \right] (\omega^2 - \omega_z^2) = 0. \tag{7.15}$$

The two solutions are the in-phase dipole,

$$\omega = \omega_z \tag{7.16}$$

and the out-of-phase dipole,

$$\omega^2 = \omega_z^2 + \frac{M_s + M_n}{M_s M_n} k_{sn}. \tag{7.17}$$

From Eq. (7.16) it is clear that the frequency is *independent* of temperature and interactions. On the contrary, for Eq. (7.17) interactions play an important role. Noteworthy is the fact that *on resonance* also the frequency of the in-phase breathing mode is independent of temperature, as measured in [Kin05a, Tho05].

For the anisotropic 1D geometry, the conditions for hydrodynamic behavior are [Ber10]: as before, $\omega\tau_{\mathrm{R}} \ll 1$, or in other words, the mean free path, l, has to be much smaller than the wavelength, λ, of the sound wave, $l \ll \lambda$. Also, the radial size of the cloud, R_{perp}, should be much smaller than λ, $R_{\mathrm{perp}} \ll \lambda$. Finally, the viscous penetration depth, $\delta = \sqrt{\eta/\rho_n\omega}$, where η is the shear viscosity coefficient, should satisfy $\delta \gg R_{\mathrm{perp}}$. This last condition imposes a low frequency regime, $\omega \ll \omega_{\mathrm{per}}^2\tau_R$.

Moreover, we emphasize that the theory for the elongated trap geometry that is relevant to our experiments is being developed simultaneously to our work [Str11]. For the adiabatic oscillations this ongoing work predicts for a 1D geometry a collective mode frequency in the zero-temperature limit of

$$\omega_k^2 = (k+1)\left(\frac{k}{5}+1\right)\omega_z^2, \tag{7.18}$$

and for $T/T_{\mathrm{F}} \gg 1$

$$\omega_k^2 = \left(\frac{7k}{5}+1\right)\omega_z^2, \tag{7.19}$$

where k is the order of the mode. As discussed above, $k = 0$ and $k = 1$ are independent of the temperature. For $k > 1$, the temperature dependence of the mode, *ie*, the frequency change between the two limits, increases together with the order of the mode. The temperature region in between still has to be theoretically investigated. This will probably result in a model for the equation of state connecting the zero-temperature limit with the nondegenerate one.

7.3. Experimental technique

The starting point of the experimental sequence is a recompression at the end of the evaporation. This is done to stop the evaporation, namely, atoms spilling out of the trap, and to make the radial trapping potential more harmonic. The trap depth is increased from $U_a/k_{\mathrm{B}} = 250$ to 380 nK. The harmonic axial confinement is dominated by the residual magnetic confinement resulting from the curvature of the Feshbach field. At the end of the recompression the excitation is started.

To resonantly excite the different modes k we modulate the intensity of the repulsive potential. This is done with a 532 nm laser (Laser Quantum: Opus 2 W) with a beam waist of $\omega_0 = 22$ μm calculated from the beam size after the glass cell. The modulation is accomplished with a sinusoidal function with an average power of 110 μW, Fig. 7.1, which leads to a repulsive potential $V_{\mathrm{rep}}/k_{\mathrm{B}} =$ 8.9 nK. This excitation of the modes $k = 2$ and $k = 3$ also couples to $k = 1$.

To minimize the excitation of $k = 1$ we modulate the intensity of the dipole trap. The modulation of the trapping beam also excites the $k = 1$ mode. Hence, to compensate for its excitation with the repulsive potential, the trapping beam is modulated with the same frequency but opposite phase, Fig. 7.2. The amplitude of the modulation of the trapping potential is experimentally optimized and corresponds to the minimum required to excite the $k = 1$ mode this way.

We also control the position of the repulsive barrier along the axial direction of the cloud by displacing the beam using an AOM. The positioning control allows us to easily change from exciting even ($k = 1$ and $k = 3$) and odd ($k = 2$) modes. For the even modes the repulsive potential is

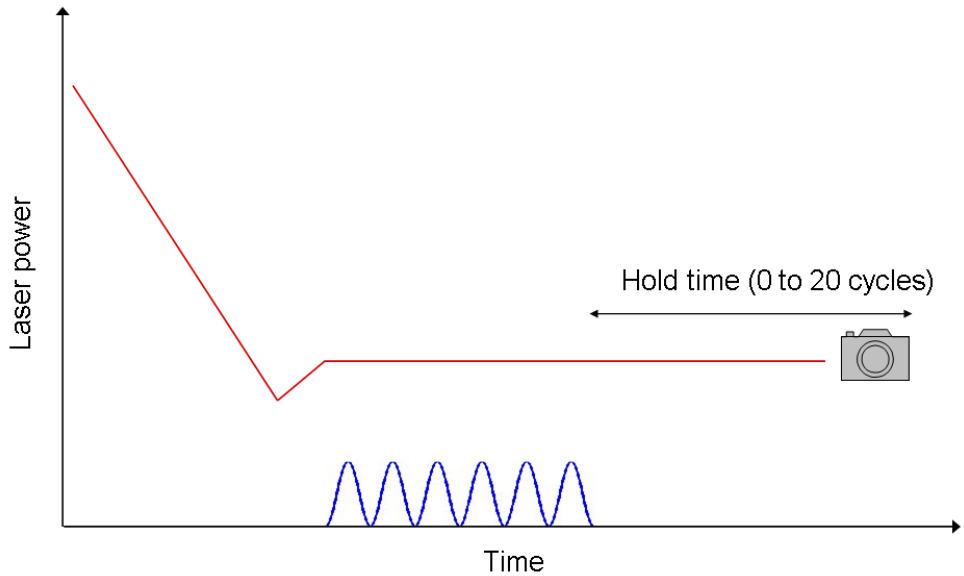

Figure 7.1.: Experimental sequence to excite the $k = 1$ collective mode. The red line is the intensity of the dipole trap, and the blue that of the repulsive potential. After the evaporation we recompress the trap slightly before exciting the mode. In this case, as opposed to the excitation of $k = 2$ and $k = 3$, the intensity of the dipole trap remains unmodulated.

centered with respect to the axial length of the cloud, whereas for the odd mode the beam is displaced off center by 27 μm. The latter position corresponds to the place where the theoretical density profile shows the largest density oscillation [Str11]. The control of the position also allows us to excite some modes by modulating the position of the beam, *eg*, the dipole mode.

As seen in Figs. 7.1 and 7.2, the modulation of the light intensity is done with a simple $h(\nu) = A\,(1 - \sin(2\pi\nu t + \pi/2))$ function, where ν is the modulation frequency and A the amplitude. However, we also tested switching the modulation on and off smoothly: we implemented an envelope on the signal, namely, $h(\nu)\sin \pi\nu t/n$, where n is the number of cycles. This was done to see if even a clearer mode signal was observed and to try to avoid any heating due to the excitation scheme. The test was done both with six and ten cycles of the excitation. Since no improvement was observed, it has not been used.

The modulation time was experimentally chosen to be six cycles of the given excitation frequency: it is enough to clearly excite a mode and short to consider the damping rates. After the excitation is finished the cloud is allowed to oscillate in the trap. An *in-situ* image is done after a variable hold time. The hold time is changed randomly from one experimental sequence to the next between zero and twenty times the period of the collective mode being excited. This span is chosen such

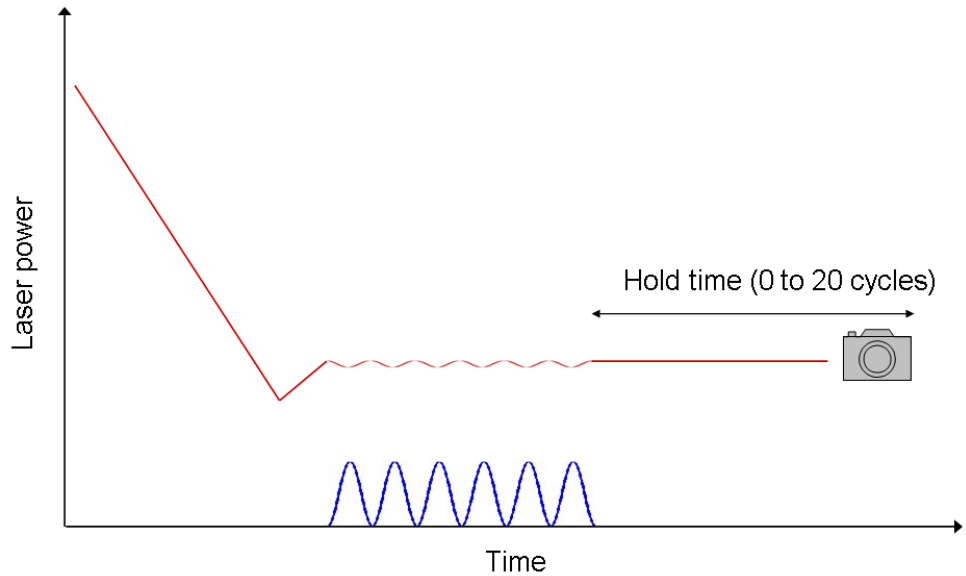

Figure 7.2.: Experimental sequence to excite the the $k = 2$ and 3 collective modes. The red line is the intensity of the dipole trap, and the blue that of the repulsive potential. The dipole trap is modulated to avoid exciting the $k = 1$ mode.

that the preferred frequency resolution of the Fourier analysis described below is met. Typically the sampling rate is at least six points per oscillation period, and on average six images are taken for each hold time.

7.4. Data analysis methodology

In this subsection we illustrate the methodology used to analyze the data using as an example the $k = 1$ mode. We begin by correcting for the intensity of the absorption imaging. This is required due to the fact that the polarization of the imaging light is σ_- along the direction perpendicular to the quantization axis, instead of the desired σ_- along the direction parallel to the quantization axis. The reason is that in our setup the imaging beam goes through the $\lambda/4$ waveplate that sets the polarization of one of the horizontal MOT beams. The s-polarized component of the imaging light leads to a π-polarized component in the quantization axis that is not absorbed by the atoms and is simply unscattered; it shows up as an offset in the images captured by the CCD camera. To quantize how large this second effect is we measure the ratio between p to s polarized light, which is found to be $p/s = 1.5$. We take this effect into account when processing the images. Firstly, we subtract the s-polarized light, and secondly, we rescale the intensity of the scattered

light on the camera to that of the p-polarized component. The result is a density profile in which the unscattered light is not present in the form of an intensity offset.

The corrected density profiles are then analyzed. To account for fluctuations, we identifying the astray images from the successful ones. To do this, we fit all the images to a polylog function. The resulting fit parameters are then compared to a set of boundary conditions that we impose, *eg*, a certain minimum number of particles should be met and interference fringes should not give an unrealistic position of the cloud. Those images that meet the conditions are kept for further analysis. The good images per hold time (about six images) are then averaged; the density profile without excitation is taken to be the average density profile of all the hold times. The difference between the averaged density profile at a given hold time with respect to the unexcited density profile, $\delta n(x,t)$, gives the density excitation at a position x along the axial density profile. This is shown in Fig. 7.3.

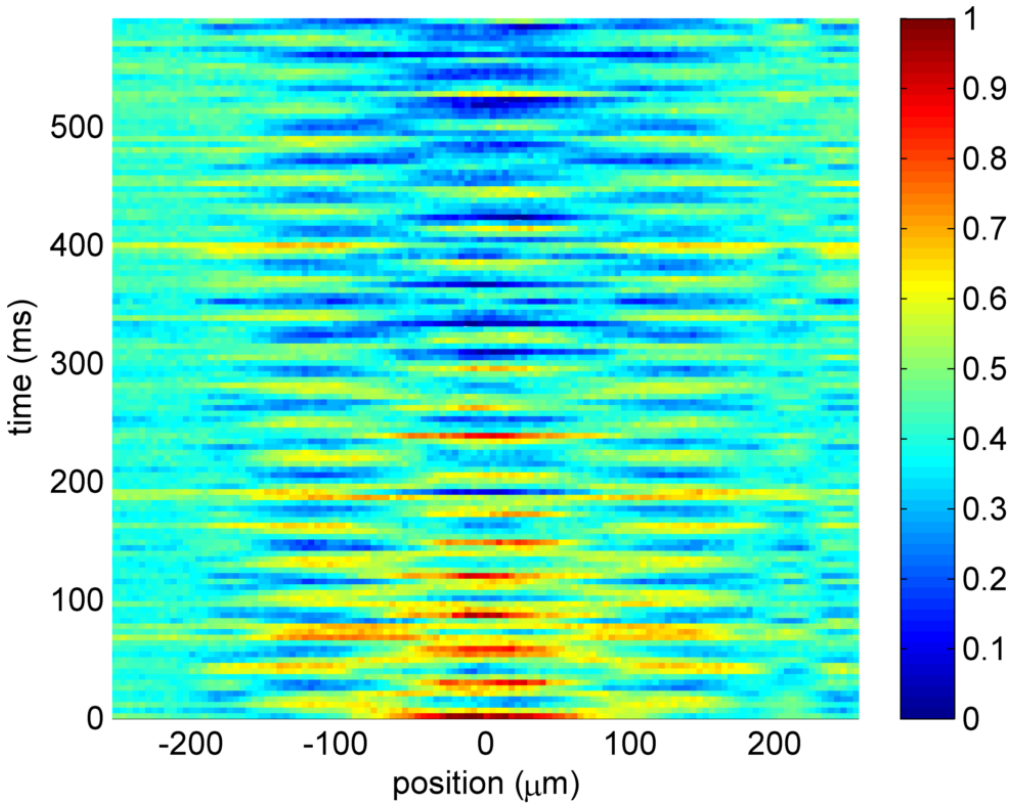

Figure 7.3.: Local density fluctuations, $\delta n(x,t)$, for the $k = 1$ collective mode.

We then proceed to carry out a Fourier analysis of the local number of atoms of the cloud to get the frequency spectrum of the excitation. We perform a fast Fourier transform (FFT) on $\delta n(x,t)$ for every fixed x. In order to get the largest amplitude of the fluctuation resulting from each FFT, the phase is chosen during the analysis such that there is no imaginary component in the outcome. The resulting frequency spectrum of the density modulation, $\delta n(x,f)$, shows the local density change with respect to the equilibrium position. We plot the power spectrum $|\delta n(x,f)|$, Fig. 7.4, so as to emphasize the nodes of the excitation.

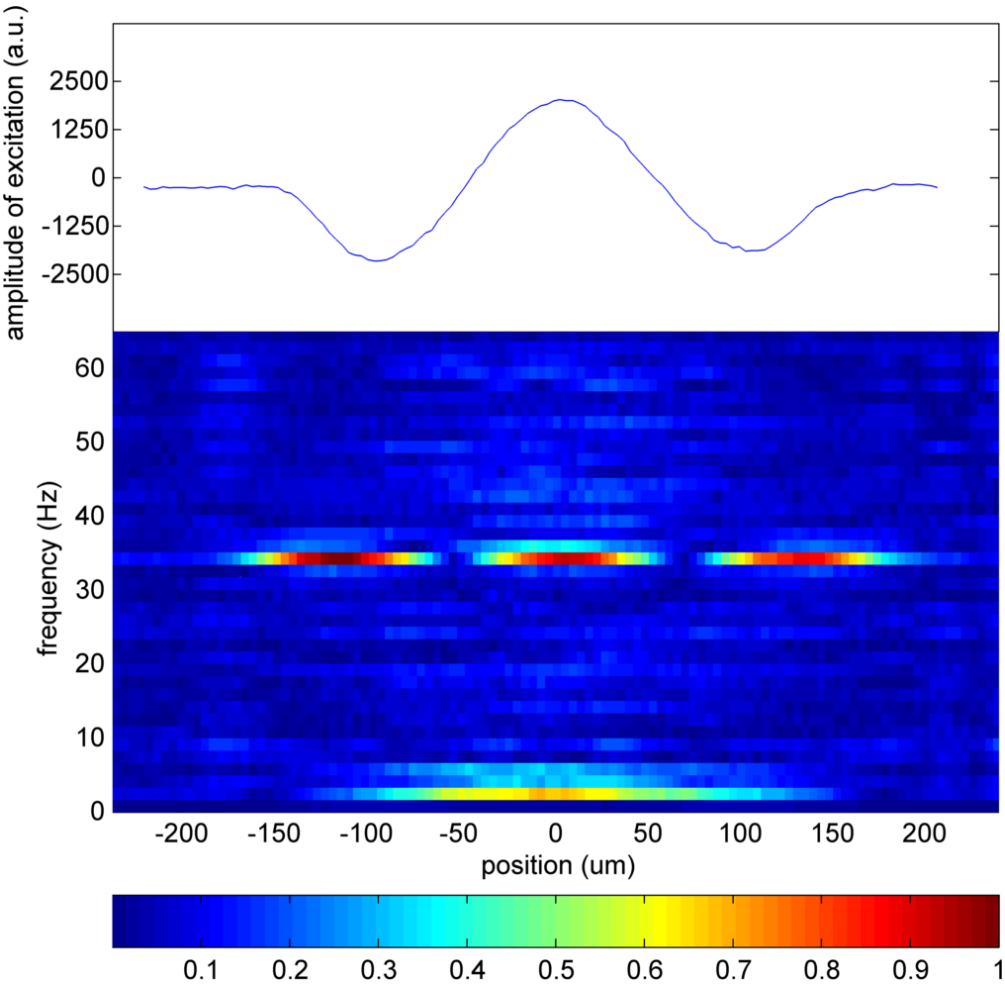

Figure 7.4.: Results for the $k = 1$ collective mode. Above: waveform, $\psi(x)$. Below: Power spectrum, $|\delta n(x, f)|$.

Next we use $\delta n(x, f)$ to execute a crucial part of the analysis to identify each collective mode: by fixing the frequency to the one at which the excitation takes place, $f_{\text{mode,fix}}$, we extract its waveform, $\psi(x) = \delta n(x, f_{\text{mode,fix}})$. The waveform, shown for $k = 1$ in Fig. 7.4, clearly shows the local density deviation from its equilibrium position, *ie*, the excitation. Moreover, $\psi(x)$ is useful for obtaining the amplitude of the excitation for a given hold time.

In order to recover the collective mode oscillation frequency we obtain the total excitation amplitude of the cloud for each hold time. The process can be divided into three steps: First we apply a Gaussian filter, $g(f)$, to $\delta n(x, f)$. The filter is centered around the predicted mode frequency to start with, Eq. (7.18). Here the theoretical prediction is used as a guideline, as it serves as initial condition for the iteration described below. The FWHM of the filter should be large enough to include all the relevant information, but still isolate the desired experimental mode frequency, f_k, from other contributions. In particular, to cut-off the low frequency components of the excitation

spectrum, which corresponds to atom loss. The one dimensional Gaussian filter has the usual form

$$g(f) = \frac{1}{\pi\zeta} \exp\left(-2\frac{(f-f_c)^2}{\zeta^2}\right), \tag{7.20}$$

where $\zeta = \mathrm{FWHM}/\sqrt{2\ln(2)}$. Then we perform an inverse FFT (IFFT) on the filtered frequency spectrum $\delta n(x,f)g(f)$. The result of the IFFT is the filtered profile of the density excitation, $\delta n'(x,t)$, shown in Fig. 7.5. Next, we weight each filtered density excitation at each time step by $\psi(x)$. Finally, we sum the weighted axial density per hold time to get the total density excitation as a function of time, $\delta n_{\mathrm{T}}(t) = \sum_x \delta n'(x,t)\psi(x)$, shown in Fig. 7.6.

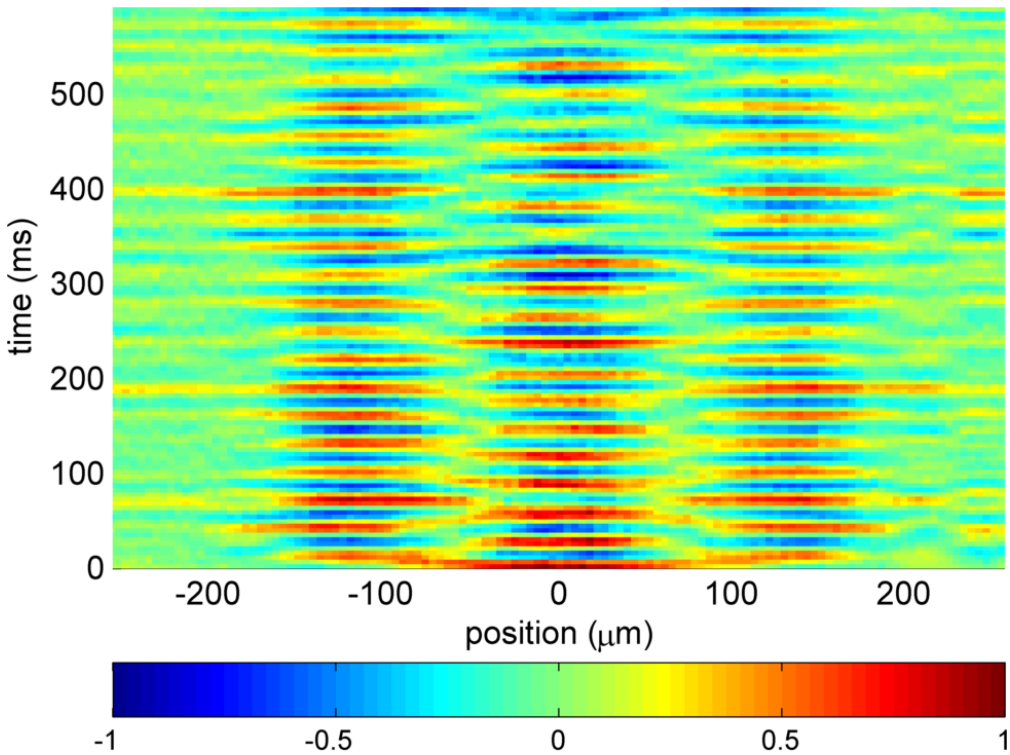

Figure 7.5.: Resulting $\delta n'(x,t)$ after an inverse FFT of $\delta n(x,f)$ using a Gaussian filter with FWHM of 50 Hz. A noteworthy difference to the unfiltered case, Fig. 7.3, is the constant offset around which the density oscillates.

Since the frequency resolution of $\delta n(x,f)$ does not allow the precise determination of the frequency of the excitation, the next step in the analysis is to determine f_k and Γ_k, the damping rate, of the collective oscillation. To this end we fit $\delta n_T(t)$ to a function $z(t) = z_0 + A_z \exp(-\Gamma_k t)\sin(2\pi f_k t + \phi)$, as shown in Fig. 7.6.

To ensure that our IFFT is optimized, we apply at this point a consistency criteria: $2\pi f_k/\omega_c < 10^{-4}$. If the criteria is unfulfilled, the above procedure to find δn_T is iterated using $g(f_c = f_k)$ each time. This procedure ensures that the Gaussian filter is properly centered around the mode frequency. Moreover, for the $k = 1$ mode we can compare the final value of the fit parameter f_k to the frequency obtained by fitting the oscillation of the axial width, shown in Fig. 7.7. The fact that both frequencies coincide reassures us of the validity of our Fourier analysis.

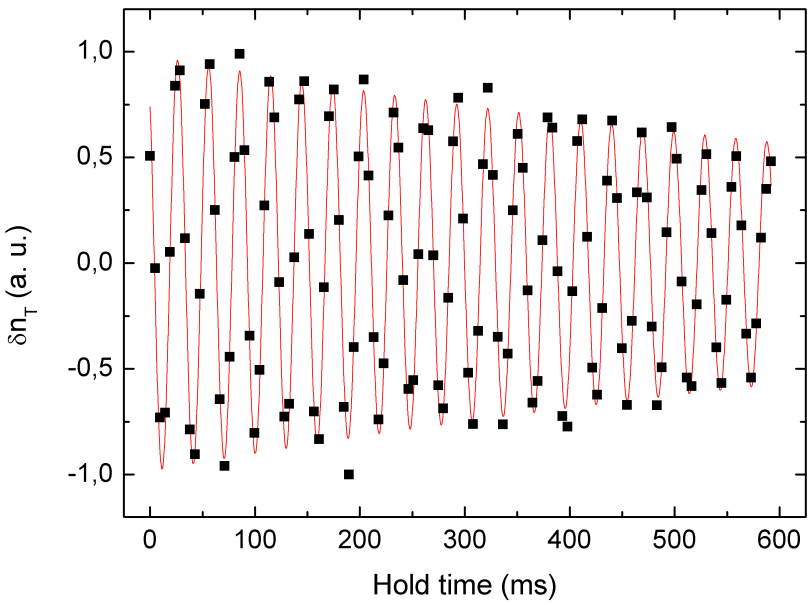

Figure 7.6.: Fit to the total density excitation δn_{T} for the collective oscillation $k = 1$.

This methodology is repeated for the different modes. The results are discussed and summarized in what follows.

7.5. Results and discussion

Performing the same analysis for the different higher order modes we obtain δn_{T}, Fig. 7.8, and summarize the fitted f_k and Γ_k in table 7.1. Pertaining f_k, the statistical error of the fit parameter is negligible: in the order of tens of mHz. In so far as the damping is concerned, it clearly increases as the order of the mode increases. In contrast to f_k, the fit parameter Γ_k has a larger error; this is probably due to the fact that the oscillations do not decay enough after 20 cycles to give an accurate fit of the exponential decay.

Table 7.1.: Fitted f_k and Γ_k for $k = 1$, 2, and 3.

k	f_k (Hz)	Error 10^{-3} (Hz)	Γ_k (s^{-1})	Error 10^{-3} (s^{-1})
1	33.826	11	0.91	74
2	44.499	22	1.66	146
3	54.652	20	3.17	133

We then compare our experimental results with the theoretical model. As seen in table 7.2 and

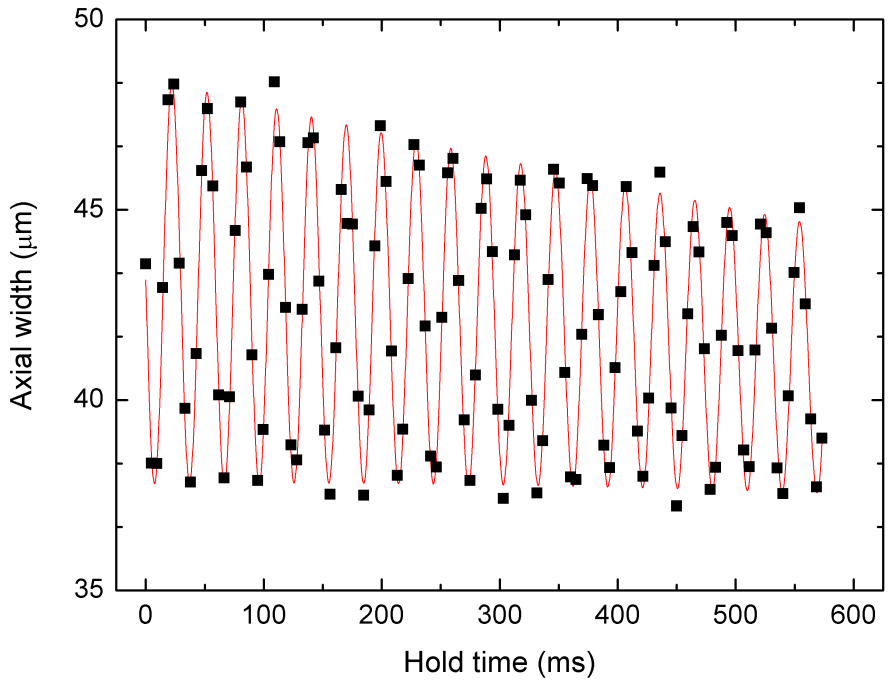

Figure 7.7.: Fit to the axial width of the cloud for the $k = 1$ mode before the Fourier analysis. We take this as a test to our methodology to analyze the collective modes: the fitted frequency of the reconstructed δn_{T} coincides with that of the axial width.

Fig. 7.9, we clearly see a deviation from the theoretical value, which increases linearly with the mode order. At least for the frequency of the k=1 mode, which, as mentioned before, it has been shown to coincide with the theoretical prediction, we believe that the deviation is due to anharmonic effects caused by a shallow trap depth in the radial direction. For the orders $k > 1$ we hypothesize whether nonlinear effect of the order (ω_z/ω_r) also contribute to the measured frequency deviation. Another plausible reason for the higher order modes is that they depend on the temperature; the actual finite temperature of the experiment may also lead to frequency shifts from the zero-temperature limit.

Comparing now $|\delta n(x, f_k)|$, Fig. 7.10, it is easy to discern the increasing number of nodes with each increasing order. One should stress here that the signal present at very low frequencies is well understood. It has to do with the loss of particles in the trap during the hold time. Hence, it is the result of the FFT of the linear slope. The decay of the number of particles is also seen in Figs. 7.3 and 7.7. In the former it is present in the color scale of the oscillations, which is above the average at the beginning of the hold time and below the average towards the end. In the latter as a time dependent offset. Furthermore, it is exactly the purpose of $g(f)$ to filter this drift in the particle number, as seen in the resulting oscillation Fig. 7.5. The same loss of particles was observed for

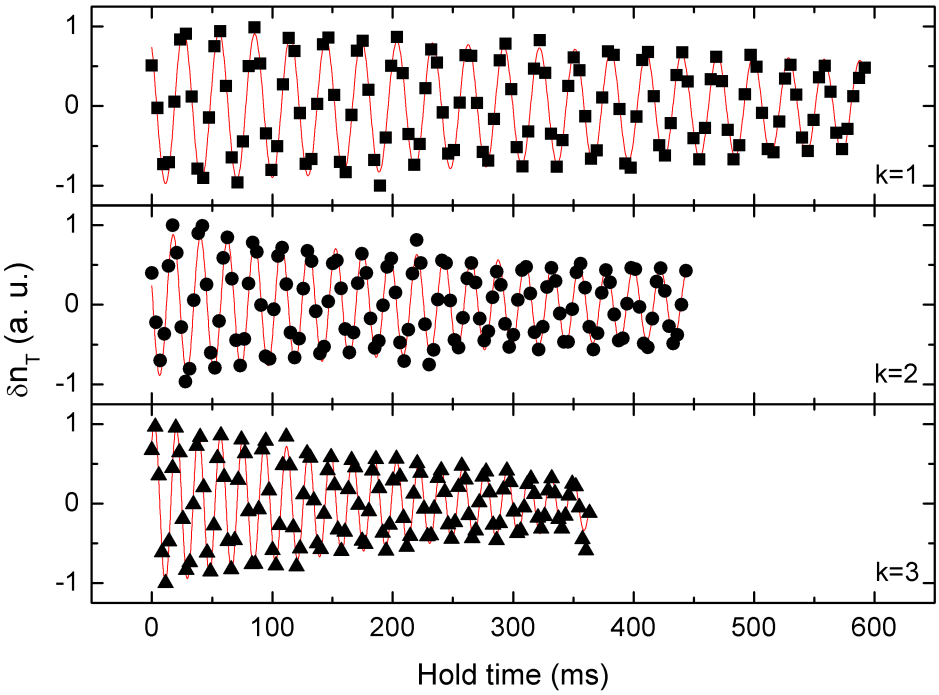

Figure 7.8.: Fit to the total density excitation, δn_T, for $k = 1$, 2, and 3. In every case the oscillation consists of 20 periods. The increase in Γ_k as k increases is easily perceived.

the unperturbed cloud, suggesting that it is simply the lifetime of the particles in the dipole trap. If it is due to heating as a result of anharmonic effects, a further recompression of the trap should improve the lifetime.

The different $\psi_k(x)$ are shown in Fig. 7.11. It is clearly discernible how the density oscillation changes from positive to negative, and to differentiate even from odd modes. It immediately reminds the reader of a fixed boundary standing wave, and its higher harmonics.

7.6. Conclusion and outlook

We have developed both the experimental technique and the analytical methodology to study higher order collective modes on resonance for the low temperature limit. Regarding the deviation of the frequencies from the theoretical prediction, ongoing work is being done to test whether anharmonic effects are the cause. Also the finite temperature at which the experiment actually takes place may contribute to the deviation. Be that as it may, with the easiness of the excitation scheme, the robustness of the oscillation, and the richness of the analysis, higher order modes seem set to offer a rich field of study of the resonant superfluid.

We expect both the technique and the methodology to extend to higher temperatures. Con-

Table 7.2.: Comparison between measured collective mode frequencies and the theoretical prediction.

k	$\omega_k/\omega_0\|_{\text{exp}}$	$\omega_k/\omega_0\|_{\text{theo}}$	ratio (%)
1	1.5175	1.549	97.96
2	1.9963	2.049	97.41
3	2.4519	2.530	96.91

cerning adiabatic higher order modes the nondegenerate limit should be straight forward to study; preferable with the highest possible order of the mode that one can reliable excite to have a better signal to noise ratio when comparing the high and low temperature limits. Moreover, it would be very interesting to connect the frequency evolution from one limiting case to the other, as this would further probe the equation of state. On the same note, since the spring constants in the theoretical model contain all the thermodynamic information of the system, its change may also shed some light into the evolution of the system.

Beyond density higher order collective modes, it should be assessed whether indeed these modes present a tool to study second sound. For the isotropic case the coupling between adiabatic and entropy modes is small, which has raised the issue of whether it is experimentally realizable. One can only hope for a larger coupling in the 1D case. Yet, bearing in mind the long lifetime of the excitations presented in this work and the ability to obtain the spectrum of the excitation, there seems to be room for pursuing new parameters of the excitation scheme that may lead to the coupling of the density and entropy oscillations. Also, there is the option of trying to measure the entropy wave directly, *ie*, try to heat up the gas locally and measure the local temperature change.

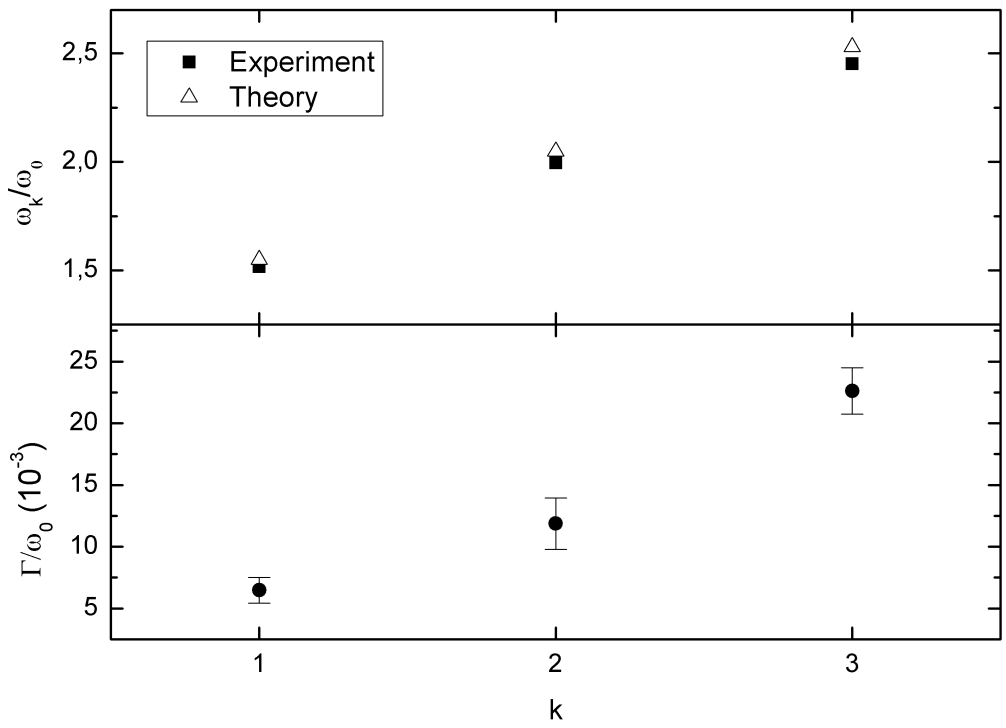

Figure 7.9.: Frequency and damping for $k = 1$, 2, and 3. Both quantities normalized to the axial trap frequency. The deviation of the measured frequency from the theoretical value increases together with k. The damping is also larger for the higher k.

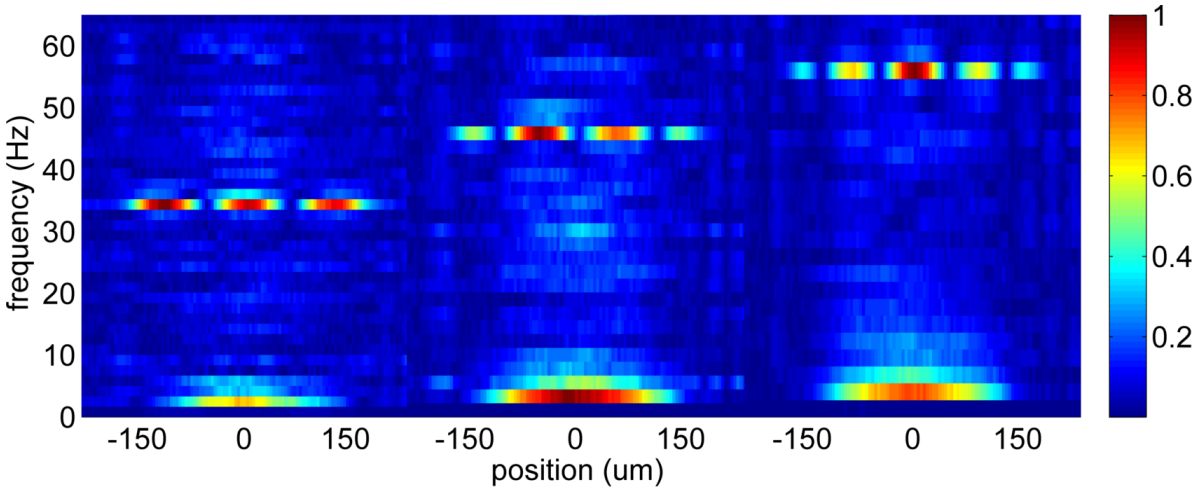

Figure 7.10.: Power spectrum for $k = 1$, 2, and 3. The increasing number of nodes of the modes is clearly seen. For $f < 10$ Hz the signal corresponds to atom loss.

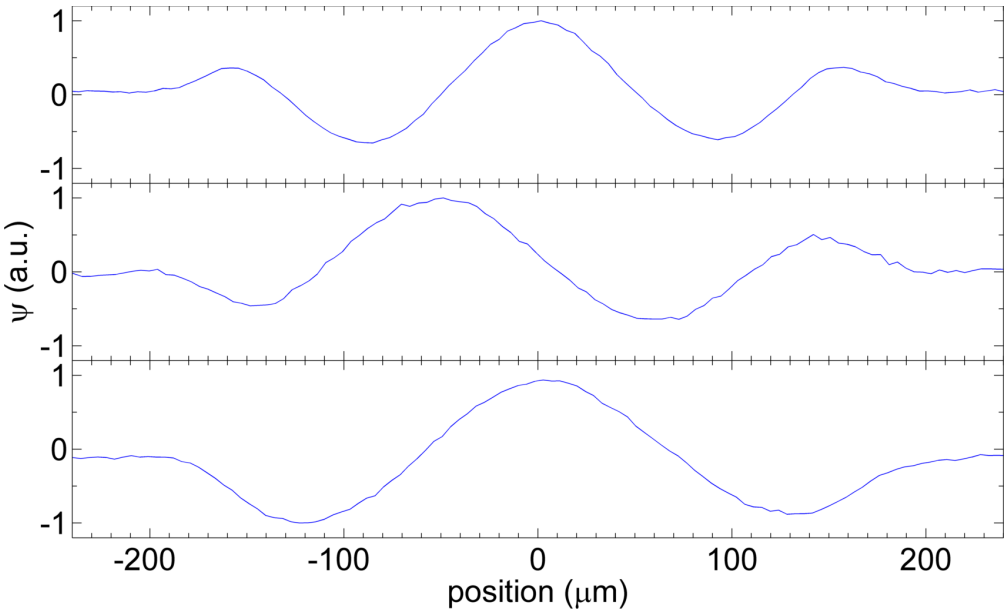

Figure 7.11.: Waveform for k=1, 2, and 3. The symmetry of the odd mode is clearly distinct from the even ones.

8. Outlook

As far as the immediate future is concerned, one should probe the higher order collective modes in the high temperature limit. Also the evolution of the frequency connecting the high and low temperature limits, that is to say, study their temperature dependence.

Beyond that, one should bear in mind that with the recent experimental characterization of the thermodynamic properties of a spin-balanced resonant superfluid, and the measurement of the *contact* pertaining to the Tan relations, the degenerate Fermi gas with unitarity limited interactions is quite well understood. The additional experiments concerning the pairing correlations, *eg*, size of the pairs and pseudogap regime, also present a quite complete picture of this aspect of the system, *albeit* a better understanding, both experimental and theoretical, of the many-body physics that it entails may be wanted. Even the dynamics seem to be quite complete with the measurements of the speed of sound, vortices, and different low-lying collective modes.

However, the study of the two-fluid model, which distinguishes strongly interacting quantum gases from the weakly interacting superfluid, is still pending. For all the studies of the gas on resonance, some of them exploiting the fact that the normal state is collisional hydrodynamic, the study of entropy waves is still awaiting. Whether a direct measurement by local thermometry, or indirectly by its predicted coupling with the adiabatic higher order collective modes such as the ones presented in this thesis, the measurement of entropy waves would finally differentiate the two fluid hydrodynamic system at hand.

Regarding the direct measurement, the challenge is the local thermal excitation that would result in an entropy wave, and the consequent measurement of the local temperature fluctuations. For the former one may try to pulse a repulsive barrier, and for the latter follow the same analysis as that of the thermodynamic studies already done. As for the direct measurement, one would have to carefully excite the cloud resonantly and look for signatures of the entropy wave in the Fourier analysis of the density oscillations.

Being past the characterization of the homonuclear resonant superfluid and given the techniques acquired during the last years to control and manipulate the ultracold degenerate Fermi gas, it is now an instrument to model and study ever more complicated atomic mixtures, internal state combinations, trap geometries, and certainly few-body and many-body effects.

A. Changes to the experimental apparatus

A.1. Repulsive potential and axial imaging setup

We present the schematic setup of the repulsive potential and the newly setup axial imaging system in Fig. A.1. The specified components are described in table A.1 below.

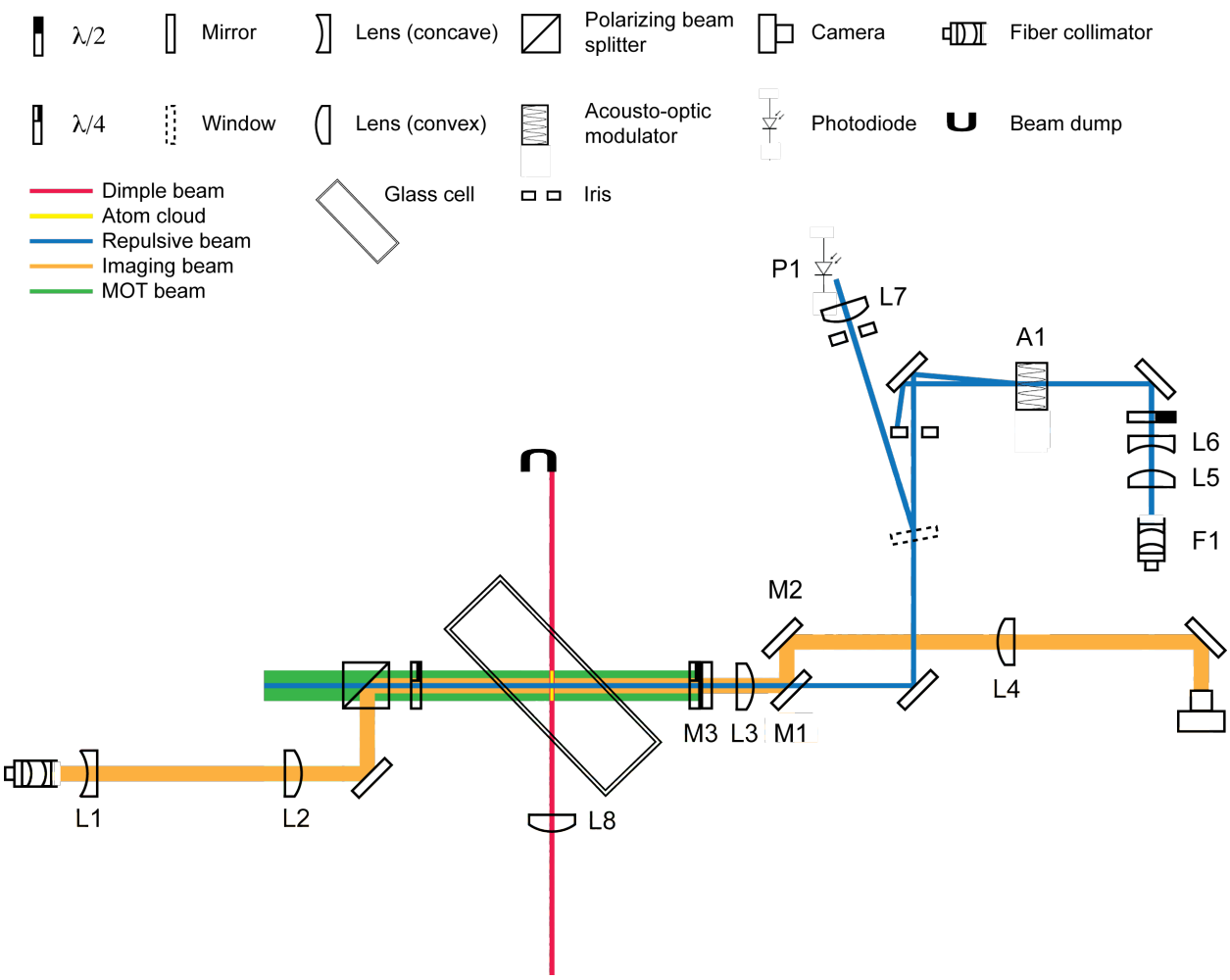

Figure A.1.: Schematic setup of the repulsive potential and the axial imaging system. The dipole trap beam is shown as a reference.

Table A.1.: Description of specified components

Name	Description
A1	Acoustic-optic modulator (AOM), 3200-125, Crystal Technology.
F1	Fiber collimator, 60FC-4M12-33, Schäfter + Kirchhoff.
L1	f = -75 mm ⌀= 25.4 mm
L2	f = 300 mm ⌀= 25.4 mm
L3	f = 100 mm ⌀= 50 mm, GRADIUM lens GPX-50-100-BB2, LightPath Technologies, Inc.
L4	f = 300 mm ⌀= 50.8 mm
L5	f = 75 mm ⌀= 25.4 mm
L6	f = -35 mm ⌀= 25.4 mm
L7	f = 40 mm ⌀= 25.4 mm
M1	⌀= 50.8 mm, Wedge = 1 deg. Coating: Surface 1: AR R<1%@532 nm 45 deg. Surface 2: R>99%@671 nm and 1030 nm, T>95%@532 nm 45 deg.
M2	⌀= 50.8 mm, Wedge = 1 deg. Coating: Surface 1: AR R<1%@1030 nm 45 deg. Surface 2:R>99%@671 nm, T>95%@1030 nm 45 deg.
M3	MOT mirror, it is displaced with a servo motor after the MOT is switched off.
P1	Intensity stabilization detector, DET36A/M, Thorlabs.

A.2. General changes to the apparatus

In this section we briefly introduce changes in the experimental setup that somehow represent a change in paradigm. For instance, a major change in the experimental setup was the substitution of the VersaDisk ELS ($\lambda = 1030$ nm) laser that we used as dipole trap for an IPG 50 W multimode Ytterbium fiber laser ($\lambda = 1070$ nm). This improved the reliability of the experiment greatly. Previously the ELS suffered from thermal drifts that resulted in the power dropping when it lased in between a mode hop. In addition, each time that it had to be serviced (every couple of months) to optimize the power and the beam profile by adjusting the etalon and Lyot filter, the pointing direction changed. This meant the rest of the components along the beam path leading up to the glass cell had to be adjusted.

Another significant change was the substitution of most voltage controlled oscillators (VCO) for direct digital synthesizers (DDS), which are digitally controlled frequency generators. The DDS, as opposed to the VCO, does not show frequency drifts. It can also be controlled exactly with the bus system, hence, it is not affected by noise in the control signal, *eg*, ground loops. Since we have not yet implemented the bus system, the VCOs that remain to be changed are those which frequency is changed during the experimental sequence. Specifically, the VCO of the two laser frequency beat-locks. The DDSs increased the stability of the experiment.

The substitution of the mechanical relays for a set of MOSFETs and PowerMOSFETs mounted on a water cooled copper block improved the stability of the MOT. We replaced the switching of

the Zeeman slower coils, the MOT coils, and other compensation coils for MOSFETs. MOSFETs are faster and more reliable than mechanical relays. In addition, since the MOT is loaded for several seconds, they are less susceptible to external factors, in particular since the temperature of the MOSFETs is regulated with the cooling block.

Bibliography

[Abe66] W. R. Abel, A. C. Anderson, and J. C. Wheatley, *Propagation of Zero Sound in Liquid $He3$ at Low Temperatures*, Phys. Rev. Lett. **17**, 74 (1966).

[Abo02] J. R. Abo-Shaeer, C. Raman, and K. W., *Formation and Decay of Vortex Lattices in Bose-Einstein Condensates at Finite Temperatures*, Phys. Rev. Lett. **88**, 070409 (2002).

[Ada94] C. S. Adams, M. Sigel, and J. Mlynek, *Atom optics*, Phys. Rep. **240**, 143 (1994).

[Alt07a] A. Altmeyer, S. Riedl, C. Kohstall, M. J. Wright, R. Geursen, M. Bartenstein, C. Chin, J. Hecker Denschlag, and R. Grimm, *Precision Measurements of Collective Oscillations in the BEC-BCS Crossover*, Phys. Rev. Lett. **98**, 040401 (2007).

[Alt07b] A. Altmeyer, S. Riedl, M. J. Wright, C. Kohstall, J. Hecker Denschlag, and R. Grimm, *Dynamics of a strongly interacting Fermi gas: The radial quadrupole mode*, Phys. Rev. A **76**, 033610 (2007).

[And95] M. H. Anderson, J. R. Ensher, M. R. Matthews, C. E. Wieman, and E. A. Cornell, *Observation of Bose-Einstein condensation in dilute atomic vapor*, Science **269**, 198 (1995).

[And97a] M. R. Andrews, D. M. Kurn, H.-J. Miesner, D. S. Durfee, C. G. Townsend, and W. Inouye, S. and. Ketterle, *Propagation of Sound in a Bose-Einstein Condensate*, Phys. Rev. Lett. **79**, 553 (1997).

[And97b] M. R. Andrews, C. G. Townsend, H. J. Miesner, D. S. Durfee, D. M. Kurn, and W. Ketterle, *Observation of Interference Between Two Bose Condensates*, Science **275**, 637 (1997).

[And98] M. R. Andrews, D. M. Stamper-Kurn, H.-J. Miesner, D. S. Durfee, C. G. Townsend, and W. Inouye, S. and. Ketterle, *Erratum: Propagation of Sound in a Bose-Einstein Condensate*, Phys. Rev. Lett. **80**, 2967 (1998).

[Ara09] E. Arahata and T. Nikuni, *Propagation of second sound in a superfluid Fermi gas in the unitary limit*, Phys. Rev. A **80**, 043613 (2009).

[Arn99] M. Arndt, O. Nairz, J. Vos-Andreae, C. Keller, G. van der Zouw, and A. Zeilinger, *Waveparticle duality of C_{60} molecules*, Nature **401**, 680 (1999).

[Ast05] G. E. Astrakharchik, R. Combescot, X. Leyronas, and S. Stringari, *Equation of State and Collective Frequencies of a Trapped Fermi Gas Along the BEC-Unitarity Crossover*, Phys. Rev. Lett. **95**, 030404 (2005).

[Ban00] Y. B. Band, M. Trippenbach, J. P. Burke, and P. S. Julienne, *Elastic Scattering Loss of Atoms from Colliding Bose-Einstein Condensate Wave Packets*, Phys. Rev. Lett. **84**, 5462 (2000).

[Ban01] Y. B. Band, J. P. Burke, A. Simoni, and P. S. Julienne, *Suppression of elastic scattering loss for slowly colliding Bose-Einstein condensates*, Phys. Rev. A **64**, 023607 (2001).

[Bar57] J. Bardeen, L. N. Cooper, and J. R. Schrieffer, *Theory of Superconductivity*, Phys. Rev. **108**, 1175 (1957).

[Bar04a] M. Bartenstein, A. Altmeyer, S. Riedl, S. Jochim, C. Chin, J. Hecker Denschlag, and R. Grimm, *Collective Excitations of a Degenerate Gas at the BEC-BCS Crossover*, Phys. Rev. Lett. **92**, 203201 (2004).

[Bar04b] M. Bartenstein, A. Altmeyer, S. Riedl, S. Jochim, C. Chin, J. Hecker Denschlag, and R. Grimm, *Crossover from a Molecular Bose-Einstein Condensate to a Degenerate Fermi Gas*, Phys. Rev. Lett. **92**, 120401 (2004).

[Bar05] M. Bartenstein, A. Altmeyer, S. Riedl, R. Geursen, S. Jochim, C. Chin, J. Hecker Denschlag, R. Grimm, A. Simoni, E. Tiesinga, C. J. Williams, and P. S. Julienne, *Precise determination of ^{6}Li cold collision parameters by radio-frequency spectroscopy on weakly bound molecules*, Phys. Rev. Lett. **94**, 103201 (2005).

[Ber10] G. Bertaina, L. Pitaevskii, and S. Stringari, *First and Second Sound in Cylindrically Trapped Gases*, Phys. Rev. Lett. **105**, 150402 (2010).

[Bon04] K. Bongs and K. Sengstock, *Physics with coherent matter waves*, Rep. Prog. Phys. **67**, 907 (2004).

[Bou03] T. Bourdel, J. Cubizolles, L. Khaykovich, K. M. F. Magalhães, S. J. J. M. F. Kokkelmans, G. V. Shlyapnikov, and C. Salomon, *Measurement of the Interaction Energy near a Feshbach Resonance in a ^{6}Li Fermi Gas*, Phys. Rev. Lett. **91**, 020402 (2003).

[Bou04] T. Bourdel, L. Khaykovich, J. Cubizolles, J. Zhang, F. Chevy, M. Teichmann, L. Tarruell, S. J. J. M. F. Kokkelmans, and C. Salomon, *Experimental Study of the BEC-BCS Crossover Region in Lithium 6*, Phys. Rev. Lett. **93**, 050401 (2004).

[Bra95] C. C. Bradley, C. A. Sackett, J. J. Tollett, and R. G. Hulet, *Evidence of Bose-Einstein condensation in an atomic gas with attractive interactions*, Phys. Rev. Lett. **75**, 1687 (1995).

[Bra06] E. Braaten and H.-W. Hammer, *Universality in few-body systems with large scattering length*, Phys. Rep. **428**, 259 (2006).

[Bre03] V. Bretin, P. Rosenbusch, F. Chevy, G. V. Shlyapnikov, and J. Dalibard, *Quadrupole Oscillation of a Single-Vortex Bose-Einstein Condensate: Evidence for Kelvin Modes*, Phys. Rev. Lett. **90**, 100403 (2003).

[Bru99] G. M. Bruun and C. W. Clark, *Hydrodynamic Excitations of Trapped Fermi Gases*, Phys. Rev. Lett. **83**, 5415 (1999).

[Bru05] G. M. Bruun and H. Smith, *Viscosity and thermal relaxation for a resonantly interacting Fermi gas*, Phys. Rev. A **72**, 043605 (2005).

[Bru07] G. M. Bruun and H. Smith, *Frequency and damping of the scissors mode of a Fermi gas*, Phys. Rev. A **76**, 045602 (2007).

[Bug04] C. Buggle, J. Léonard, W. von Klitzing, and J. T. M. Walraven, *Interferometric Determination of the s and d-Wave Scattering Amplitudes in ^{87}Rb*, Phys. Rev. Lett. **93**, 173202 (2004).

[Bul05] A. Bulgac and G. F. Bertsch, *Collective Oscillations of a Trapped Fermi Gas near the Unitary Limit*, Phys. Rev. Lett. **94**, 070401 (2005).

[Cao11] C. Cao, E. Elliott, J. Joseph, H. Wu, J. Petricka, T. Schfer, and J. Thomas, *Universal Quantum Viscosity in a Unitary Fermi Gas*, Science **331**, 58 (2011).

[Cas97] Y. Castin and J. Dalibard, *Relative phase of two Bose-Einstein condensates*, Phys. Rev. A **55**, 4330 (1997).

[Ced07] L. S. Cederbaum, A. I. Streltsov, Y. B. Band, and O. E. Alon, *Interferences in the Density of Two Bose-Einstein Condensates Consisting of Identical or Different Atoms*, Phys. Rev. Lett. **98**, 110405 (2007).

[Che00] F. Chevy, K. M. Madison, and J. Dalibard, *Measurement of the Angular Momentum of a Rotating Bose-Einstein Condensate*, Phys. Rev. Lett. **85**, 2223 (2000).

[Che03] F. Chevy and S. Stringari, *Kelvin modes of a fast rotating Bose-Einstein condensate*, Phys. Rev. A **68**, 053601 (2003).

[Che05] Q. Chen, J. Stajic, and K. Levin, *Thermodynamics of Interacting Fermions in Atomic Traps*, Phys. Rev. Lett. **95** (2005).

[Chi00] A. P. Chikkatur, A. Görlitz, D. M. Stamper-Kurn, S. Inouye, S. Gupta, and W. Ketterle, *Suppression and Enhancement of Impurity Scattering in a Bose-Einstein Condensate*, Phys. Rev. Lett. **85**, 483 (2000).

[Chi04a] C. Chin, M. Bartenstein, A. Altmeyer, S. Riedl, S. Jochim, J. Hecker Denschlag, and R. Grimm, *Observation of the Pairing Gap in a Strongly Interacting Fermi Gas*, Science **305**, 1128 (2004).

[Chi04b] C. Chin, M. Bartenstein, A. Altmeyer, S. Riedl, S. Jochim, J. Hecker Denschlag, and R. Grimm, *Observation of the Pairing Riedl2008coo in a Strongly Interacting Fermi Gas*, Science **305**, 1128 (2004).

[Chi06] J. K. Chin, D. E. Miller, Y. Liu, C. Stan, W. Setiawan, C. Sanner, K. Xu, and W. Ketterle, *Evidence for superfluidity of ultracold fermions in an optical lattice*, Nature **443**, 961 (2006).

[Chi10] C. Chin, R. Grimm, P. S. Julienne, and E. Tiesinga, *Feshbach resonances in ultracold gases*, Rev. Mod. Phys. **82**, 1225 (2010).

[Cla07] B. Clancy, L. Luo, and J. E. Thomas, *Observation of Nearly Perfect Irrotational Flow in Normal and Superfluid Strongly Interacting Fermi Gases*, Phys. Rev. Lett. **99**, 140401 (2007).

[Coo56] L. N. Cooper, *Bound Electron Pairs in a Degenerate Fermi Gas*, Phys. Rev. **104**, 1189 (1956).

[Cos10] L. Costa, J. Brachmann, A.-C. Voigt, C. Hahn, M. Taglieber, T. W. Hänsch, and K. Dieckmann, *s-wave interaction in a two-species Fermi-Fermi mixture at a narrow Feshbach resonance*, Phys. Rev. Lett. **105**, 123201 (2010).

[Cou98] P. Courteille, R. S. Freeland, D. J. Heinzen, F. A. van Abeelen, and B. J. Verhaar, *Observation of a Feshbach Resonance in Cold Atom Scattering*, Phys. Rev. Lett. **81**, 69 (1998).

[Cro09] A. D. Cronin, J. Schmiedmayer, and D. E. Pritchard, *Optics and interferometry with atoms and molecules*, Rev. Mod. Phys. **81**, 1051 (2009).

[Cub03] J. Cubizolles, T. Bourdel, S. J. J. M. F. Kokkelmans, G. V. Shlyapnikov, and C. Salomon, *Production of Long-Lived Ultracold Li_2 Molecules from a Fermi Gas*, Phys. Rev. Lett. **91**, 240401 (2003).

[Dal99] F. Dalfovo, S. Giorgini, L. P. Pitaevskii, and S. Stringari, *Theory of Bose-Einstein condensation in trapped gases*, Rev. Mod. Phys. **71**, 463 (1999).

[Dav27] C. J. Davisson and L. H. Germer, *The Scattering of Electrons by a Single Crystal of Nickel*, Nature **119**, 558 (1927).

[Dav95] K. B. Davis, M. O. Mewes, M. R. Andrews, N. J. van Druten, D. S. Durfee, D. M. Kurn, and W. Ketterle, *Bose-Einstein condensation in a gas of sodium atoms*, Phys. Rev. Lett. **75**, 3969 (1995).

[de 23] L. de Broglie, *Waves and Quanta*, Nature **112**, 540 (1923).

[DeM99a] B. DeMarco, J. L. Bohn, J. P. Burke, Jr., M. Holland, and D. S. Jin, *Measurement of p-Wave Threshold Law Using Evaporatively Cooled Fermionic Atoms*, Phys. Rev. Lett. **82**, 4208 (1999).

[DeM99b] B. DeMarco and D. S. Jin, *Onset of Fermi Degeneracy in a Trapped Atomic Gas*, Science **285**, 1703 (1999).

[Die02] K. Dieckmann, C. A. Stan, S. Gupta, Z. Hadzibabic, C. H. Schunck, and W. Ketterle, *Decay of an Ultracold Fermionic Lithium Gas near a Feshbach Resonance*, Phys. Rev. Lett. **89**, 203201 (2002).

[Dod97] R. J. Dodd, K. Burnett, M. Edwards, and C. Clark, *Excitation spectroscopy of vortex states in dilute Bose-Einstein condensed gases*, Phys. Rev. A **56**, 587 (1997).

[Du08] X. Du, L. Luo, B. Clancy, and J. E. Thomas, *Observation of anomalous spin segregation in a trapped Fermi gas*, Phys. Rev. Lett. **101**, 150401 (2008).

[Du09a] X. Du, Y. Zhang, J. Petricka, and J. E. Thomas, *Controlling Spin Current in a Trapped Fermi Gas*, Phys. Rev. Lett. **103**, 010401 (2009).

[Du09b] X. Du, Y. Zhang, and J. E. Thomas, *Inelastic Collisions of a Fermi Gas in the BEC-BCS Crossover*, Phys. Rev. Lett. **102**, 250402 (2009).

[Dui04] R. Duine and H. Stoof, *Atom–molecule coherence in Bose gases*, Phys. Rep. **396**, 115 (2004).

[Dür04] S. Dürr, T. Volz, A. Marte, and G. Rempe, *Observation of Molecules Produced from a Bose-Einstein Condensate*, Phys. Rev. Lett. **92** (2004).

[Dyk11] E. D. Dyke, P. and. Kuhnle, S. Whitlock, H. Hu, M. Mark, S. Hoinka, M. Lingham, P. Hannaford, and C. J. Vale, *Crossover from 2D to 3D in aWeakly Interacting Fermi Gas*, Phys. Rev. Lett. **106**, 105304 (2011).

[Eag69] D. M. Eagles, *Possible pairing without superconductivity at low carrier concentrations in bulk and thin-film superconducting semiconductors*, Phys. Rev. **186**, 456 (1969).

[Efi70] V. Efimov, *Energy levels arising from resonant two-body forces in a three-body system*, Phys. Lett. B **33**, 563 (1970).

[Efi71] V. Efimov, *Weakly-bound states of three resonantly-interacting particles*, Sov. J. Nucl. Phys. **12**, 589 (1971).

[Efi79] V. Efimov, *Low-energy properties of three resonantly interacting particles*, Sov. J. Nuc. Phys. **29**, 546 (1979).

[Est30] I. Estermann and O. Stern, *Beugung von Molekularstrahlen*, Z. Phys. **61**, 95 (1930).

[Fan61] U. Fano, *Effects of configuration interaction on intensities and phase shifts*, Phys. Rev. **124**, 1866 (1961).

[Far00] M. Farine, P. Schuck, and X. Viñas, *Moment of inertia of a trapped superfluid gas of atomic fermions*, Phys. Rev. A **62**, 013608 (2000).

[Fer08] F. Ferlaino, S. Knoop, M. Mark, M. Berninger, H. Schöbel, H.-C. Nägerl, and R. Grimm, *Collisions between tunable halo dimers: Exploring an elementary four-body process with identical bosons*, Phys. Rev. Lett. **101**, 023201 (2008).

[Fes58] H. Feshbach, *Unified theory of nuclear reactions*, Ann. Phys. (N.Y.) **5**, 357 (1958).

[Fes62] H. Feshbach, *Unified theory of nuclear reactions II*, Ann. Phys. (N.Y.) **19**, 287 (1962).

[Fuc08] J. Fuchs, C. Ticknor, P. Dyke, G. Veeravalli, E. Kuhnle, W. Rowlands, and C. J. Hannaford, P. and. Vale, *Binding energies of 6Li p-wave Feshbach molecules*, Phys. Rev. Lett. **77**, 053616 (2008).

[Ful64] P. Fulde and R. A. Ferrell, *Superconductivity in a Strong Spin-Exchange Field*, Phys. Rev. **135**, A550 (1964).

[Gae07] J. P. Gaebler, J. T. Stewart, J. L. Bohn, and D. S. Jin, *p-wave Feshbach molecules*, Phys. Rev. Lett. **98**, 200403 (2007).

[Gae10] J. P. Gaebler, J. T. Stewart, T. E. Drake, D. S. Jin, A. Perali, P. Pieri, and G. C. Strinati, *Observation of pseudogap behaviour in a strongly interacting Fermi gas*, Nature Phys. **6**, 569 (2010).

[Ger11] S. Gerlich, S. Eibenberger, M. Tomandl, S. Nimmrichter, K. Hornberger, P. J. Fagan, J. Tüxen, M. Mayor, and M. Arndt, *Quantum interference of large organic molecules*, Nat. Commun. **2**, 263 (2011).

[Gio08] S. Giorgini, L. P. Pitaevskii, and S. Stringari, *Theory of ultracold atomic Fermi gases*, Rev. Mod. Phys. **80**, 1215 (2008).

[GO99a] D. Guéry-Odelin and S. Stringari, *Scissors Mode and Superfluidity of a Trapped Bose-Einstein Condensed Gas*, Phys. Rev. Lett. **83**, 4452 (1999).

[GO99b] D. Guéry-Odelin, F. Zambelli, J. Dalibard, and S. Stringari, *Collective oscillations of a classical gas confined in harmonic traps*, Phys. Rev. A **60**, 4851 (1999).

[GO00] D. Guéry-Odelin, *Spinning up and down a Boltzmann gas*, Phys. Rev. A **62**, 033607 (2000).

[Gra02] S. R. Granade, M. E. Gehm, K. M. O'Hara, and J. E. Thomas, *All-Optical Production of a Degenerate Fermi Gas*, Phys. Rev. Lett. **88**, 120405 (2002).

[Gre03] M. Greiner, C. A. Regal, and D. S. Jin, *Emergence of a Molecular Bose-Einstein Condensate from a Fermi Gas*, Nature **426**, 537 (2003).

[Gre11] D. Greif, L. Tarruell, T. Uehlinger, R. Jördens, and T. Esslinger, *Probing Nearest-Neighbor Correlations of Ultracold Fermions in an Optical Lattice*, Phys. Rev. Lett. **106**, 145302 (2011).

[Gri09] A. Griffin, T. Nikuni, , and E. Zaremba, *Bose-Condensed Gases at Finite Temperatures*, Cambridge University Press, 2009.

[Hac10] L. Hackermüller, U. Schneider, M. Moreno-Cardoner, T. Kitagawa, T. Best, S. Will, E. Demler, E. Altman, I. Bloch, and B. Paredes, *Anomalous Expansion of Attractively Interacting Fermionic Atoms in an Optical Lattice*, Science **327**, 1621 (2010).

[Had02] Z. Hadzibabic, C. A. Stan, K. Dieckmann, S. Gupta, M. W. Zwierlein, A. Görlitz, and W. Ketterle, *Two-Species Mixture of Quantum Degenerate Bose and Fermi Gases*, Phys. Rev. Lett. **88**, 160401 (2002).

[Had06] Z. Hadzibabic, P. Krger, M. Cheneau, B. Battelier, and J. Dalibard, *Berezinskii-Kosterlitz-Thouless crossover in a trapped atomic gas*, Nature **441**, 1118 (2006).

[Hal01a] P. C. Haljan, B. P. Anderson, I. Coddington, and E. A. Cornell, *Use of Surface-Wave Spectroscopy to Characterize Tilt Modes of a Vortex in a Bose-Einstein Condensate*, Phys. Rev. Lett. **86**, 2922 (2001).

[Hal01b] P. C. Haljan, I. Coddington, P. Engels, and E. A. Cornell, *Driving Bose-Einstein-Condensate Vorticity with a Rotating Normal Cloud*, Phys. Rev. Lett. **87**, 210403 (2001).

[Hau08] R. Haussmann and W. Zwerger, *Thermodynamics of a trapped unitary Fermi gas*, Phys. Rev. A **78**, 063602 (2008).

[He07] Y. He, Q. Chen, C.-C. Chien, and K. Levin, *First- and second-sound-like modes at finite temperature in trapped Fermi gases from BCS to BEC*, Phys. Rev. A **76**, 051602(R) (2007).

[Hei04] H. Heiselberg, *Collective Modes of Trapped Gases at the BEC-BCS Crossover*, Phys. Rev. Lett. **94**, 040402 (2004).

[Her03] J. Herbig, T. Kraemer, M. Mark, T. Weber, C. Chin, H.-C. Nägerl, and R. Grimm, *Preparation of a pure molecular quantum gas*, Science **301**, 1510 (2003).

[Hes67] G. B. Hess and W. M. Fairbank, *Measurements of Angular Momentum in Superfluid Helium*, Phys. Rev. Lett. **19**, 216 (1967).

[Ho04] T.-L. Ho, *Universal Thermodynamics of Degenerate Quantum Gases in the Unitarity Limit*, Phys. Rev. Lett. **92**, 090402 (2004).

[Ho10] T.-L. Ho and Q. Zhou, *Obtaining the phase diagram and thermodynamic quantities of bulk systems from the densities of trapped gases*, Nature Phys. **6**, 131 (2010).

[Hod02] E. Hodby, G. Hechenblaikner, S. A. Hopkins, O. M. Maragò, and C. J. Foot, *Vortex Nucleation in Bose-Einstein Condensates in an Oblate, Purely Magnetic Potential*, Phys. Rev. Lett. **88**, 010405 (2002).

[Hof07] S. Hofferberth, I. Lesanovsky, B. Fischer, T. Schumm, and J. Schmiedmayer, *Non-equilibrium coherence dynamics in one-dimensional Bose gases*, Nature **449**, 324 (2007).

[Hor10] M. Horikoshi, S. Nakajima, M. Ueda, and T. Mukaiyama, *Measurement of universal thermodynamic functions for a unitary Fermi gas*, Science **327**, 442 (2010).

[Hu04] H. Hu, A. Minguzzi, X.-J. Liu, and M. P. Tosi, *Collective Modes and Ballistic Expansion of a Fermi Gas in the BCS-BEC Crossover*, Phys. Rev. Lett. **93**, 190403 (2004).

[Hu10] H. Hu, E. Taylor, X.-J. Liu, S. Stringari, and A. Griffin, *Second sound and the density response function in uniform superfluid atomic gases*, New J. Phys. **12**, 043040 (2010).

[Hua87] K. Huang, *Statistical Mechanics*, John Wiley & Sons, New York, 1987.

[Hub63] J. Hubbard, *Electron Correlations in Narrow Energy Bands*, Proc. R. Soc. Lond. A **276**, 238 (1963).

[Huc09] J. H. Huckans, J. R. Williams, E. L. Hazlett, R. W. Stites, and K. M. O'Hara, *Three-body recombination in a three-state Fermi gas with widely tunable interactions*, Phys. Rev. Lett. **102**, 165302 (2009).

[Ian06] M. Iannuzzi, A. Orecchini, F. Sacchetti, P. Facchi, and S. Pascazio, *Direct Experimental Evidence of Free-Fermion Antibunching*, Phys. Rev. Lett. **96**, 080402 (2006).

[Ina08a] Y. Inada, M. Horikoshi, S. Nakajima, M. Kuwata-Gonokami, M. Ueda, and T. Mukaiyama, *Collisional properties of p-wave Feshbach molecules*, Phys. Rev. Lett. **101**, 100401 (2008).

[Ina08b] Y. Inada, M. Horikoshi, S. Nakajima, M. Kuwata-Gonokami, M. Ueda, and T. Mukaiyama, *Critical Temperature and Condensate Fraction of a Fermion Pair Condensate*, Phys. Rev. Lett. **101**, 180406 (2008).

[Ing08] M. Inguscio, W. Ketterle, and C. Salomon (Eds.), *Ultra-cold Fermi Gases*, IOS Press, Amsterdam, 2008, Proceedings of the International School of Physics "Enrico Fermi", Course CLXIV, Varenna, 20-30 June 2006.

[Ino98] S. Inouye, M. R. Andrews, J. Stenger, H.-J. Miesner, D. M. Stamper-Kurn, and W. Ketterle, *Observation of Feshbach resonances in a Bose-Einstein condensate*, Nature **392**, 151 (1998).

[Ino01] S. Inouye, S. Gupta, T. Rosenband, A. P. Chikkatur, A. Görlitz, T. L. Gustavson, A. E. Leanhardt, D. E. Pritchard, and W. Ketterle, *Observation of Vortex Phase Singularities in Bose-Einstein Condensates*, Phys. Rev. Lett. **87**, 080402 (2001).

[Jak98] D. Jaksch, C. Bruder, J. I. Cirac, C. W. Gardiner, and P. Zoller, *Cold bosonic atoms in optical lattices*, Phys. Rev. Lett. **81**, 3108 (1998).

[Joc02] S. Jochim, M. Bartenstein, G. Hendl, J. Hecker Denschlag, R. Grimm, A. Mosk, and W. Weidemüller, *Magnetic Field Control of Elastic Scattering in a Cold Gas of Fermionic Lithium Atoms*, Phys. Rev. Lett **89**, 273202 (2002).

[Joc03a] S. Jochim, M. Bartenstein, A. Altmeyer, G. Hendl, S. Riedl, C. Chin, J. Hecker Denschlag, and R. Grimm, *Bose-Einstein Condensation of Molecules*, Science **302**, 2101 (2003).

[Joc03b] S. Jochim, M. Bartenstein, A. Altmeyer, G. Hendl, C. Chin, J. Hecker Denschlag, and R. Grimm, *Pure Gas of Optically Trapped Molecules Created from Fermionic Atoms*, Phys. Rev. Lett **91**, 240402 (2003).

[Jos04] J. A. Joseph, J. E. Thomas, M. Kulkarni, and A. G. Abanov, *Observation of Shock Waves in a Strongly Interacting Fermi Gas*, Phys. Rev. Lett. **106**, 150401 (2004).

[Jos07] J. Joseph, B. Clancy, L. Luo, J. Kinast, A. Turlapov, and J. E. Thomas, *Measurement of Sound Velocity in a Fermi Gas near a Feshbach Resonance*, Phys. Rev. Lett. **98**, 170401 (2007).

[Kim04a] E. Kim and M. H. W. Chan, *Observation of superflow in solid helium*, Science **305**, 1941 (2004).

[Kim04b] Y. E. Kim and A. L. Zubarev, *Dynamics of strongly interacting Fermi gases of atoms in a harmonic trap*, Phys. Lett. A **327**, 397 (2004).

[Kim04c] Y. E. Kim and A. L. Zubarev, *Time-dependent density-functional theory for trapped strongly interacting fermionic atoms*, Phys. Rev. A **70**, 033612 (2004).

[Kin04a] J. Kinast, S. L. Hemmer, M. E. Gehm, A. Turlapov, and J. E. Thomas, *Evidence for Superfluidity in a Resonantly Interacting Fermi Gas*, Phys. Rev. Lett. **92**, 150402 (2004).

[Kin04b] J. Kinast, A. Turlapov, and J. E. Thomas, *Breakdown of Hydrodynamics in the Radial Breathing Mode of a Strongly Interacting Fermi Gas*, Phys. Rev. A **70**, 051401(R) (2004).

[Kin05a] J. Kinast, A. Turlapov, and J. E. Thomas, *Damping of a Unitary Fermi Gas*, Phys. Rev. Lett. **94**, 170404 (2005).

[Kin05b] J. Kinast, A. Turlapov, J. E. Thomas, Q. Chen, J. Stajic, and K. Levin, *Heat Capacity of a Strongly Interacting Fermi Gas*, Science **307**, 1296 (2005).

[Kin06] J. Kinast, *Thermodynamics and Superfluidity of a Strongly Interacting Fermi Gas*, Ph.D. thesis, Duke University (2006).

[Köh05] M. Köhl, H. Moritz, T. Stöferle, K. Günter, and T. Esslinger, *Fermionic Atoms in a Three Dimensional Optical Lattice: Observing Fermi Surfaces, Dynamics, and Interactions*, Phys. Rev. Lett. **94**, 080403 (2005).

[Kov05] P. K. Kovtun, D. T. Son, , and A. O. Starinets, *Viscosity in Strongly Interacting Quantum Field Theories from Black Hole Physics*, Phys. Rev. Lett. **94**, 111601 (2005).

[Kuh10] E. D. Kuhnle, H. Hu, X.-J. Liu, P. Dyke, M. Mark, P. D. Drummond, P. Hannaford, and C. J. Vale, *Universal Behavior of Pair Correlations in a Strongly Interacting Fermi Gas*, Phys. Rev. Lett. **105**, 070402 (2010).

[Kuh11a] E. D. Kuhnle, S. Hoinka, P. Dyke, H. Hu, P. Hannaford, and C. J. Vale, *Temperature Dependence of the Universal Contact Parameter in a Unitary Fermi Gas*, Phys. Rev. Lett. **106**, 170402 (2011).

[Kuh11b] E. D. Kuhnle, S. Hoinka, H. Hu, P. Dyke, P. Hannaford, and C. J. Vale, *Studies of the universal contact in a strongly interacting Fermi gas using Bragg spectroscopy*, New J. Phys. **13**, 055010 (2011).

[Lan41] L. D. Landau, *The theory of superfluidity of helium II*, J. Phys. (USSR) **5**, 71 (1941).

[Lan47] C. T. Lane, H. A. Fairbank, and W. M. Fairbank, *Second Sound in Liquid Helium II*, Phys. Rev. **71**, 600 (1947).

[Lar65] A. I. Larkin and Y. N. Ovchinnikov, *Inhomogeneous state of superconductors*, Sov. Phys. JETP **20**, 762 (1965).

[Lea02] A. E. Leanhardt, A. Görlitz, A. P. Chikkatur, D. Kielpinski, Y. Shin, D. E. Pritchard, and W. Ketterle, *Imprinting Vortices in a Bose-Einstein Condensate using Topological Phases*, Phys. Rev. Lett. **89**, 190403 (2002).

[Leg80] A. J. Leggett, in: A. Pekalski and R. Przystawa (Eds.), *Modern Trends in the Theory of Condensed Matter*, vol. 115 of *Lecture Notes in Physics*, 13, Springer Verlag, Berlin, 1980.

[Li07] W. Li, G. Partridge, Y. Liao, and R. Hulet, *Pairing of a trapped Fermi gas with unequal spin populations*, Nucl. Phys. A **790**, 88c (2007).

[Lia10] A. S. C. Liao, Yean-an andRittner, T. Paprotta, W. Li, G. B. Partridge, R. G. Hulet, S. K. Baur, and E. J. Mueller, *Spin-imbalance in a one-dimensional Fermi gas*, Nature **467**, 567 (2010).

[Lof02] T. Loftus, C. A. Regal, C. Ticknor, J. L. Bohn, and D. S. Jin, *Resonant Control of Elastic Collisions in an Optically Trapped Fermi Gas of Atoms*, Phys. Rev. Lett. **88**, 173201 (2002).

[Lom10a] T. Lompe, T. B. Ottenstein, F. Serwane, G. Wenz, Andre N.and Zrn, and S. Jochim, *Radio-Frequency Association of Efimov Trimers*, Science **330**, 940 (2010).

[Lom10b] T. Lompe, T. B. Ottenstein, F. Serwane, K. Viering, A. N. Wenz, and S. Zürn, G. and. Jochim, *Atom-Dimer Scattering in a Three-Component Fermi Gas*, Phys. Rev. Lett. **105**, 103201 (2010).

[Luo07] L. Luo, B. Clancy, J. Joseph, J. Kinast, and J. E. Thomas, *Measurement of the Entropy and Critical Temperature of a Strongly Interacting Fermi Gas*, Phys. Rev. Lett. **98**, 080402 (2007).

[Luo09] L. Luo and J. E. Thomas, *Thermodynamic Measurements in a Strongly Interacting Fermi Gas*, J. Low Temp. Phys. **154**, 1 (2009).

[Mad27] E. Madelung, *Quantentheorie in hydrodynamischer Form*, Z. Phys. **40**, 322 (1927).

[Mad00] K. W. Madison, F. Chevy, W. Wohlleben, and J. Dalibard, *Vortex Formation in a Stirred Bose-Einstein Condensate*, Phys. Rev. Lett. **84**, 806 (2000).

[Mad01] K. W. Madison, F. Chevy, V. Bretin, and J. Dalibard, *Stationary States of a Rotating Bose-Einstein Condensate: Routes to Vortex Nucleation*, Phys. Rev. Lett. **86**, 4443 (2001).

[Man05] N. Manini and L. Salasnich, *Bulk and Collective Properties of a Dilute Fermi Gas in the BCS-BEC crossover*, Phys. Rev. A **71**, 033625 (2005).

[Mar00] O. M. Maragò, S. A. Hopkins, J. Arlt, E. Hodby, G. Hechenblaikner, and C. J. Foot, *Observation of the Scissors Mode and Evidence for Superfluidity of a Trapped Bose-Einstein Condensed Gas*, Phys. Rev. Lett. **84**, 2056 (2000).

[Mar01] O. Maragò, G. Hechenblaikner, E. Hodby, and C. Foot, *Temperature Dependence of Damping and Frequency Shifts of the Scissors Mode of a Trapped Bose-Einstein Condensate*, Phys. Rev. Lett. **86**, 3938 (2001).

[Mas05] P. Massignan, G. M. Bruun, and H. Smith, *Viscous relaxation and collective oscillations in a trapped Fermi gas near the unitarity limit*, Phys. Rev. A **71**, 033607 (2005).

[Men02] C. Menotti, P. Pedri, and S. Stringari, *Expansion of an Interacting Fermi Gas*, Phys. Rev. Lett. **89**, 250402 (2002).

[Mep09a] R. Meppelink, S. B. Koller, and P. van der Straten, *Sound propagation in a Bose-Einstein condensate at finite temperatures*, Phys. Rev. A **80**, 043605 (2009).

[Mep09b] R. Meppelink, S. B. Koller, J. M. Vogels, H. T. C. Stoof, and P. van der Straten, *Damping of Superfluid Flow by a Thermal Cloud*, Phys. Rev. Lett. **103**, 265301 (2009).

[Mil05] D. E. Miller, J. R. Anglin, J. R. Abo-Shaeer, K. Xu, J. K. Chin, and W. Ketterle, *Laser-noise-induced heating in far-off resonance optical traps*, Phys. Rev. A **71**, 043615 (2005).

[Mil07] D. E. Miller, J. Chin, C. A. Stan, Y. Liu, W. Setiawan, C. Sanner, and W. Ketterle, *Critical Velocity for Superfluid Flow across the BEC-BCS Crossover*, Phys. Rev. Lett. **99**, 070402 (2007).

[Min01] A. Minguzzi and M. P. Tosi, *Scissors mode in a superfluid Fermi gas*, Phys. Rev. A **63**, 023609 (2001).

[Mod03a] G. Modugno, F. Ferlaino, R. Heidemann, G. Roati, and M. Inguscio, *Production of a Fermi gas of atoms in an optical lattice*, Phys. Rev. A **68** (2003).

[Mod03b] M. Modugno, G. Modugno, G. Roati, C. Fort, and M. Inguscio, *Scissors mode of an expanding Bose-Einstein condensate*, Phys. Rev. A **67** (2003).

[Moe95] A. J. Moerdijk, B. J. Verhaar, and A. Axelsson, *Resonances in ultracold collisions of* ^{6}*Li,* ^{7}*Li, and* ^{2}*3Na*, Phys. Rev. A **51**, 4852 (1995).

[Mül10] T. Müller, B. Zimmermann, J. Meineke, J.-P. Brantut, T. Esslinger, and H. Moritz, *Local Observation of Antibunching in a Trapped Fermi Gas*, Phys. Rev. Lett. **105**, 040401 (2010).

[Nai09] P. Naidon and M. Ueda, *Possible Efimov Trimer State in a Three-Hyperfine-Component Lithium-6 Mixture*, Phys. Rev. Lett. **103**, 073203 (2009).

[Nai11] D. Naik, A. Trenkwalder, C. Kohstall, F. M. Spiegelhalder, M. Zaccanti, G. Hendl, F. Schreck, R. Grimm, T. M. Hanna, and P. S. Julienne, *Feshbach resonances in the* ^{6}*Li-*^{40}*K Fermi-Fermi mixture: elastic versus inelastic interactions*, Eur. Phys. J. D (2011), published online, doi:10.1140/epjd/e2010-10591-2.

[Nak10] S. Nakajima, M. Horikoshi, T. Mukaiyama, P. Naidon, and M. Ueda, *Nonuniversal Emov Atom-Dimer Resonances in a Three-Component Mixture of* ^{6}*Li*, Phys. Rev. Lett. **105**, 023201 (2010).

[Nak11] S. Nakajima, M. Horikoshi, T. Mukaiyama, P. Naidon, and M. Ueda, *Measurement of an Emov Trimer Binding Energy in a Three-Component Mixture of* ^{6}*Li*, Phys. Rev. Lett. **106**, 143201 (2011).

[Nas09] S. Nascimbène, N. Navon, K. J. Jiang, L. Tarruell, M. Teichmann, J. McKeever, F. Chevy, and C. Salomon, *Collective Oscillations of an Imbalanced Fermi Gas: Axial Compression Modes and Polaron Effective Mass*, Phys. Rev. Lett. **103**, 170402 (2009).

[Nas10a] S. Nascimbène, N. Navon, F. Chevy, and C. Salomon, *The equation of state of ultracold Bose and Fermi gases: a few examples*, New J. of Phys. **12**, 103026 (2010).

[Nas10b] S. Nascimbène, N. Navon, K. J. Jiang, F. Chevy, and C. Salomon, *Exploring the thermodynamics of a universal Fermi gas*, Nature **463**, 1057 (2010).

[Nav10] N. Navon, S. Nascimbène, F. Chevy, and C. Salomon, *The Equation of State of a Low-Temperature Fermi Gas with Tunable Interactions*, Science **328**, 729 (2010).

[Nik01] T. Nikuni and A. Griffin, *Temperature-dependent relaxation times in a trapped Bose-condensed gas*, Phys. Rev. A **65**, 011601(R) (2001).

[Noz85] P. Nozières and S. Schmitt-Rink, J. Low Temp. Phys. **59**, 195 (1985).

[O'H02a] K. M. O'Hara, S. L. Hemmer, M. E. Gehm, S. R. Granade, and J. E. Thomas, *Observation of a Strongly Interacting Degenerate Fermi Gas*, Science **298**, 2179 (2002).

[OH02b] K. M. OHara, S. L. Hemmer, S. R. Granade, M. E. Gehm, J. E. Thomas, V. Venturi, E. Tiesinga, and C. J. Williams, *Measurement of the zero crossing in a Feshbach resonance of fermionic 6Li*, Phys. Rev. A **66**, 041401 (2002).

[Ott08] T. B. Ottenstein, T. Lompe, M. Kohnen, A. N. Wenz, and S. Jochim, *Collisional stability of a three-component degenerate Fermi gas*, Phys. Rev. Lett. **101**, 203202 (2008).

[Par05] G. B. Partridge, K. E. Strecker, R. I. Kamar, M. W. Jack, and R. G. Hulet, *Molecular Probe of Pairing in the BEC-BCS Crossover*, Phys. Rev. Lett. **95**, 020404 (2005).

[Par06a] G. B. Partridge, W. Li, R. I. Kamar, Y. Liao, and R. G. Hulet, *Pairing and Phase Separation in a Polarized Fermi Gas*, Science **311**, 503 (2006).

[Par06b] G. B. Partridge, W. Li, R. G. Liao, Y. A. and. Hulet, and H. T. C. Haque, M. and. Stoof, *Deformation of a Trapped Fermi Gas with Unequal Spin Populations*, Phys. Rev. Lett. **97**, 190407 (2006).

[Par07] G. Partridge, W. Li, Y. Liao, and R. Hulet, *Pairing, Phase Separation, and Deformation in the BEC-BCS Crossover*, J. Low Temp. Phys. **148**, 323 (2007).

[Ped03] P. Pedri, D. Guéry-Odelin, and S. Stringari, *Dynamics of a classical gas including dissipative and mean-field effects*, Phys. Rev. A **68**, 043608 (2003).

[Per04] A. Perali, P. Pieri, L. Pisani, and G. C. Strinati, *BCS-BEC Crossover at Finite Temperature for Superfluid Trapped Fermi Atoms*, Phys. Rev. Lett. **92** (2004).

[Per11] A. Perali, F. Palestini, P. Pieri, G. C. Strinati, J. T. Stewart, J. P. Gaebler, T. E. Drake, and D. S. Jin, *Evolution of the Normal State of a Strongly Interacting Fermi Gas from a Pseudogap Phase to a Molecular Bose Gas*, Phys. Rev. Lett. **106**, 060402 (2011).

[Pes44] V. Peshkov, *"Second sound" in helium II*, J. Phys. (USSR) **8**, 381 (1944).

[Pet05a] D. S. Petrov, C. Salomon, and G. V. Shlyapnikov, *Diatomic molecules in ultracold Fermi gases – novel composite bosons*, J. Phys. B: At. Mol. Opt. Phys. **38**, S645 (2005).

[Pet05b] D. S. Petrov, C. Salomon, and G. V. Shlyapnikov, *Scattering properties of weakly bound dimers of fermionic atoms*, Phys. Rev. A **71** (2005).

[Pie09] P. Pieri, A. Perali, and G. C. Strinati, *Enhanced paraconductivity-like fluctuations in the radiofrequency spectra of ultracold Fermi atoms*, Nature Phys. **5**, 736 (2009).

[Pie11] P. Pieri, A. Perali, G. C. Strinati, S. Riedl, M. J. Wright, A. Altmeyer, C. Kohstall, J. Sánchez Guajardo, E. R.and Hecker Denschlag, and R. Grimm, *Pairing-gap, pseudo-gap, and no-gap phases in rf spectra of a trapped unitary 6Li gas*, Phys. Rev. A **84**, 011608(R) (2011).

[Pit98] L. Pitaevskii and S. Stringari, *Elementary Excitations in Trapped Bose-Einstein Condensed Gases Beyond the Mean-Field Approximation*, Phys. Rev. Lett. **81**, 4541 (1998).

[Reg03] C. A. Regal, C. Ticknor, J. L. Bohn, and D. S. Jin, *Creation of Ultracold Molecules from a Fermi Gas of Atoms*, Nature **424**, 47 (2003).

[Reg04a] C. A. Regal, M. Greiner, and D. S. Jin, *Lifetime of Molecule-Atom Mixtures near a Feshbach Resonance in K*, Phys. Rev. Lett. **92**, 083201 (2004).

[Reg04b] C. A. Regal, M. Greiner, and D. S. Jin, *Observation of Resonance Condensation of Fermionic Atom Pairs*, Phys. Rev. Lett. **92**, 040403 (2004).

[Rie08] S. Riedl, E. R. Sánchez Guajardo, C. Kohstall, A. Altmeyer, M. J. Wright, J. Hecker Denschlag, R. Grimm, G. M. Bruun, and H. Smith, *Collective oscillations of a Fermi gas in the unitarity limit: Temperature effects and the role of pair correlations*, Phys. Rev. A **78**, 053609 (2008).

[Rie09] S. Riedl, E. R. Sánchez Guajardo, C. Kohstall, J. Hecker Denschlag, and R. Grimm, *Lifetime of angular momentum in a rotating strongly interacting Fermi gas*, Phys. Rev. A **79**, 053628 (2009).

[Rie11] S. Riedl, E. R. Sánchez Guajardo, C. Kohstall, J. Hecker Denschlag, and R. Grimm, *Superfluid quenching of the moment of inertia in a strongly interacting Fermi gas*, New J. of Phys. **13**, 035003 (2011).

[Rin80] P. Ring and P. Schuck, *The Nuclear Many Body Problem*, Springer, Berlin, 1980.

[Roa02] G. Roati, F. Riboli, G. Modugno, and M. Inguscio, *Fermi-Bose Quantum Degenerate K-Rb Mixture with Attractive Interaction*, Phys. Rev. Lett. **89**, 150403 (2002).

[Rob00] J. L. Roberts, N. R. Claussen, S. L. Cornish, and C. E. Wieman, *Magnetic Field Dependence of Ultracold Inelastic Collisions near a Feshbach Resonance*, Phys. Rev. Lett. **85**, 728 (2000).

[Rom06] T. Rom, T. Best, D. van Oosten, U. Schneider, S. Fölling, B. Paredes, and I. Bloch, *Free fermion antibunching in a degenerate atomic Fermi gas released from an optical lattice*, Nature **444**, 733 (2006).

[Sav97] T. A. Savard, K. M. O'Hara, and J. E. Thomas, *Laser-noise-induced heating in far-off resonance optical traps*, Phys. Rev. A **56**, R1095 (1997).

[Sch94] W. Schöllkopf and J. P. Toennies, *Nondestructive Mass Selection of Small van der Waals Clusters*, Science **266**, 1345 (1994).

[Sch01] F. Schreck, L. Khaykovich, K. L. Corwin, G. Ferrari, T. Bourdel, J. Cubizolles, and C. Salomon, *Quasipure Bose-Einstein Condensate Immersed in a Fermi Sea*, Phys. Rev. Lett. **87**, 080403 (2001).

[Sch07a] T. Schäfer, *Ratio of shear viscosity to entropy density for trapped fermions in the unitarity limit*, Phys. Rev. A **76**, 063618 (2007).

[Sch07b] C. H. Schunck, M. W. Zwierlein, A. Schirotzek, and W. Ketterle, *Superfluid Expansion of a Rotating Fermi Gas*, Phys. Rev. Lett. **98**, 050404 (2007).

[Sch08a] A. Schirotzek, Y.-i. Shin, C. H. Schunck, and W. Ketterle, *Determination of the Superfluid Gap in Atomic Fermi Gases by Quasiparticle Spectroscopy*, Phys. Rev. Lett. **101**, 140403 (2008).

[Sch08b] U. Schneider, L. Hackermller, S. Will, T. Best, I. Bloch, T. A. Costi, R. W. Helmes, D. Rasch, and A. Rosch, *Metallic and Insulating Phases of Repulsively Interacting Fermions in a 3D Optical Lattice*, Science **322**, 204 (2008).

[Sch08c] C. H. Schunck, Y.-i. Shin, A. Schirotzek, and W. Ketterle, *Determination of the fermion pair size in a resonantly interacting superfluid*, Nature **454**, 739 (2008).

[Sen10] R. Sensarma, D. Pekker, E. Altman, E. Demler, N. Strohmaier, D. Greif, R. Jördens, L. Tarruell, H. Moritz, and T. Esslinger, *Lifetime of double occupancies in the Fermi-Hubbard model*, Phys. Rev. B **82**, 224302 (2010).

[Ser11] F. Serwane, G. Zürn, T. Lompe, T. B. Ottenstein, A. N. Wenz, and S. Jochim, *Deterministic Preparation of a Tunable Few-Fermion System*, Science **332**, 336 (2011).

[She98] V. B. Shenoy and T.-L. Ho, *First and Second Sound Modes of a Bose-Einstein Condensate in a Harmonic Trap*, Phys. Rev. Lett. **80**, 3895 (1998).

[Shi04] Y. Shin, M. Saba, T. A. Pasquini, W. Ketterle, D. E. Pritchard, and A. E. Leanhardt, *Atom Interferometry with Bose-Einstein Condensates in a Double-Well Potential*, Phys. Rev. Lett. **92**, 050405 (2004).

[Shi06] Y. Shin, M. Zwierlein, C. H. Schunck, A. Schirotzek, and W. Ketterle, *Observation of Phase Separation in a Strongly Interacting Imbalanced Fermi Gas*, Phys. Rev. Lett. **97**, 030401 (2006).

[Shi07] Y. Shin, C. H. Schunck, and W. Schirotzek, A. and. Ketterle, *Tomographic rf Spectroscopy of a Trapped Fermi Gas at Unitarity*, Phys. Rev. Lett. **99**, 090403 (2007).

[Shi08] Y.-i. Shin, C. H. Schunck, and W. Schirotzek, Andreand Ketterle, *Phase diagram of a two-component Fermi gas with resonant interactions*, Nature **451**, 689 (2008).

[Sim00] J. E. Simsarian, J. Denschlag, M. Edwards, C. W. Clark, L. Deng, E. W. Hagley, K. Helmerson, S. L. Rolston, and W. D. Phillips, *Imaging the Phase of an Evolving Bose-Einstein Condensate Wave Function*, Phys. Rev. Lett. **85**, 2040 (2000).

[Sin97] S. Sinha, *Semiclassical analysis of collective excitations in Bose-Einstein condensate*, Phys. Rev. A **55**, 4325 (1997).

[Spi09] F. M. Spiegelhalder, A. Trenkwalder, D. Naik, G. Hendl, F. Schreck, and R. Grimm, *Collisional stability of* ^{40}K *immersed in a strongly interacting Fermi Gas of* ^{6}Li, Phys. Rev. Lett. **103**, 223203 (2009).

[Spi10] F. M. Spiegelhalder, A. Trenkwalder, D. Naik, G. Kerner, E. Wille, G. Hendl, F. Schreck, and R. Grimm, *All-optical production of a degenerate mixture of 6Li and 40K and creation of heteronuclear molecules*, Phys. Rev. A **81**, 043637 (2010).

[Sta98] D. M. Stamper-Kurn, H.-J. Miesner, S. Inouye, M. R. Andrews, and W. Ketterle, *Collisionless and Hydrodynamic Excitations of a Bose-Einstein Condensate*, Phys. Rev. Lett. **81**, 500 (1998).

[Sta05] J. Stajic, Q. Chen, and K. Levin, *Density Profiles of Strongly Interacting Trapped Fermi Gases*, Phys. Rev. Lett. **94** (2005).

[Ste06] J. T. Stewart, J. P. Gaebler, C. A. Regal, and D. S. Jin, *Potential Energy of a [sup 40]K Fermi Gas in the BCS-BEC Crossover*, Phys. Rev. Lett. **97** (2006).

[Ste08] J. T. Stewart, J. P. Gaebler, and D. S. Jin, *Using photoemission spectroscopy to probe a strongly interacting Fermi gas*, Nature **454**, 744 (2008).

[Ste10] J. T. Stewart, J. P. Gaebler, T. E. Drake, and D. S. Jin, *Verication of Universal Relations in a Strongly Interacting Fermi Gas*, Phys. Rev. Lett. **104**, 235301 (2010).

[Stö06] T. Stöferle, H. Moritz, K. Günter, M. Köhl, and T. Esslinger, *Molecules of Fermionic Atoms in an Optical Lattice*, Phys. Rev. Lett. **96**, 030401 (2006).

[Str] S. Stringari, *Private communication.*

[Str96] S. Stringari, *Moment of Inertia and Superfluidity of a Trapped Bose Gas*, Phys. Rev. Lett. **76**, 1405 (1996).

[Str03] K. E. Strecker, G. B. Partridge, and R. G. Hulet, *Conversion of an Atomic Fermi Gas to a Long-Lived Molecular Bose Gas*, Phys. Rev. Lett. **91**, 080406 (2003).

[Str04] S. Stringari, *Collective Oscillations of a Trapped Superfluid Fermi Gas near a Feshbach Resonance*, Europhys. Lett. **65**, 749 (2004).

[Str11] S. Stringari, *Private communication* (2011).

[Svi98] A. A. Svidzinsky and A. L. Fetter, *Normal modes of a vortex in a trapped Bose-Einstein condensate*, Phys. Rev. A **58**, 3168 (1998).

[Tag08] M. Taglieber, A.-C. Voigt, T. Aoki, T. W. Hänsch, and K. Dieckmann, *Quantum Degenerate Two-Species Fermi-Fermi Mixture Coexisting with a Bose-Einstein Condensate*, Phys. Rev. Lett. **100**, 010401 (2008).

[Tan08a] S. Tan, *Energetics of a strongly correlated Fermi gas*, Ann. Phys. **323**, 2952 (2008).

[Tan08b] S. Tan, *Generalized virial theorem and pressure relation for a strongly correlated Fermi gas*, Ann. Phys. **323**, 2987 (2008).

[Tan08c] S. Tan, *Large momentum part of a strongly correlated Fermi gas*, Ann. Phys. **323**, 2971 (2008).

[Tay05] E. Taylor and A. Griffin, *Two-fluid hydrodynamic modes in a trapped superfluid gas*, Phys. Rev. A **72**, 053630 (2005).

[Tay08] E. Taylor, X.-J. Hu, H.and Liu, and A. Griffin, *Variational theory of two-fluid hydrodynamic modes at unitarity*, Phys. Rev. A **77**, 033608 (2008).

[Tay09] E. Taylor, X.-J. Hu, H.and Liu, L. P. Pitaevskii, A. Griffin, and S. Stringari, *First and second sound in a strongly interacting Fermi gas*, Phys. Rev. A **80**, 053601 (2009).

[Tho05] J. E. Thomas, J. Kinast, and A. Turlapov, *Virial Theorem and Universality in a Unitary Fermi Gas*, Phys. Rev. Lett. **95** (2005).

[Tie10] T. G. Tiecke, M. R. Goosen, A. Ludewig, S. D. Gensemer, S. Kraft, S. J. J. M. F. Kokkelmans, and J. T. M. Walraven, *Broad Feshbach resonance in the* ^6Li-^{40}K *mixture*, Phys. Rev. Lett. **104**, 053202 (2010).

[Tis38] L. Tisza, *Transport Phenomena in Helium II*, Nature **141**, 913 (1938).

[Tis40a] L. Tisza, *Sur la théorie des liquides quantiques. Application à l'hélium liquide*, J. Phys. Radium **1**, 164 (1940).

[Tis40b] L. Tisza, *Sur la théorie des liquides quantiques. Application à l'hélium liquide. II*, J. Phys. Radium **1**, 350 (1940).

[Tre11] A. Trenkwalder, C. Kohstall, M. Zaccanti, D. Naik, A. I. Sidorov, and R. Schreck, F. and. Grimm, *Hydrodynamic Expansion of a Strongly Interacting Fermi-Fermi Mixture*, Phys. Rev. Lett. **106**, 115304 (2011).

[Tru01] A. G. Truscott, K. E. Strecker, W. I. McAlexander, G. B. Partridge, and R. G. Hulet, *Observation of Fermi Pressure in a Gas of Trapped Atoms*, Science **291**, 2570 (2001).

[Tur08] A. Turlapov, J. Kinast, B. Clancy, L. Luo, J. Joseph, and J. Thomas, *Is a Gas of Strongly Interacting Atomic Fermions a Nearly Perfect Fluid?*, J. Low Temp. Phys. **150**, 567 (2008).

[Urb03] M. Urban and P. Schuck, *Slow rotation of a superfluid trapped Fermi gas*, Phys. Rev. A **67**, 033611 (2003).

[Urb05] M. Urban, *Two-fluid model for a rotating trapped Fermi gas in the BCS phase*, Phys. Rev. A **71**, 033611 (2005).

[Vee08] G. Veeravalli, E. Kuhnle, P. Dyke, and C. J. Vale, *Bragg Spectroscopy of a Strongly Interacting Fermi Gas*, Phys. Rev. Lett. **101**, 250403 (2008).

[Vic00] L. Vichi, *Collisional Damping of the Collective Oscillations of a Trapped Fermi Gas*, J. Low. Temp. Phys. **121**, 177 (2000).

[Voi09] A.-C. Voigt, M. Taglieber, L. Costa, T. Aoki, W. Wieser, T. W. Hänsch, and K. Dieckmann, *Ultracold heteronuclear Fermi-Fermi molecules*, Phys. Rev. Lett. **102**, 020405 (2009), *ibid.* **105**, 269904(E) (2010).

[Voi10] A.-C. Voigt, M. Taglieber, L. Costa, T. Aoki, W. Wieser, T. Hänsch, and K. Dieckmann, *Erratum: Ultracold Heteronuclear Fermi-Fermi Molecules*, Phys. Rev. Lett. **105**, 269904 (2010).

[Wel09] D. M. Weld, P. Medley, H. Miyake, D. Hucul, D. E. Pritchard, and W. Ketterle, *Spin Gradient Thermometry for Ultracold Atoms in Optical Lattices*, Phys. Rev. Lett. **103**, 245301 (2009).

[Wen09] A. N. Wenz, T. Lompe, T. B. Ottenstein, F. Serwane, G. Zürn, and S. Jochim, *Universal trimer in a three-component Fermi gas*, Phys. Rev. A **80**, 040702(R) (2009).

[Wil02] J. E. Williams, E. Zaremba, B. Jackson, T. Nikuni, and A. Griffin, *Dynamical Instability of a Condensate Induced by a Rotating Thermal Gas*, Phys. Rev. Lett. **88**, 070401 (2002).

[Wil08] E. Wille, F. M. Spiegelhalder, G. Kerner, D. Naik, A. Trenkwalder, G. Hendl, F. Schreck, R. Grimm, T. G. Tiecke, J. T. M. Walraven, S. J. J. M. F. Kokkelmans, E. Tiesinga, and P. S. Julienne, *Exploring an ultracold Fermi-Fermi mixture: Interspecies Feshbach resonances and scattering properties of* ^6Li *and* ^{40}K, Phys. Rev. Lett. **100**, 053201 (2008).

[Wil09] J. R. Williams, E. L. Hazlett, J. H. Huckans, R. W. Stites, Y. Zhang, and K. M. O'Hara, *Evidence for an excited-state Efimov trimer in a three-component Fermi gas*, Phys. Rev. Lett. **103**, 130404 (2009).

[Wri07] M. J. Wright, S. Riedl, A. Altmeyer, C. Kohstall, E. R. Sánchez Guajardo, J. Hecker Denschlag, and R. Grimm, *Finite-temperature collective dynamics of a Fermi gas in the BEC-BCS crossover*, Phys. Rev. Lett. **99**, 150403 (2007).

[Xio06] H. Xiong, S. Liu, and M. Zhan, *Interaction-induced interference for two independent BoseEinstein condensates*, New J. Phys. **8**, 245 (2006).

[Xu03] K. Xu, T. Mukaiyama, J. R. Abo-Shaeer, J. K. Chin, D. E. Miller, and W. Ketterle, *Formation of Quantum-Degenerate Sodium Molecules*, Phys. Rev. Lett. **91** (2003).

[Zam98] F. Zambelli and S. Stringari, *Quantized Vortices and Collective Oscillations of a Trapped Bose-Einstein Condensate*, Phys. Rev. Lett. **81**, 1754 (1998).

[Zar98] E. Zaremba, A. Griffin, and T. Nikuni, *Two-fluid hydrodynamics for a trapped weakly interacting Bose gas*, Phys. Rev. A **57**, 4695 (1998).

[Zaw10] M. E. Zawadzki, P. F. Griffin, E. Riis, and A. S. Arnold, *Spatial interference from well-separated split condensates*, Phys. Rev. A **81**, 043608 (2010).

[Zha07] W. Zhang and C. A. R. Sá de Melo, *Matter-wave interference in s-wave and p-wave Fermi condensates*, Phys. Rev. A **76**, 013627 (2007).

[Zhu01] O. N. Zhuravlev, A. E. Muryshev, and P. O. Fedichev, *Dissipative dynamics of vortex arrays in anisotropic traps*, Phys. Rev. A **64**, 053601 (2001).

[Zil50] P. R. Zilsel, *Liquid Helium II: The Hydrodynamics of the Two-Fluid Model*, Phys. Rev. **79**, 309 (1950).

[Zim11] B. Zimmermann, T. Müller, J. Meineke, T. Esslinger, and H. Moritz, *High-resolution imaging of ultracold fermions in microscopically tailored optical potentials*, New J. of Phys. **13**, 043007 (2011).

[Zou10] P. Zou, E. D. Kuhnle, C. J. Vale, and H. Hu, *Quantitative comparison between theoretical predictions and experimental results for Bragg spectroscopy of a strongly interacting Fermi superuid*, Phys. Rev. A **82**, 061605(R) (2010).

[Zwi03] M. W. Zwierlein, C. A. Stan, C. H. Schunck, S. M. F. Raupach, S. Gupta, Z. Hadzibabic, and W. Ketterle, *Observation of Bose-Einstein Condensation of Molecules*, Phys. Rev. Lett. **91**, 250401 (2003).

[Zwi04] M. W. Zwierlein, C. A. Stan, C. H. Schunck, S. M. F. Raupach, A. J. Kerman, and W. Ketterle, *Condensation of Pairs of Fermionic Atoms near a Feshbach Resonance*, Phys. Rev. Lett. **92**, 120403 (2004).

[Zwi05] M. W. Zwierlein, J. R. Abo-Shaeer, A. Schirotzek, C. H. Schunck, and W. Ketterle, *Vortices and Superfluidity in a Strongly Interacting Fermi Gas*, Nature **435**, 1047 (2005).

[Zwi06] M. W. Zwierlein, A. Schirotzek, C. H. Schunck, and W. Ketterle, *Fermionic Superfluidity with Imbalanced Spin Populations*, Science **311**, 492 (2006).